Phenoxazinone synthase (PHS) Activity of Azurin Variants

A THESIS
SUBMITTED TO THE FACULTY OF THE GRADUATE SCHOOL
OF THE UNIVERSITY OF MINNESOTA
BY

Garrett Joseph Stoddard

IN PARTIAL FULFILLMENT OF THE REQUIREMENTS
FOR THE DEGREE OF
MASTER OF SCIENCE

Steven M. Berry

August 2014

Acknowledgements

I would like to thank all my family and friends who have supported me throughout my entire education. In addition, I would like to thank Dr. Steven Berry for his guidance and mentorship throughout my entire experience at UMD. I would also like to thank my fellow graduate students in lab, specifically: Jacob Strange, Balabhadra Khatiwada, and Alexandra Sauer. I am also very grateful to some great undergraduate students in our lab: Emmalee Toldo, Christine Hedstrom, and Tracy Roach. I would like to acknowledge the University of Minnesota Duluth, for providing me with the funding and facilities to complete this work by supporting me with many graduate teaching assistantships, and acknowledge the NIH for funding.

I would like to dedicate this work to my grandfather Clarence Norman Jensen for giving me the opportunity to follow my path in life. You will be forever loved and missed.

Abstract

Phenoxazinone synthase (PHS) is a multicopper oxidase that catalyzes the oxidation of ortho-aminophenol to aminophenoxazinone, by coupling the 6 e^- oxidation with the reduction of O_2. To study this reaction, an azurin protein scaffold model was used. Our models contain the naturally occurring T1 copper center and an additional designed surface T2 copper center. The T2 copper centers in these variants were modeled after 2 other naturally occurring copper oxidoreductases, nitrite reductase (NiR) and peptidylglycine α-hydroxylating monooxygenase (PHM). A PHS activity assay was adapted to investigate the activities of PHM-Azurin and NiR-Azurin using an already 2 e^- reduced peroxide shunt pathway as well as the native O_2 as oxidants. The assay was optimized with a 20 mM potassium phosphate buffer at pH 7.5 and a 10 mM tert-butylhydroperoxide shunt at a final enzyme concentration of 1 μM. Second generation variants in which the T1 copper center's reduction potential was decreased and an electron transfer tryptophan mutation was incorporated were assayed and found to increase turnover number for almost all surface T2 copper variants.

Table of Contents

List of Tables

List of Figures

Chapter 1: Introduction

1.1 Phenoxazinone Synthase and its Role as a Multicopper Oxidase

Phenoxazinone Synthase (PHS) is a multicopper oxidase that catalyzes the oxidation of 3-hydroxyanthranilic acid to actinomycin D[1] (Figure 1), the final step in the production of actinomycin D in *Streptomyces* antibioticus. PHS is only found in *Streptomyces* antibioticus. Actinomycin D has been shown to be effective as an anti-cancer drug[2], due to its ability to intercalate nucleic acids in DNA. Actinomycin D is a common treatment for a wide range of cancers.[3] When used in combination with surgery, it has been shown to increase the cure rate of patients with Wilms' tumor from 40% to 80%.[4]

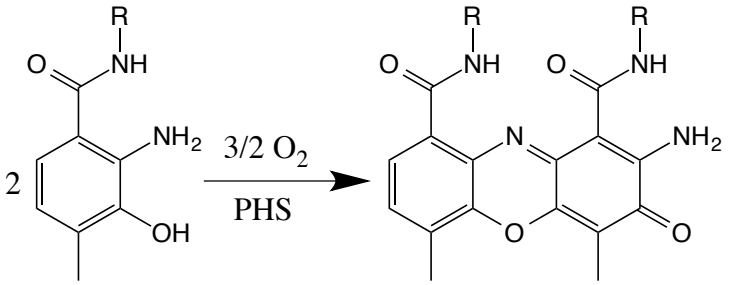

3-Hydroxyanthranilic Acid Actinomycin D

Figure 1. A reaction catalyzed by PHS in which 3-hydroxyanthranilic acid is oxidized to actinomycin D, coupled to the reduction of 3/2 molecules of O_2.

The reaction catalyzed by PHS is the 6 e^- oxidation of *o*-aminophenol (oAP) to aminophenoxazinone (APX), the chromophore of actinomycin D (Figure 2).[5] Aminophenoxazinone has an absorbance at 434 nm with a molar absorptivity of 23,200 $M^{-1}cm^{-1}$.[5] An example absorbance spectrum of APX is shown in Figure 3.

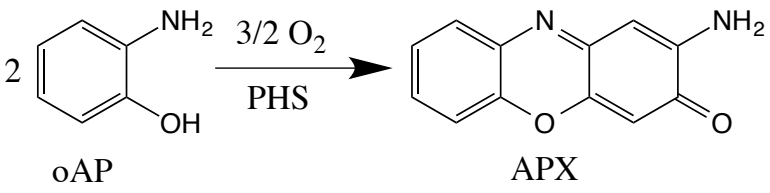

Figure 2. The analogous reaction commonly used as an assay to study PHS. The oxidation of *o*-aminophenol to aminophenoxazinone by PHS and 3/2 molecules O_2.

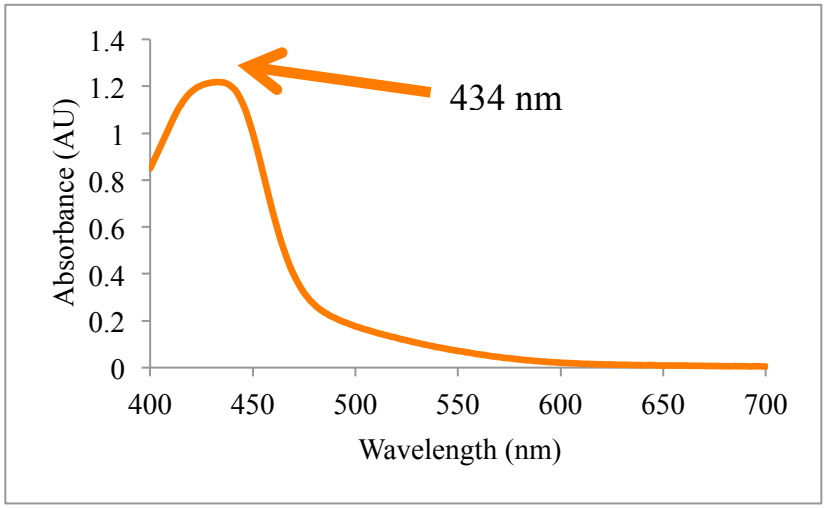

Figure 3. Example spectrum of aminophenoxazinone showing an absorbance at 434 nm. This peak was used to monitor the concentration of product in all experiments with PHS.

The APX core can be found in various natural sources such as insects, fungi, and Australian marsupials.[6] Within these various organisms, it has been shown to function as both a pigment and a as a protectant against oxidative damage.[6] Due to the plethora of applications for the product, the reaction of PHS is of great interest. Native PHS couples the 6 e^- oxidation of oAP to APX with the 4 e^- reduction of 3/2 molecules of O_2.[7] The use of oxygen is a very important phenomenon as it is a naturally available and abundant oxidant. There are a handful of known PHS enzyme family members, which differ in many fundamental ways including; substrate selectivity, cofactor dependence, inhibition profiles, and molecular structure.[3] The most significant difference between PHS family members is that only 2 PHS enzymes are Cu^{2+} and O_2 dependent: phenoxazinone

synthase (PHS)[5] and grixazone F (GriF)[8]. Other PHS like enzymes utilize Mn^{2+} and flavin adenine dinucleotide (FAD)[9].

Other copper proteins are known that are similar to copper PHS in that they use of oxygen as an oxidant. These include enzymes such as peptidylglycine α-hydroxylating monooxygenase (PHM)[10], tryrosinase[11], and Tyramine β-monooxygenase (TβM).[12] The oxidoreductase PHM will be discussed in more detail (Section 1.2) as another copper protein of interest we have investigated. The remainder of this section will focus on PHS as a multicopper oxidase

PHS was first discovered in 1962 when Katz and Weissbach purified it from *Streptomyces antibioticus*.[13] Preliminary investigations incorrectly identified copper as an inhibitory metal, by as much as 100 % inhibition.[13] Originally, Mn^{2+} or Ca^{2+} was believed to be the metal ion needed for activity.[13] It wasn't until 1969, that Cu^{2+} was identified as the active metal for PHS.[14] The Nishimura group was able to inhibit PHS' activity by binding cyanide to the enzyme and showed that only dialysis with a Cu^{2+} solution was able to reverse the inhibition[14], thus identifying PHS as a copper protein. Little was known about PHS until the Barry group undertook an exhaustive mechanistic study in 1989.[5] This study investigated the mechanistic steps involved in the conversion of oAP to APX using PHS and O_2. The mechanism was proposed to be a cascade of three 2 e^- oxidations and two conjugate additions, with the first intermediate being the quinone imine product.[5] An abbreviated form of the mechanism is shown in Figure 4. According to Barry, the first reaction occurs at the active site of PHS when it accepts 2 e^- from oAP and forms the quinone imine intermediate. Then, the quinone imine intermediate undergoes a conjugate addition with another oAP to form a "dimerized"

intermediate. The mechanism for the next two oxidations and conjugate addition are debated and unclear. However, it is hypothesized that four more electrons are lost as two more oxidations and one more conjugate addition in seven steps. It is not clear if the PHS enzyme plays a role in the latter oxidations. In addition, the Barry group identified 3.7 Cu atoms per subunit as being necessary for PHS activity. This would be disputed and then investigated by a later investigation that determined 4-5 Cu atoms per subunit are required for maximum activity.[1]

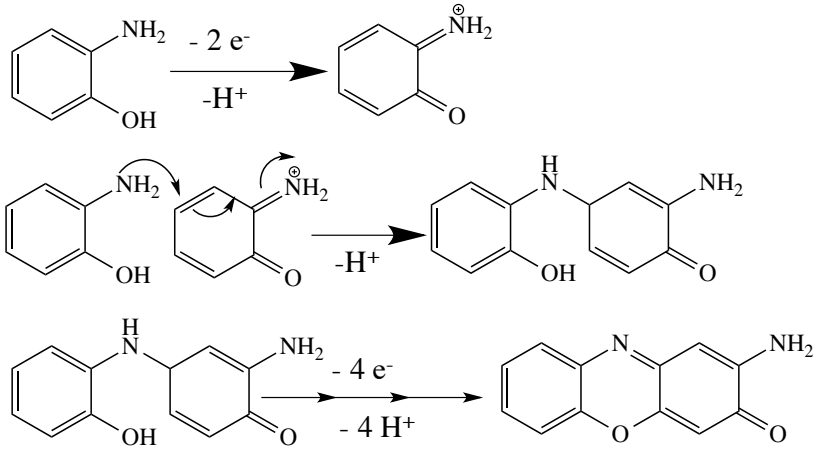

Figure 4. Abbreviated mechanism of the conversion of oAP to APX by PHS. Shown is the first catalytic step involving the 2 e^- transfer to PHS to form the quinone imine intermediate that undergoes a conjugate addition with another oAP to form the "dimerized" intermediate. Adapted from Barry et al (1989).

PHS is known to be active in two forms; dimers of low activity and hexamers of high activity. Later investigations showed the age of the bacteria cell cultures dictates which form will be produced, with the older cultures producing the hexameric form and younger cell producing the dimeric form.[3] The active structure that is most studied is the hexameric form (Figure 5), which was studied by X-ray crystallography. Each subunit weighs 88 kDa and was found to contain five copper(II) ions in the crystal structure. The five coppers were found in one type one (T1), two type 2 (T2), and one type 3 (dinuclear copper center) (T3) copper centers and makes for 30 copper atoms total in the hexamer.

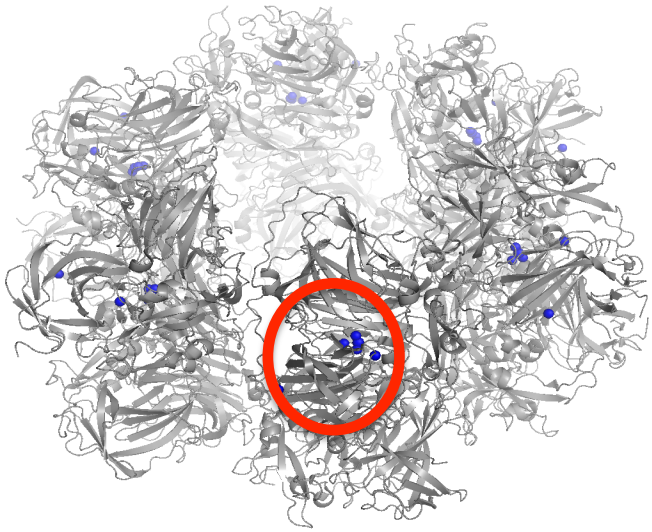

Figure 5. Image of the multicopper oxidase Phenoxazinone synthase (PHS) in its hexameric form. Circled in red is the active site of one PHS subunit containing 1 T1, 1 T2, and 1 T3 copper center. PDB: 3GYR

The T1 site in PHS is that of a typical blue T1 copper center that is coordinated by two histidines, one cysteine, and one methionine,[2] with distorted tetrahedral geometry. Like that of a typical "blue" T1 center, it is believed to function as an electron transfer site in PHS and is the primary electron acceptor from oAP.[7] The T1 center in PHS has a λ_{max} = 598 nm with an absorptivity of 4,000 M^{-1} cm^{-1}.[1,5] The absorbance near 600 nm from all T1 copper centers arises from the S(cys) pπ → Cu $3d_{X^2-Y^2}$ transition.[15,16] One of the two T2 centers in the active site of PHS is coordinated by two histidines and one H_2O, as opposed to a typical "normal" or more common T2 site that is coordinated by three histidines.[7] The second T2 site is coordinated by three histidines, but is not located near the other copper centers. Based on the crystal structure, it is believed to play a structural role to stabilize the hexameric form as the copper binds in a loop near the interface of the subunits. The last two copper ions in PHS are located in a T3 copper center. A T3 copper center is different from the previous two, as it is a dinuclear copper center. It contains two Cu atoms in close proximity (~4.5 Å), each coordinated by three histidines,

and bridged by a hydroxide ligand. Examples of typical copper centers are shown in Figure 6. The active site of PHS, comprised of the T1, one T2, and the T3 copper centers, is a copper ion binding motif that is common in the a larger family of copper binding proteins called the multicopper oxidases.[7] .

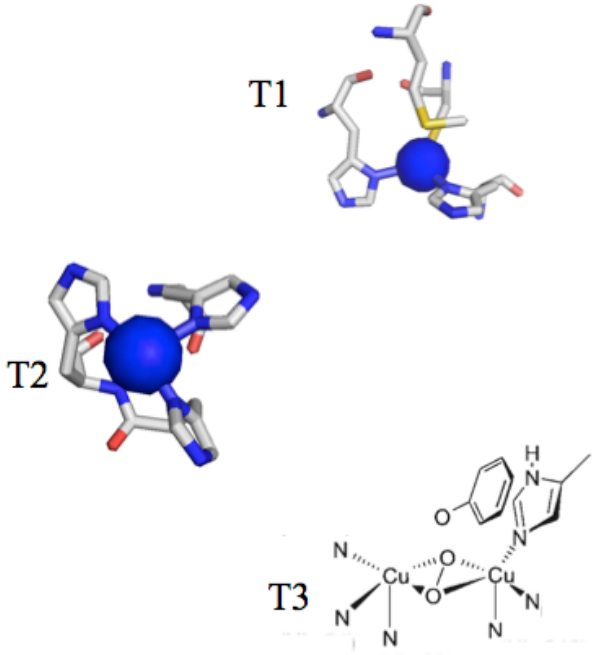

Figure 6. Examples of typical copper centers, including a type 1 (T1), type 2 (T2), and a type 3 (T3). The T3 copper center is shown with nitrogens from the histidines for clarity. PDB: 4AZU, 1PHM, and 1WX2.

The multicopper oxidase (MCO) family of enzymes is a large group of copper proteins that are defined by their sequence homology, spectroscopy, and reactivity. Some examples of multicopper oxidases include laccase, ascorbate oxidase, ceruloplasmin, bilirubin oxidase, and sulochrin oxidase.[3,5,7] The sequences of MCOs have been shown to be alike. When a study compared laccase and PHS it was found that their amino acid sequences were 76% similar.[17] The 3D structure of MCOs typically consists of 3 domains that all have a similar Greek β-barrel structure.[3,18] In addition to the similar 3D structure, MCOs all have a highly conserved active site containing a T1, T2, and a T3

copper center (Figure 7). Another similarity amongst MCOs is that their T1 site provides a blue color from the absorbance at 600 nm in the visible light region.

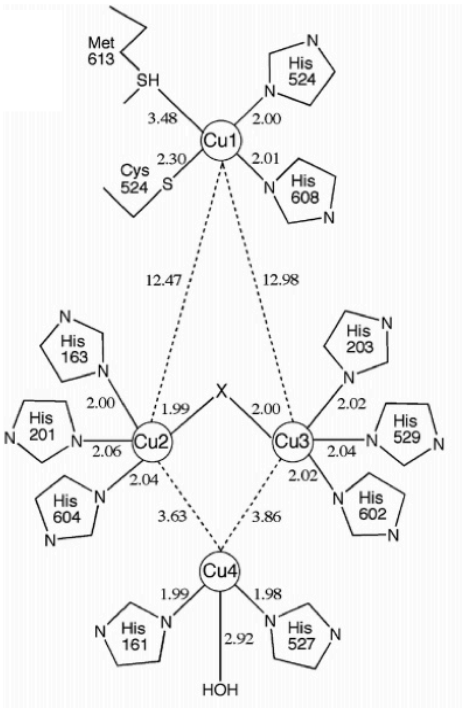

Figure 7. Active site of PHS showing a type 1, type 2, and type 3 copper center motif common amongst the multicopper oxidase family. X was identified as a bridging ligand of oxygen but couldn't be assigned. PDB: 3GYR

A final defining characteristic is their general reactivity with O_2 at what is referred to as the "trinuclear cluster" (Figures 7 and 9). The type 2 and type 3 copper centers are in close proximity and together are referred to as the trinuclear cluster.[7]. Even though the 3 copper ions are in close vicinity and they communicate with each other by electron transfer during the reaction mechanism, they are not coupled as closely as the two copper ions in a T3 center are. They are therefore considered a cluster of T2 and T3 copper centers, and not a unique copper center. It is at this trinuclear cluster where all multicopper oxidases similarly carry out their reactions with O_2.

As mentioned above, PHS couples the six e^- oxidation of oAP to the four e^- reduction of 3/2 molecules of O_2. The T1 center accepts electrons from substrate, then transfers it along a cysteine-histidine pathway, to the trinuclear cluster (Figure 8).[3,7] This flow of electrons functions to keep the three copper atoms of the trinuclear cluster in the reduced Cu^{1+} form. When the trinuclear cluster is reduced, it is in the necessary state to reduce O_2 to H_2O.[5] First, a molecule of O_2 enters the trinuclear cluster, where it undergoes its first two e^- reduction to the HOO^-, hydroperoxo intermediate via a two e^- transfer from the two Cu^{1+} ions in the T3 site (Figure 9).[7] Once in the peroxide intermediate form, a 2^{nd} two e^- reduction occurs and two hydroxides result via e^- transfers from the T2 site and a 4^{th} e^- from the T1 center (Figure 9).[7] Both hydroxides pick up an H^+ to form two H_2O molecules,[7] and all the copper ions are oxidized to Cu(II). The cycle continues with the substrate induced reduction back to Cu^{1+} (Figure 9).

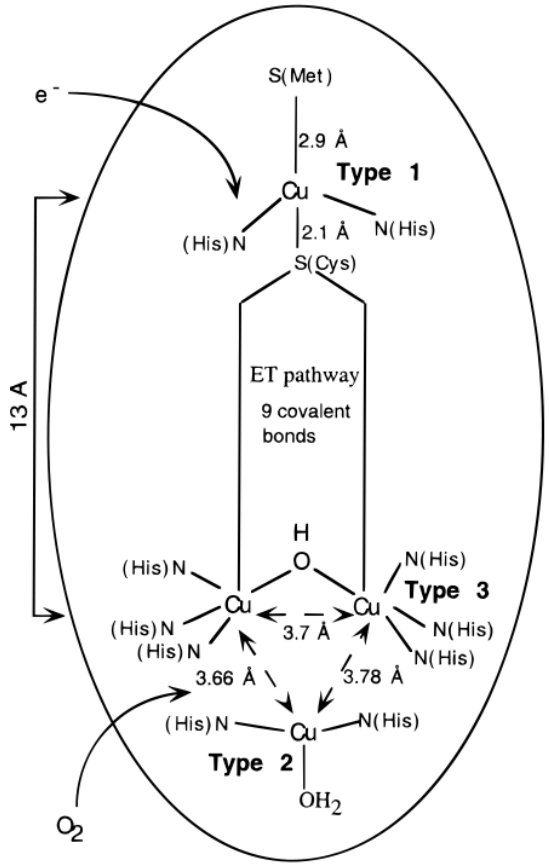

Figure 8. Active site of typical multicopper oxidases containing 1 T1, 1 T2, and 1 T3 copper center. The T1 site is located ~13 Å away from the T3 center of the trinuclear cluster, where an e^- enters the active site from the substrate and is shuttled to the T2/T3 trinuclear cluster to reduce O_2 to water. ET stands for electron transfer in the figure.

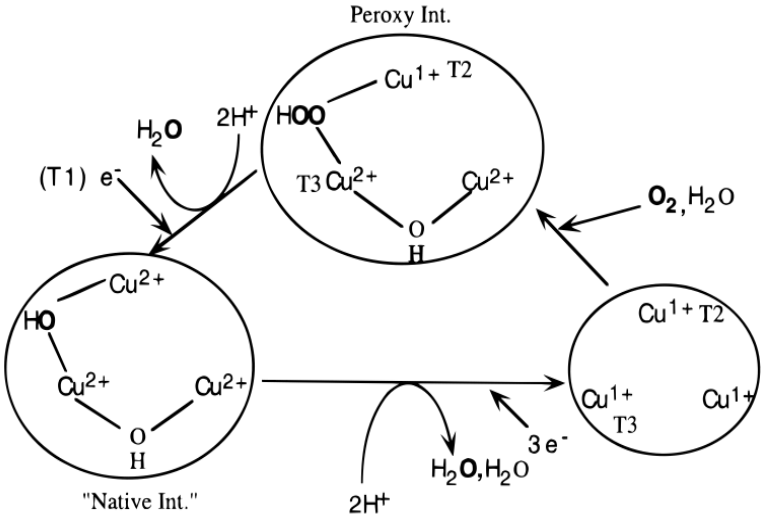

Figure 9. A closer look at the T2/T3 trinuclear cluster and its reaction with O_2. Oxygen proceeds through the peroxide, then the hydroxide fully reduced form for an overall 4 e^- reduction. The start of the reaction is the bottom right phase where all coppers are reduced and molecular oxygen enters the system.

A part of this work was to investigate copper proteins' reaction with O_2. Molecular oxygen is capable of accepting four electrons to be fully reduced to H_2O. To investigate this, we have examined our proteins' activity using both O_2 and a peroxide shunt as oxidants. To maximize our activity and understand our systems' reactivity we started with the already two e^- reduced form of O_2, by using a hydrogen peroxide species as the oxidant (Figure 10). This allows us to bypass the initial two electron reduction of O_2 (Figure 10) and start with a more reactive peroxide to catalyze the conversion of oAP to APX. This is known in the literature as using a "peroxide shunt".[19]

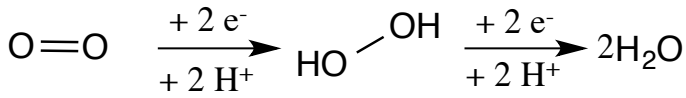

Figure 10. Illustration of the reduction of molecular oxygen through the 2 e^- reduced peroxide intermediate, then the 4 e^- completely reduced water form.

The goal of the work in this section was to study the PHS activity of our copper protein model systems in azurin, which required the development of a PHS assay. In developing this assay, we were able to gather data using multiple azurin variants that contain an additional T2 copper site on top of the naturally existing T1 copper site. These "parent" mutants were assayed, along with variants containing more T1 copper site mutations that had varied reduction potentials. These produced significant differences in reactivity. In addition, another goal of this work is to investigate the mechanism of the PHS enzyme by using our model series to study. The assay that was developed is described in section 2.1 and the results are described in section 3.1-3.3.

1.2 Peptidylglycine α-Hydroxylating Monooxygenase (PHM) as an Oxidoreductase T2 Copper Protein

Peptidylglycine α-hydroxylating monooxygenase (PHM) is an oxidoreductase protein that is part of the bifunctional enzyme, peptidylglycine α-amidating monooxygenase (PAM) complex.[20,21] PHM catalyzes the hydroxylation of the alpha carbon of peptidyglycine that then reacts with the PAM complex to generate the final amidated peptide (Figure 11).[22]

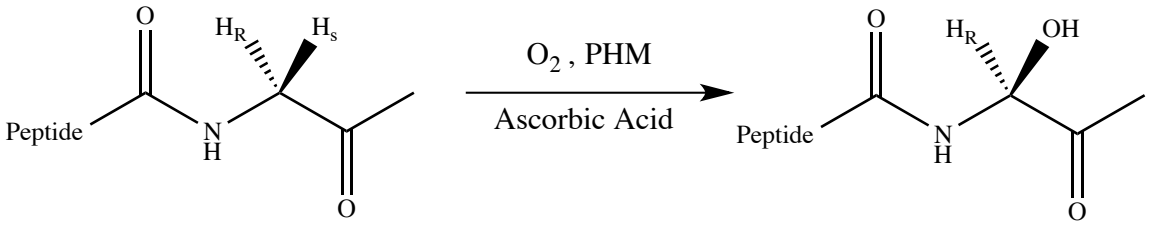

Figure 11. Enzymatic reaction of PHM showing the stereoselective hydroxylation of the Pro-S hydrogen of the α-carbon on peptidylglycine.

The PAM complex is responsible for the amidation of many peptides, making them 1000 times less likely to be consumed by proteolytic enzymes and converting them into neurotransmitters and peptide hormones (Figure 12).[23,24]

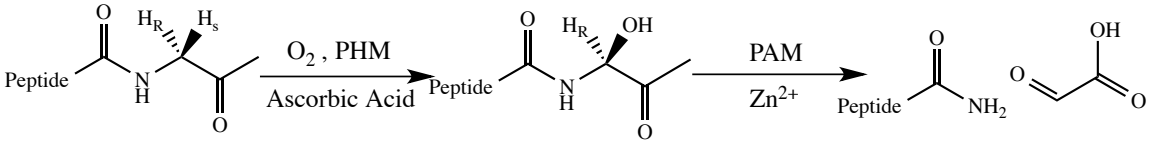

Figure 12. Enzymatic reaction of the PAM complex showing the initial hydroxylation by PHM and the amidation of a peptide by PAM.

PAM is the sole enzyme to carry out this reaction that is vital to the generation of neurotransmitters and peptide hormones pivotal to organism development and survival.[25] Deletion of the PAM gene in mice is lethal at the embryonic stage of mice.[25] This family of enzymes is commonly involved in neurotransmitter generation as the related oxidoreductases, dopamine β-monooxygenase (DβM) converts dopamine to

norepinephrine and tyramine b-monooxygenase generates hormones in insects.[20,21] The most common source of PHM is mammals as its role in the nervous system is critical. It is commonly purified from hamster ovaries.[26] The PHM gene is also found in *Planaria* and *Cnidarians*[27], which have a very primitive nervous system, further showcasing its importance in the generation of neurotransmitters.

PHM contains two T2 copper centers, one denoted as the Cu_H and the other as the Cu_M site.[27-30] From the crystal structure of PHM the Cu_H site is coordinated by 3 histidines and the Cu_M site is coordinated by two histidines, one methionine, and one water (Figure 13).[29] Both copper centers differ not only in their coordination but also in their geometry. The Cu_H site has a distorted T-shaped geometry, while the Cu_M site has a distorted tetrahedral geometry.[31] The Cu_M is the site where O_2 or solvent water binds.[31] The two copper(II) centers are separated by a distance of 11 Å through a peptide binding pocket as determined from the PHMcc crystal structure. It is believed, yet debated, that the catalytic copper site is the Cu_M site, with the Cu_H site being responsible for e^- transfer to the Cu_M site.[27-30]

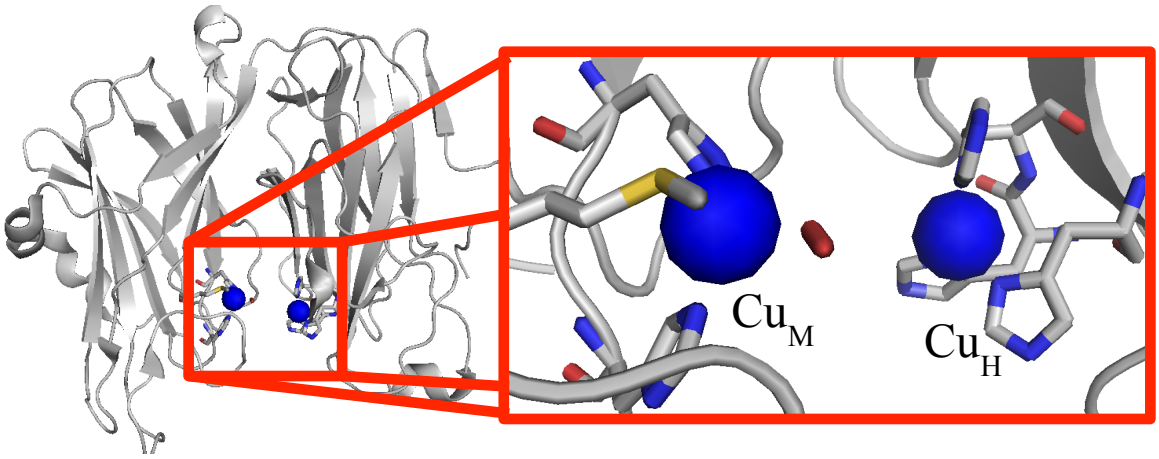

Figure 13. Crystal structure of PHMcc showing the active site of PHM. The Cu_H site is coordinated by three histidines and is 11 Å away from the Cu_M site coordinated by two histidines and one methionine. This image was generated in Pymol.[54] PDB = 1SDW

The hypothesized mechanism of PHM is shown in Figure 14.[27] In the active enzyme, both coppers begin in the reduced Cu^{1+} state when O_2 and substrate bind simultaneously (Figure 14). The first transition state involves a one e^- transfer from the Cu_M site where the O_2 binds, to O_2 forming a copper superoxide species (Figures 14 and 15). Once the Cu(II)-superoxide has formed, another e^- could be transferred to the Cu_M site from the Cu_H site to form a Cu(I)-superoxo or a Cu(II)-peroxo intermediate . It is currently believed that the Cu_M(II)-superoxo species is the active species. Regardless, the reactive Cu-O_2 species then extracts the pro-S hydrogen of the peptidylglycine substrate leaving a radical species on the α-carbon and allowing for further hydroxylation of the substrate. There is debate in the field whether or not the reaction actually proceeds through the superoxo species, but rather goes straight to the peroxo species.

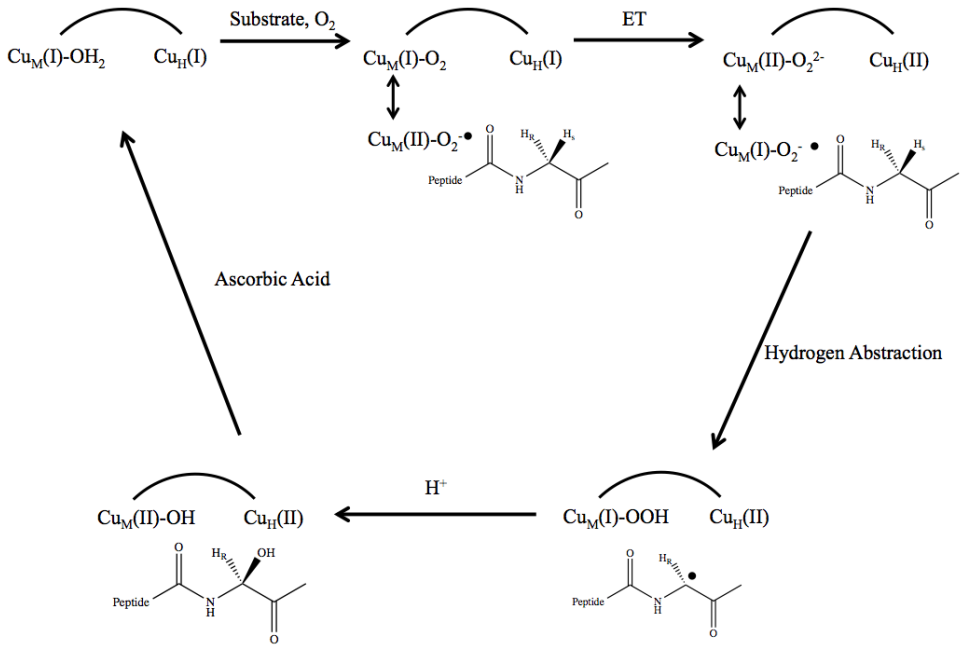

Figure 14. Proposed Mechanism of the hydroxylation of the α-carbon of peptidylglycine by PHM. ET stands for electron transfer in the reaction mechanism. Adapted from reference 27.

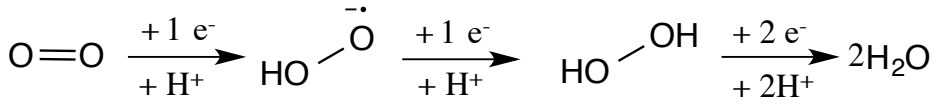

Figure 15. Illustration of the reactive species of oxygen, beginning with molecular oxygen, proceeding through the 1e$^-$ reduced superoxide, 2 e$^-$ reduced peroxide, and fully reduced water species.

In addition to modeling PHS, one of the goals of my work was to model the oxidoreductase PHM. To assess activity, we attempted hydroxylation assays similar to what is found in the literature[32], which will be discussed in section 2.3. These assays involved monitoring oxygen consumption, product hydroxylation, and the oxidation state of T1 center in azurin (via the 625 nm absorption peak). The peptidylglycine species used as a substrate was hippuric acid, shown in Figure 16. The results from these hydroxylation assays will be discussed in section 3.6.

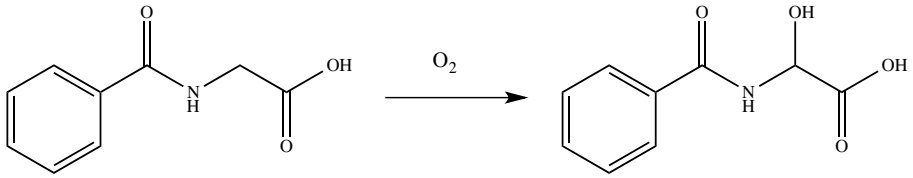

Hippuric Acid alpha-Hydroxy Hippuric Acid

Figure 16. Peptidylglycine, hippuric acid, used to assay PHM activity and its product, α-hydroxy hippuric acid. Hippuric acid is naturally found in horse urine and is not native in the cell. It is used to study PHM because of the resemblance to a glycine amino acid.

1.3 Azurin as a Scaffold Protein

To model the activity of both PHS and PHM, we used a model system. Instead of a traditional inorganic synthetic model, we chose to use azurin as a scaffold protein to build upon. Azurin is a small 14 kDa, 128 amino acid electron transfer copper protein found in *Pseudomonas aeruginosa*. The 3D structure of azurin is that of a β-barrel arranged in a double wound Greek key topology with two beta sheets and a small alpha helix.[33,34] It has a native T1 copper site that is coordinated by two histidines, one cysteine, one methionine, and a weak long distance interaction with the carbonyl backbone from a nearby glycine residue (Figure 17).[18] The T1 copper site in azurin has a distinctive charge transfer band in the absorbance spectrum from the S(cys) pπ → Cu $3d_{X^2-Y^2}$ transition[15,16] at 625 nm (molar absorptivity 5000 M^{-1} cm^{-1}). When the Cu(II) in the T1 site is reduced to the Cu^{1+} state it no longer has the absorbance at 625 nm.

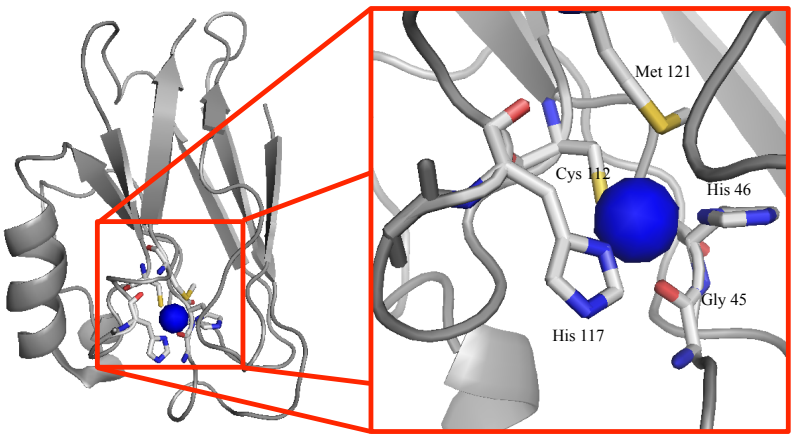

Figure 17. Wild type azurin crystal structure 4AZU, with a zoomed in view of the T1 copper electron transfer site residues. This image was generated in Pymol.[54]

In all of the azurin models, we used the naturally occurring T1 site to function as an electron transfer site along with an added T2 surface copper site (Figure 18). To create the models' additional copper binding site, we mutated amino acids to copper coordinating histidine and methionine residues. We chose this method of protein re-design rather than building an amino acid sequence from the ground up, or the de novo approach[36] to build a protein model. By starting with a stable protein scaffold with an existing T1 copper center, we had a robust base to work with. This allowed us to create variants of both the T2 center and manipulate the naturally existing T1 center to further probe structure-function relationships.

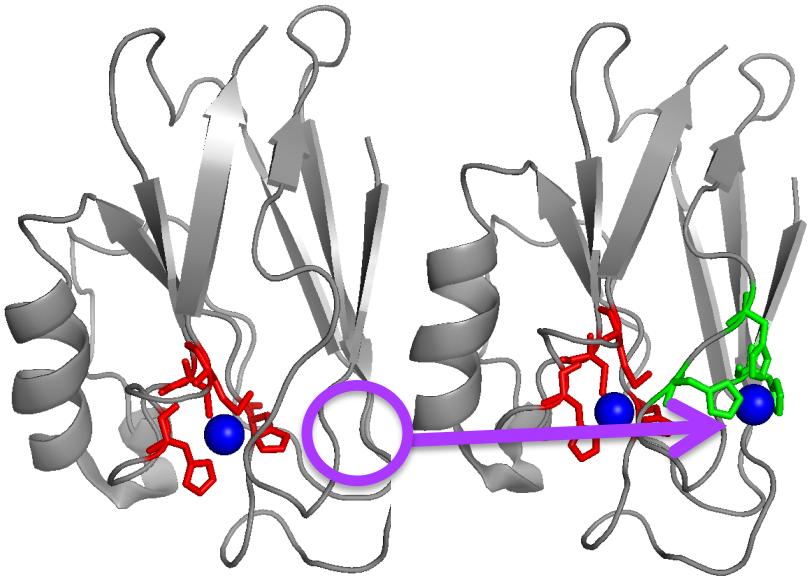

Figure 18. WT Az crystal structure 4AZU left, cartoon of a mutated T2 copper center in azurin on the right, green residues depict the incorporated surface copper binding site. Image was generated in Pymol.[54]

1.4 Azurin Models: The Parent Mutants

The T2 copper centers designed in azurin were chosen based on a couple of naturally existing non-coupled dinuclear copper proteins. The oxidoreductase proteins PHM and nitrite reductase (NiR) have catalytic T2 copper centers that we modeled our

variants after. As described before, the active site of PHM has a T2 copper center with two histidines and one methionine at its Cu_M center.[27-31] We chose this copper center as one to mimic for our first T2 center parent mutant. In order to accomplish this, the mutations Gln8Met, Gln14His, and Asn16His were made. The second parent mutant named PHM3His has all of the same mutations, except all three residues were mutated to histidines. This mutation was made using all histidines to more closely resemble a typical T2 copper center with the geometry of the Cu_M site in PHM. Cartoons of these mutations are shown in Figure 19.

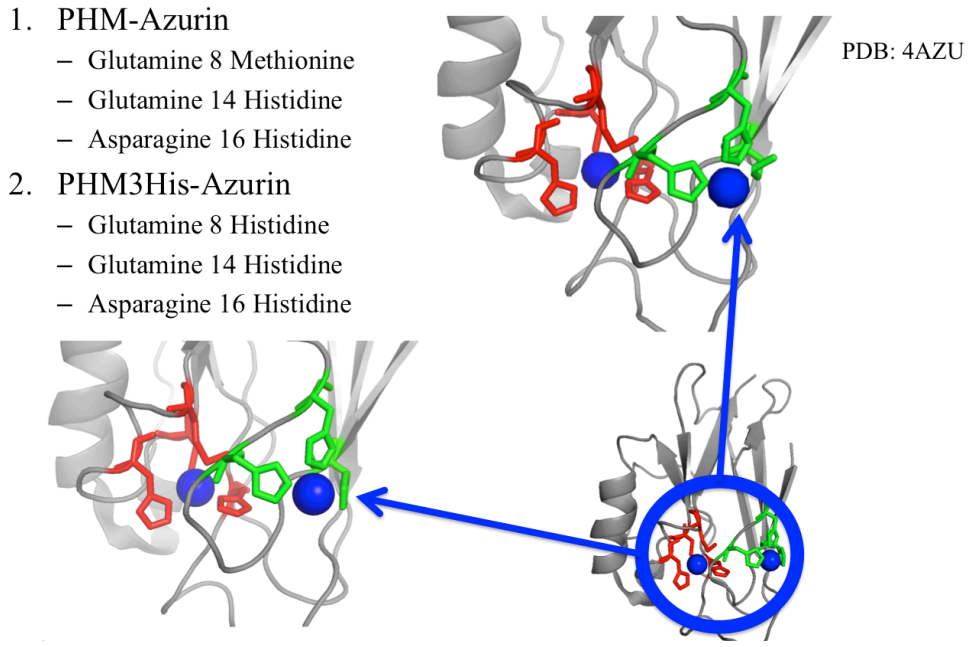

Figure 19. Cartoons of the T2 copper center parent mutants, PHM and PHM3His, designed after the active site of PHM. This image was generated in Pymol.[54]

The second noncoupled dinuclear copper protein we chose to replicate in our model was the T2 center in NiR. NiR has a T1 copper center for electron transfer and a T2 center for catalyzing the conversion of NO_2^- to NO.[37-39] This T2 center is coordinated by three histidines and has an aspartate near the active site for substrate binding.[37-39] To mimic the T2 center in NiR we incorporated a T2 surface copper into azurin by mutating

Asn10His, Gln14Asp, and Asn16His. This parent mutant, named NiR, was made to mimic the histidines in the active site and incorporate the aspartate into the active site. The final parent mutant we created was named NiR3His, where all the same amino acids in NiR were all mutated into histidines. This was to directly mimic the T2 site in NiR and resemble that of a typical T2 site coordinated by three histidines. Cartoons of these mutations are shown in Figure 20.

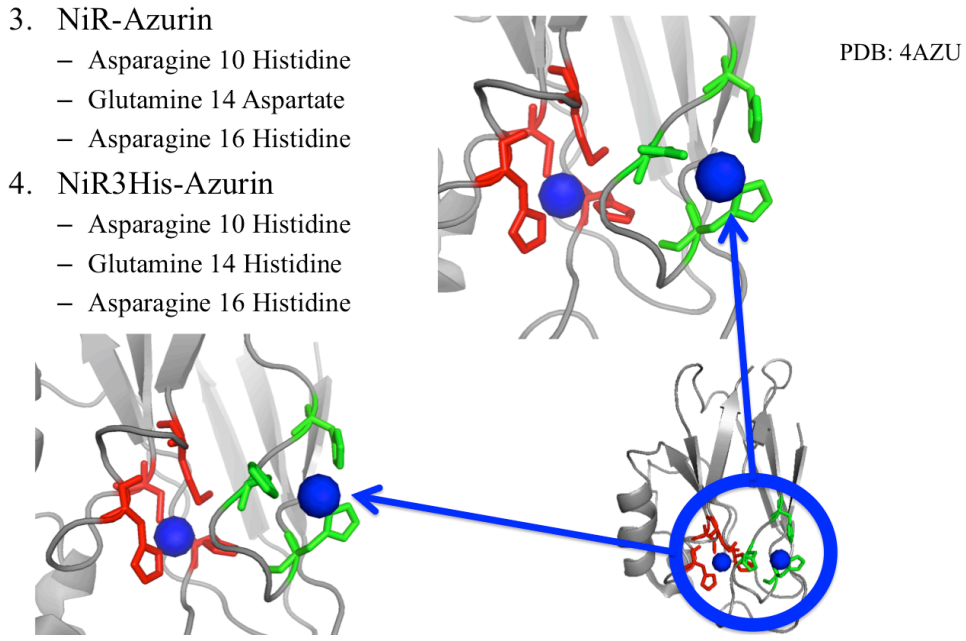

Figure 20. Cartoons of the parent mutants NiR and NiR3His, designed after the active site of the oxidoreductase protein nitrite reductase. This image was generated in Pymol.[54]

All of these variants were assayed using the developed PHS assay developed in section 2.1 and their results will be discussed in section 3.2 - 3.5. After all these variants were tested, we examined other aspects of protein design to improve the reactivity of our system. These approaches are referred to as the second generation variants.

1.5 Azurin Models: Second Generation Variants

The cupredoxin class of proteins, also known as electron transfer copper proteins, all contain a T1 copper center coordinated in a similar manner with at least two histidines and one cysteine.[35] An interesting aspect of these copper ion centers is the wide variation in their reduction potentials, spanning 100-1000 mV.[35] For example, stellacyanin has a reduction potential of 184 mV[40], rusticyanin has a reduction potential of 680 mV[41], and human ceruroplasmin having a reduction potential over 1000 mV.[42] The variability in reduction potentials comes from both primary coordination sphere electrostatics as well as secondary coordination sphere effects. It has been shown that the secondary coordination sphere can affect the reduction potential of azurin by as much as 30 mV per phenylalanine addition.[35]

In addition to secondary coordination sphere reduction potential tuning, one can tune reduction potentials using the primary coordination sphere. This approach directly manipulates residues that are either coordinated to the copper in the T1 center, or affect neighboring residues that stabilize the copper interactions.[43] The disruption of this coordination sphere can allow the copper atom to be oriented differently in the binding pocket and give different spectroscopic and electrochemical properties.[43] Two known ways to tune reduction potentials in azurin are the mutations Phe114Pro and Met121Gln.[44,45] Both of these mutations disrupt the primary coordination sphere of the T1 copper center in azurin and decrease the reduction potential. The Phe114Pro mutation in azurin has been shown to decrease the reduction potential by ~ 90mV.[44] This mutation causes a reorganization of the hydrogen bonding network near the copper center of azurin. The loss of the phenylalanine eliminates a direct hydrogen bond to Cys112,

which in turn increases the electron density on the sulfur ligand, and causes a decrease in the reduction potential (Figure 21).[43-45]

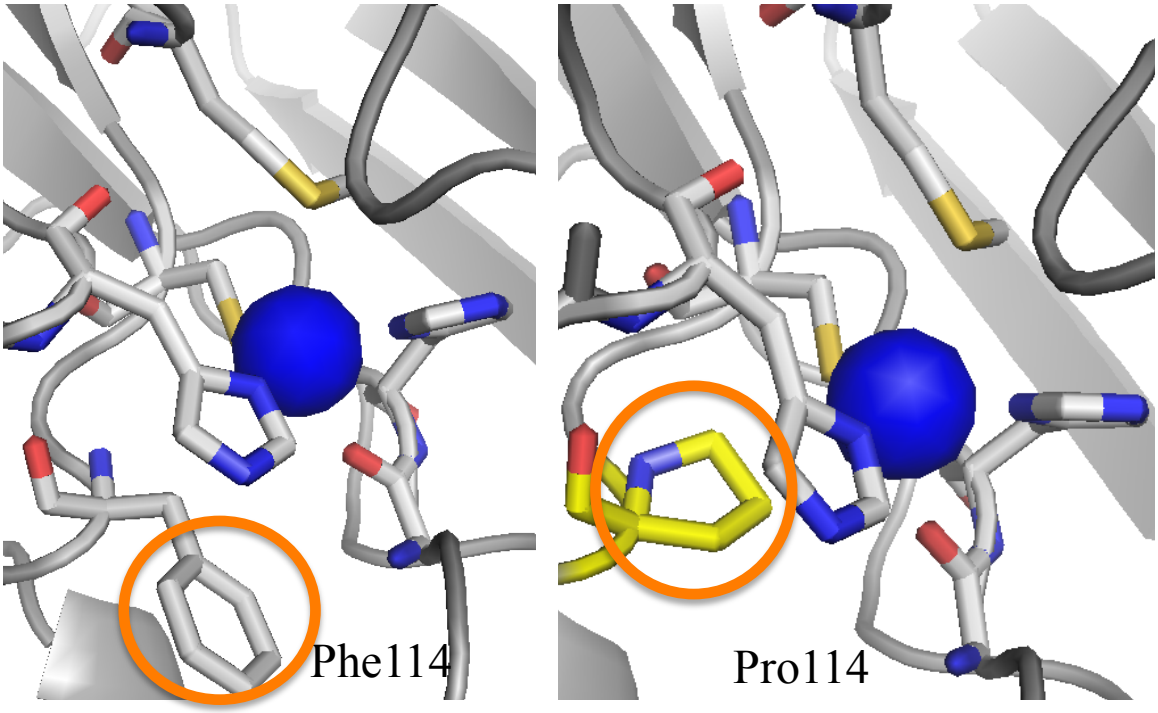

Figure 21. Cartoon of the Phe114Pro mutation to the T1 site of azurin on right. Shown on the left is the native Phe114 residue from crystal structure 4AZU, and the right is the mutated Pro114, both circled in orange. This mutation is known to decrease the reduction potential of the copper site by ~100 mV. This image was generated in Pymol.[54]

In addition to the Phe114Pro mutation to the primary coordination sphere to decrease the reduction potential, it is known that mutating the axially bound methionine to the T1 site will decrease the reduction potential. Methionine in this case can be mutated to glutamine and will have the same effect as the Phe114Pro mutation. The Met121Gln mutation disrupts a hydrogen bond from Phe114 to Cys112 to decrease the reduction potential like that of Phe114Pro by ~100 mV (Figure 22).[43-45]

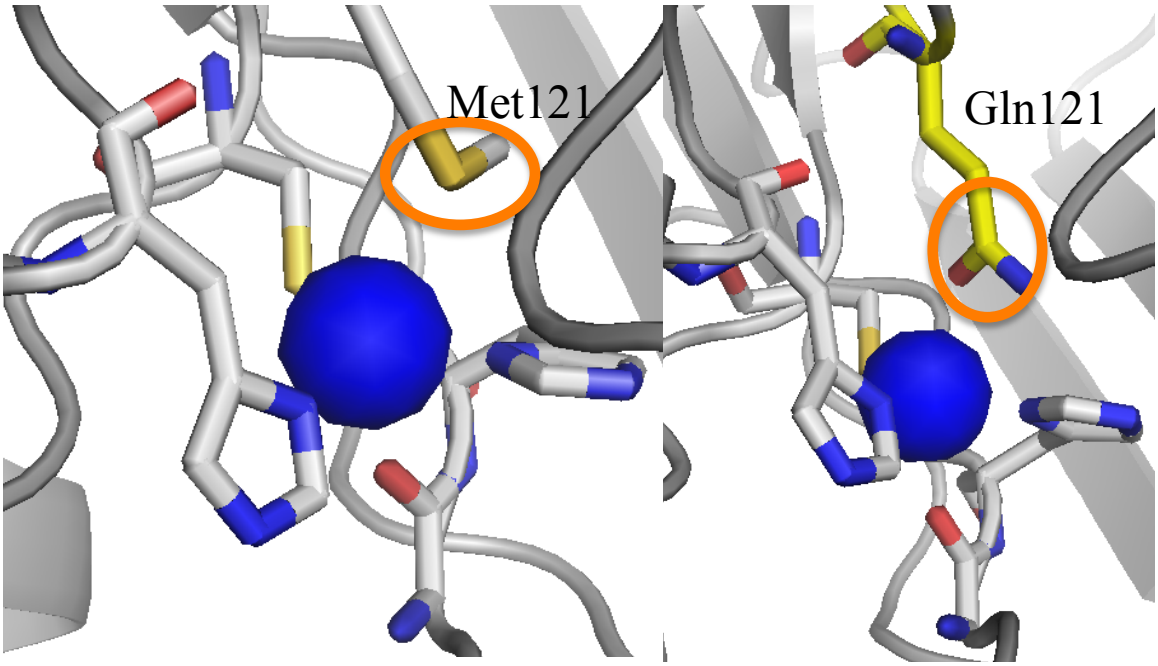

Figure 22. Cartoon of the Met121Gln mutation to the T1 site of azurin on right. Shown on the left is the native Met121 residue from crystal structure 4AZU, and the right is the mutated Gln121, both circled in orange. This mutation is known to decrease the reduction potential of the copper site by ~100 mV. This image was generated in Pymol.[54]

These mutations give us the ability to tune our systems' T1 copper center reduction potential. One of the strategies we have used to maximize our systems' activity in the PHS activity assay has been to utilize the mutations described above as well as an additional mutation. In addition to the variance in T1 copper centers discussed above, another reason for tuning the reduction potential to increase activity comes from the native NiR system that two of our models are based on. The native T1 center in NiR has a reduction potential of about 250 mV,[37-39] where as the reduction potential of azurin is about 360 mV.[35] Because of this, we have created variants that decrease the reduction potential of our T1 copper center to have a reduction potential closer to native NiR.

For our second generation mutants thus far, we have described strategies used to tune the reduction potential of the T1 copper center only. Our last rational design strategy for our second generation mutants involves the creation of an electron transfer

wire between our T1 and T2 surface copper site. Native PHS has a 13 Å Cis-His electron transfer pathway from the T1 to T2/T3 trinuclear cluster that facilitates electron transfer[2,7] and native NiR has a His-Cys network that functions in the same manner.[37-39] In order to mimic an electron transfer pathway, we have mutated Phe15Trp (Figure 23). Tryptophan has been shown to facilitate and speed the transfer of electrons across distances as much as 20 Å.[46]

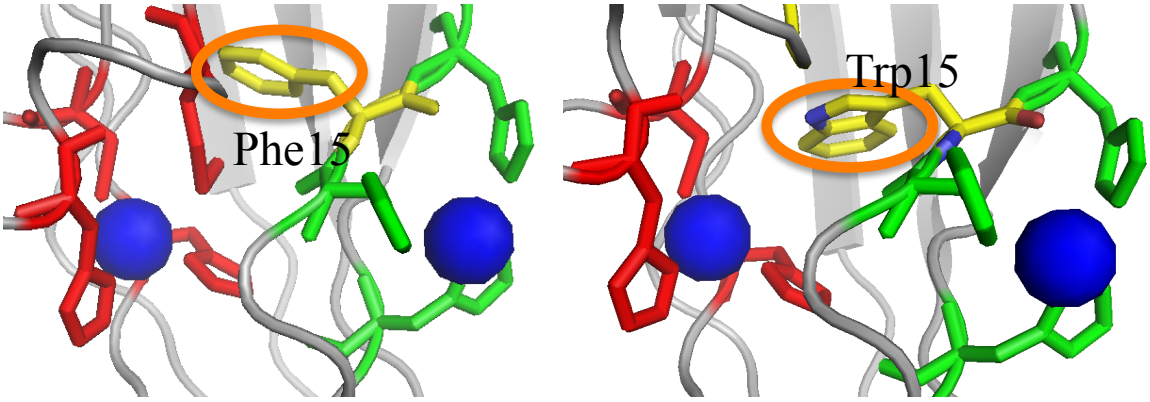

Figure 23. Cartoons of the Phe15Trp mutation in our NiR3His azurin model, named NiR3His F15W. Shown on the left is the native Phe15 residue and the right is the mutated Trp15, both circled in orange. This image was generated in Pymol.[54]

Our second-generation mutants consist of the three mutations described above. We have combined all of our parent mutations with Phe114Pro, Met121Gln, and Phe15Trp as shown in figures 23, 24, and 25. These variants have been named the "single" mutants due to their one second generation mutation to the preexisting parent mutations.

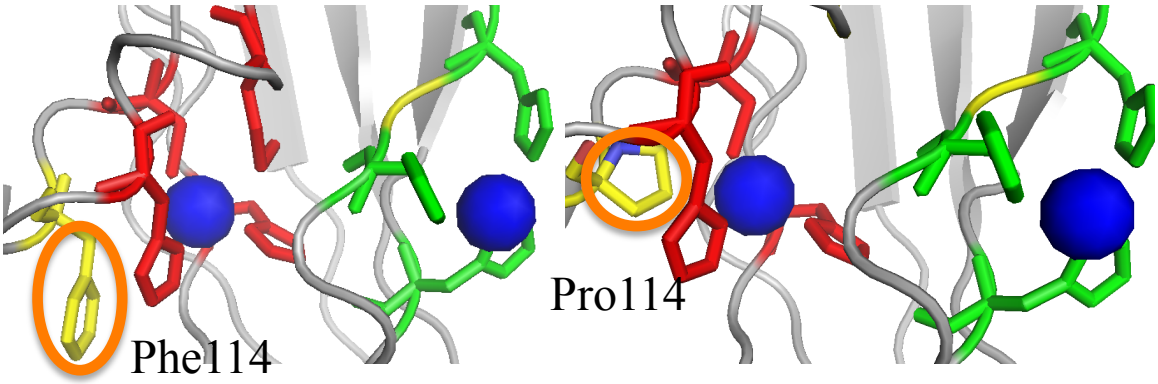

Figure 24. Cartoon of the Phe114Pro mutation in our NiR3His azurin model, named NiR3His F114P. Shown on the left is the native Phe114 residue and the right is the mutated Pro115, both circled in orange. This image was generated in Pymol.[54]

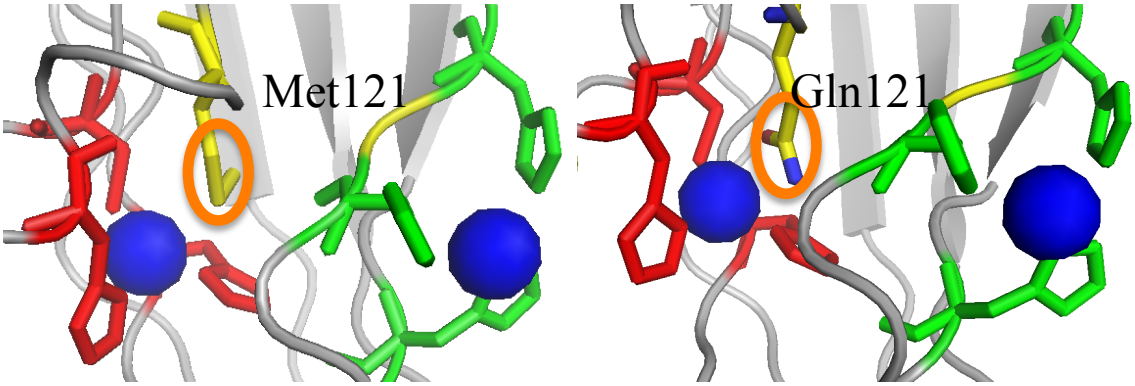

Figure 25. Cartoon of the Met121Gln mutation in our NiR3His azurin model, named NiR3His M121Q. Shown on the left is the native Met121 residue and the right is the mutated Gln121, both circled in orange. This image was generated in Pymol.[54]

In addition to the single mutants, three "double" mutants were created to incorporate all three possible pairs of 2nd generation variations with the parent mutants. Studies have shown that when the Phe114Pro and Met121Gln mutations are combined, the decrease in reduction potential for variant decreases in an additive manner, and the native WT azurin reduction potential is about 200 mV.[35,40,41] The double mutants have been named Phe114ProMet121Gln, Phe114ProPhe15Trp, and Met121GlnPhe15Trp. Example cartoons are shown in figures 26, 27, and 28.

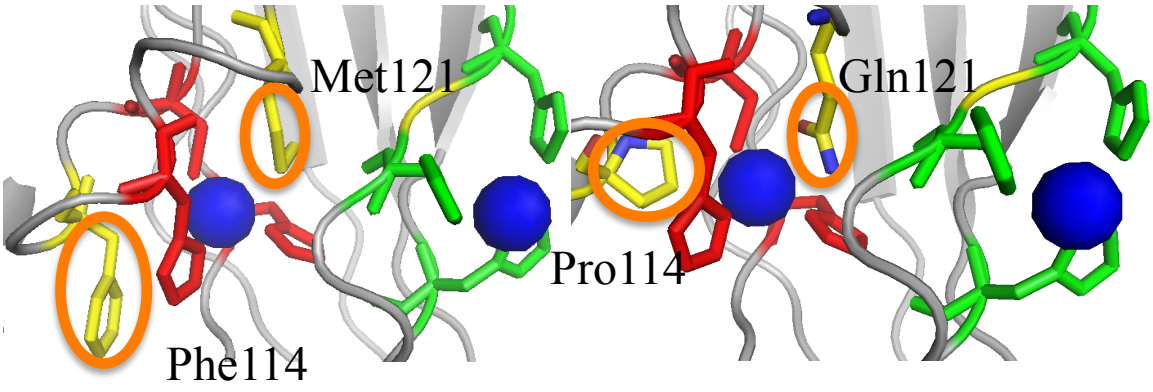

Figure 26. Cartoon of the Phe114ProMet121Gln mutation in our NiR3His azurin model, named NiR3His F114PM121Q. Shown on the left are the native Phe114 Met121 residues and the right are the mutated Gln121 Pro114, all circled in orange. This image was generated in Pymol.[54]

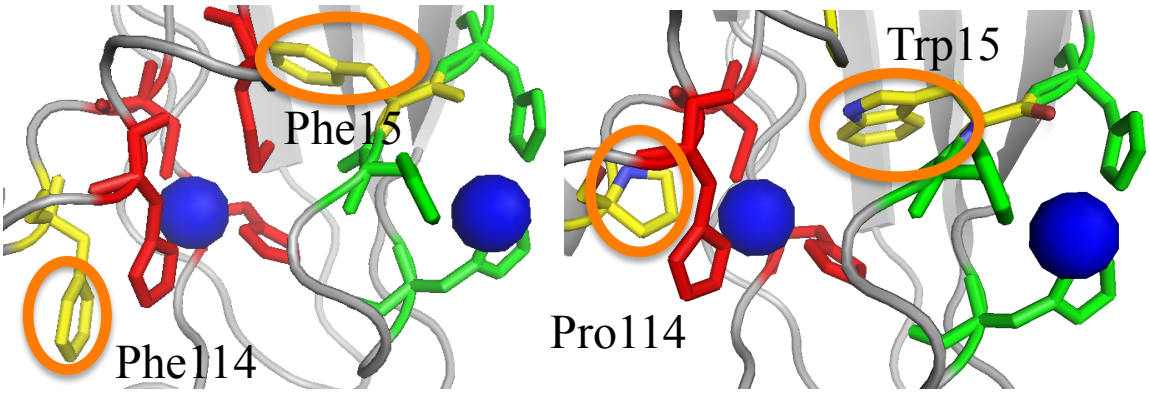

Figure 27. Cartoon of the Phe114ProPhe15Trp mutation in our NiR3His azurin model, named NiR3His F114PF15W. Shown on the left are the native Phe114 Phe15 residues and the right are the mutated Pro114 Trp15, all circled in orange. This image was generated in Pymol.[54]

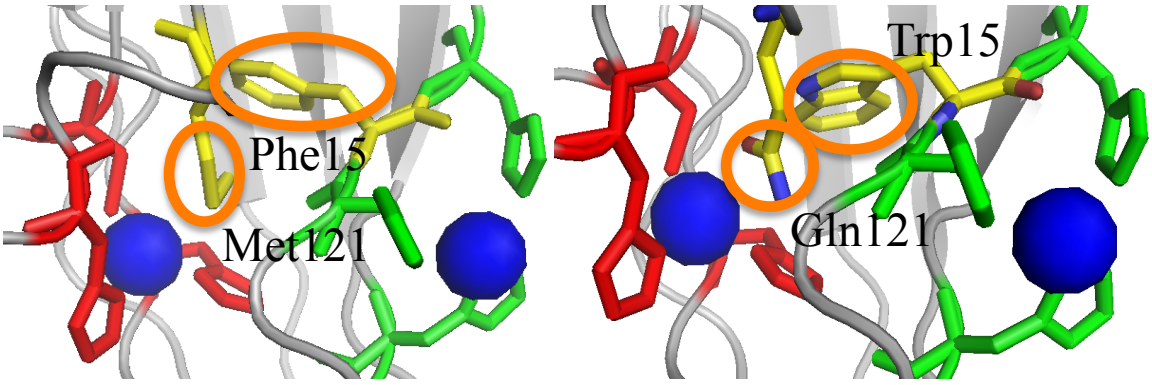

Figure 28. Cartoon of the Met121GlnPhe15Trp mutation in our NiR3His azurin model, named NiR3His M121QF15W. Shown on the left are the native Met121 Phe15 residues and the right are the mutated Gln121 Trp15, all circled in orange. This image was generated in Pymol.[54]

The final second generation mutant that has been made is the "triple" mutant where all three mutations have been added to the parent mutations. Thus named Phe114ProMet121GlnPhe15Trp and shown in Figure 29. These variants have an electron transfer wire and the most decreased T1 copper center reduction potential.

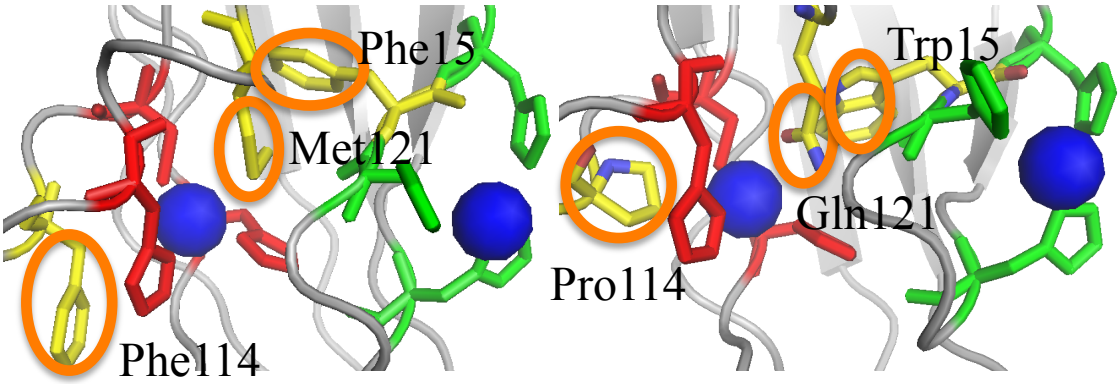

Figure 29. Cartoon of the Phe114ProMet121GlnPhe15Trp mutation in our NiR3His azurin model, named NiR3His F114PM121QF15W. Shown on the left are the native Phe114 Met121 Phe15 residues and the right are the mutated Pro114 Gln121 Trp15, all circled in orange. This image was generated in Pymol.[54]

All the azurin variants described herein have been generated and characterized with UV/Vis and EPR spectroscopy by previous students in our lab. We used all these variants to gain more insight into the copper protein structure-function relationship by testing their activity in assays such as the PHS or PHM assays. We manipulated both structural and electronic features of our copper centers in an attempt to learn more about their integrated functions in their native systems and ultimately protein design.

1.6 Wild Type Azurin Crystallography:

To gain more insight into our azurin protein structure and function relationships, our lab undertook a crystallography study with our variants. Crystal structures give us insight into our mutants as another method of characterization in addition to UV/Vis and EPR spectroscopy. With the additional information crystallography provides, we can characterize our protein by directly examining the structure. However, the process involved to get a crystal structure can be long and tedious. One must first grow the crystal, then dehydrate correctly, pin and cryoprotect the crystal, and finally gather a solvable dataset.

To grow our crystals, we utilize the hanging drop method (Figure 30). This method uses a sealed chamber with 1 mL reservoir solution below a hanging droplet of reservoir solution mixed with purified protein.

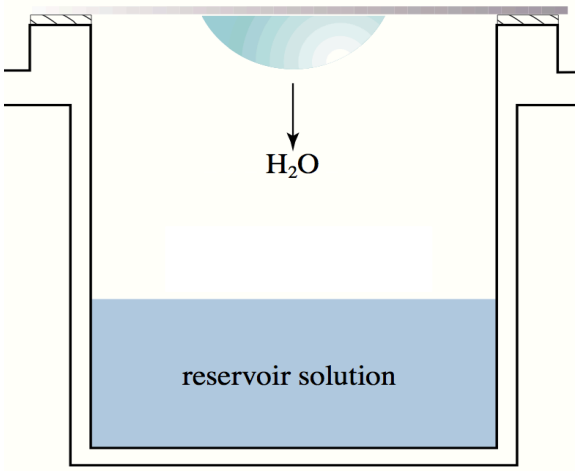

Figure 30. Example diagram of the hanging drop method of growing protein crystals. As the box ages, the concentration of analyst in the hanging drop increases and the protein crystal grows in an ordered manner.

It is important to have a pure sample of protein,[47] as any impurities will disrupt the protein crystallization to either cause disorder or lack of crystallization. The reservoir is then placed into a thermally controlled environment to grow crystals. As the box ages,

water in the droplet will evaporate and condense in the reservoir at a controlled rate, creating a supersaturated environment, until the protein in the hanging droplet reaches a point of precipitation. This can result in the protein crystallizing out of solution. However, to grow a good crystal, one must have the crystal precipitate out of solution in an ordered manner to avoid amorphous precipitation as illustrated in Figure 31.

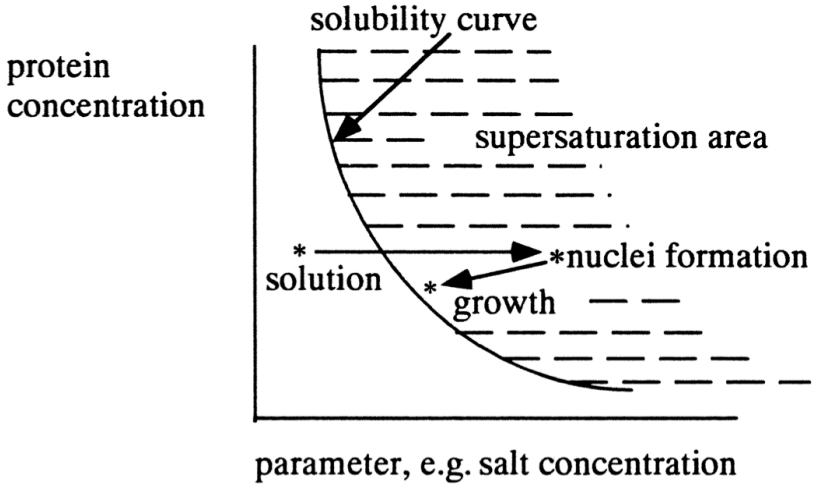

Figure 31. Protein solubility curve as a function of protein concentration and a precipitating factor to illustrate the importance of supersaturation and where crystal growth occurs, adapted from reference 48.

There are many different ways to cause precipitation when it comes to crystallography. We grow our crystals using a combination of salt ionic effects and a precipitating agent. The precipitating agent is usually polyethylene glycol (PEG), and our salts vary between $LiNO_3$ and $CaCl_2$. PEG molecules cannot approach a protein molecule at a distance any closer than the PEG's radius, therefore an inaccessible layer for PEG surrounds the protein molecules. When the protein molecules begin to aggregate alongside the PEG, the inaccessible area becomes smaller. As a result of this, the accessible area becomes larger and facilitates ordered packing of protein molecules. Salt on the other hand facilitates crystallization in an additional two ways. The first is the salt ions crowd the areas on the protein where ionic charge exists, and therefore weaken ionic

repulsion forces. The second effect salt has is to immobilize the water in solution by the salt hydration, which reduces solubility of the protein. Both of these chemicals work in tandem to force the protein molecule to aggregate by competing with the protein to stay in solution and causing the protein to precipitate.[48]

When a protein precipitates in the hanging drop method, the goal is to have ordered monocrystals form, meaning one continuous crystal with one unit cell packing in an organized manner. To grow monocrystals that are worthy of collecting a dataset from, many iterations on the growth conditions are often tried. This includes varying buffer, pH, excess copper source in our case, and precipitating agent. We optimize conditions in droplets to give few nucleation sites resulting in big, dark blue (more concentrated azurin) crystals, with well defined edges. We aimed to grow a crystal that was sufficient for a complete dataset to be collected. A sufficient crystal will have packed well enough to diffract out past 2 Å and have a mosaicity less than 0.5 °.

A common problem with protein crystallography is the inherit disorder associated with proteins and an aqueous environment. Proteins are floppy and in constant movement with varied water pockets between proteins in a crystal. Water tends to not pack well in a protein crystal, which creates disorder and increases mosaicity. A highly disordered crystal is bad for diffraction as it is less likely for protein molecules to align, which in turn significantly reduces the resolution of the solved structure. Mosaicity is a way of quantifying this disorder. The higher the degree of mosaicity, the less ordered the crystal is.

To minimize the disorder caused by water molecules in protein crystallography, a technique known as dehydration can be used. The dehydration process has been shown

to improve the resolution of bovine serum albumin from ~8 Å to 3.2 Å and disulfide bond G protein from 10 Å to 2.0 Å.[49,50] Dehydration is a process that involves transferring a crystal from the droplet it was grown in to a more concentrated dehydration solution, to leech out water from the crystal to increase order and decrease mosaicity (Figure 32). The dehydration solution has a higher precipitating solution concentration and usually contains a cryoprotectant like glycerol. The increased precipitating solution extracts water from the crystal in a way that is aggressive enough to dehydrate it but not too aggressive as to crack or destroy the crystal. However, dehydration techniques can vary based on the quality and morphology of the crystal due to the strength of the crystal to resist cracking.[49] The removal of water increases the order of the crystal, which decreases the crystals' mosaicity, and in turn increases resolution.[49]

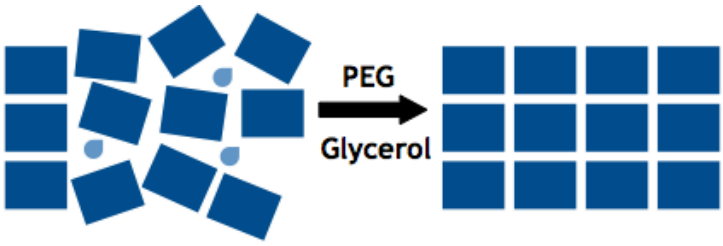

Figure 32. Visual depiction of the dehydration process that removes water from protein crystals to decrease mosaicity and increase the order of the crystal. This technique can be applied to all protein crystals.

Once the crystals have been grown and dehydrated, we then screen the crystals. Crystal screening is the process of collecting initial diffraction images to gauge whether or not the crystal is worthy of collecting a full dataset. When we screen crystals we collect two diffraction pattern images of the crystal at 90° in order to get an approximation of how well the crystal will diffract. Some qualities of a good crystal screen are low mosaicity, high resolution, high spot intensity, and the lack of ice rings. An example of a good screening crystal diffraction pattern is shown in Figure 33 for the crystal 61 D4.

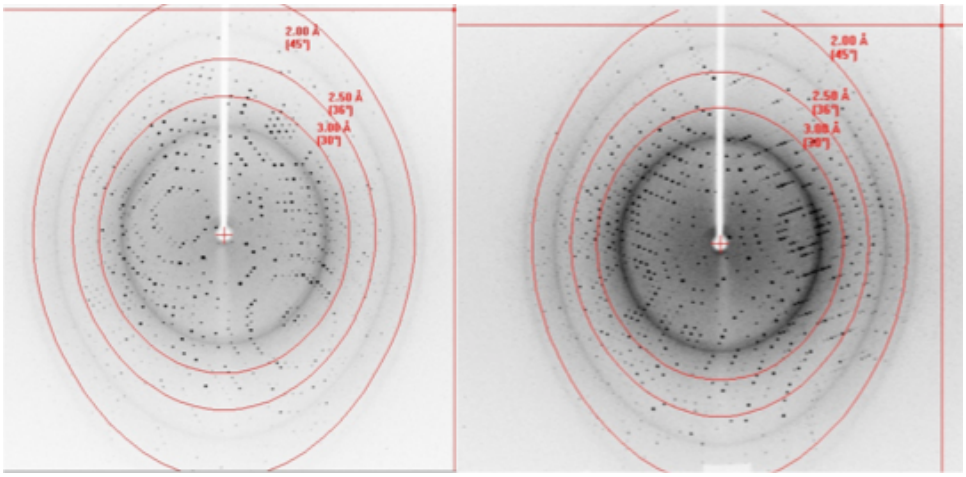

Figure 33. Example diffraction patterns from a good screening of a WT Az crystal with low mosaicity, high resolution, intense spots, and a low amount ice rings. This was done at the UMD Rigaku Rapid-II diffractometer.

Currently there are over 15 published crystal structures in the literature for azurin and its variants. The solved crystal structures have been grown anywhere from pH 3.2-8.0 in acetate, imidazole, Tris, and citric acid.[51-53] However, none of them are at pH 7.0 in Tris buffer. We set out to gain a wild type azurin structure at pH 7.0 in Tris buffer. This is an important structure to our lab so that we can compare WT azurin to other azurin variants that were crystallized under these same conditions. My goal was to determine the wild type azurin crystal structure as a control for our lab's other crystallography projects.

Chapter 2: Materials and Methods

2.1a Ortho-Aminophenol (oAP) Assay Sample Preparation:

To assess our proteins' activity, we assayed them using oxidation assays. Discussed herein are the *o*-aminophenol oxidation assay and its preparations. The goal of this was to test the azurin variants and examine differences between copper sites based on their catalysis of the conversion of *o*-aminophenol (oAP) to phenoxazinone (APX) using an oxidant. This assay produced results that will be discussed in Chapter 3.

All protein variants were purified according to an already established purification protocol.[1,2] Variants were grown in the BL21* strain of *E. Coli* bacteria (Invitrogen Corp., Carlsbad, CA). Protein growths began with a small volume (4-5 mL) growth in LB broth in the presence of Kanamycin for 4-6 h. Once the cells had grown, 1 mL of the grown cells were transferred to 4L of 2xYT (64 g bacto-tryptone, 40 g yeast extract, and 40 g NaCl) media and allowed to incubate for 12 h or until the optical density at 600 nm reached 9-10. After this incubation, 3 mM isopropyl β-D-1-thiogalactopyranoside (IPTG) was added to induce azurin expression, the cells were allowed to express azurin for 2-3 h. The cells were then separated from the media by centrifugation (7000 RPM for 10 min), suspended in a 20% sucrose solution, lysed by osmotic shock, purified with a precipitation solution (500 mM ammonium acetate pH 4.1), and further purified with cation (SP-sepharose) followed by anion (Q-sepharose) exchange columns.[3]

To prepare samples used in assays, first the T1 copper center was titrated to determine the azurin concentration by using a 100 μL aliquot of purified protein with $CuSO_4$ until the 625 nm T1 copper center absorption peak no longer increased. The maximum absorption peak was corrected for dilutions and a molar absorptivity of 5000

cm^{-1} M^{-1} was used to calculate the concentration.[3] Once a final concentration was determined, 5 molar equivalents of 0.1 M $CuSO_4$ was added to all of the protein to bind both copper binding sites (2 binding sites + 3 extra equivalents). The protein was allowed to bind copper for approximately 25 min while being stirred on ice.[3] After the protein bound copper, it was passed through a PD-10 size exclusion column packed with Sephadex G-25 Medium to remove excess copper and exchange the protein into its intended buffer. A final concentration was determined for the protein sample by measuring its 625 nm absorption peak and using the molar absorptivity. The sample was then aliquoted into 1.8 mL screw cap vials, flash frozen in liquid nitrogen, and stored in a -4 ° C freezer for future use.

2.1b Ortho-Aminophenol (oAP) Preparation:

Ortho-Aminophenol (oAP) was purchased from Fisher Scientific at 99% purity. It requires further purification as oAP auto-oxidizes with oxygen when exposed to the atmosphere to yield a brown colored contaminant.[4] In order to purify oAP, a re-crystallization was performed with benzene. Approximately 1.0 g of oAP was added to 16.0 mL of benzene and then heated to 80 °C. The solution was allowed to slowly cool to room temperature and then further cooled in an ice bath. Once cooled, it was vacuum filtered and allowed to dry on the filter for approximately 15 min with air flowing over the solid from the vacuum filter apparatus. Approximately 0.75 g of a white crystalline material was recovered from each recrystallization. The oAP was stored in the -4 ° C freezer in glass vials covered in tinfoil after streaming Ar gas over the solid for approximately 10 min to purge oxygen.

To prepare the oAP solution, approximately 10 mg of oAP was measured into a glass vial. The oAP was then dissolved in DMSO solvent (Caution! Easily dissolves in skin.) to make a final stock solution that was 100 mM oAP. All oAP solutions had to be prepared fresh each day, as the oAP oxidizes throughout the day yielding a brown solution.[4] To lessen this decomposition, each vial was covered in tinfoil and kept sealed when not in use as light and oxygen can cause the auto-oxidation of the stock solution.[4]

2.1c Ortho-Aminophenol (oAP) Peroxide Shunt Assays:

For all peroxide shunt assays[19,20], assays where H_2O_2 or tert-butyl hydrogen peroxide were used as an oxidant instead of O_2, reactions were performed in a cuvette on a Shimadzu-2401PC scanning UV-visible absorption spectrophotometer, with a thermally regulated water jacketed cuvette holder at 23 °C, while being stirred using a Variomag Telemodul magnetic stir device and 6 mm magnetic stir bar. H_2O_2 shunt reactions were performed in 2.5 mL total volume in 50 mM ammonium acetate buffer pH 5.1, where the protein was diluted to a final concentration of 10 μM. Tert-butyl hydroperoxide shunt reactions were performed in 2.5 mL of 20 mM potassium phosphate buffer pH 7.5, where the protein was diluted to a final concentration of 1 μM. All assays were monitored at 434 nm, to observe the phenoxazinone (APX)[5] formation directly. For each reaction, oAP was added to the cuvette containing protein and buffer and mixed with pipetting. To initiate the reaction 10 mM peroxide was added 18 s after the oAP, and also mixed by pipetting. Once the reaction was initiated, the absorbance was measured every 6 s for 7-10 min. At the end of the reaction, the initial linear rate was determined from the first 48-60 s of the reaction after the peroxide shunt was added, using a linear regression trend line, usually above the 99% correlation (Figure 34), and a reaction rate was determined

from the slope. Assays with H_2O_2 were performed in the oAP concentration range of 0.5 mM – 100 mM and assays with tert-butyl hydroperoxide were performed in the substrate range of 10 µM – 1000 µM oAP. All assays were performed in triplicate and fit to Michaelis-Menten kinetic models using Sigmaplot (Systat Software Inc, San Jose, CA) using a least squares analysis. From the fit, V_{max} (mM/min) and K_m (mM) were obtained and the turnover number (mmol oAP min^{-1} $mmol^{-1}$ protein) was determined. Turnover number is the amount of product formed by an enzyme in a given amount of time per total protein. We have compared our proteins' specific activity to the native Phenoxazinone Synthase (PHS) as reported in the literature to assess our activity.

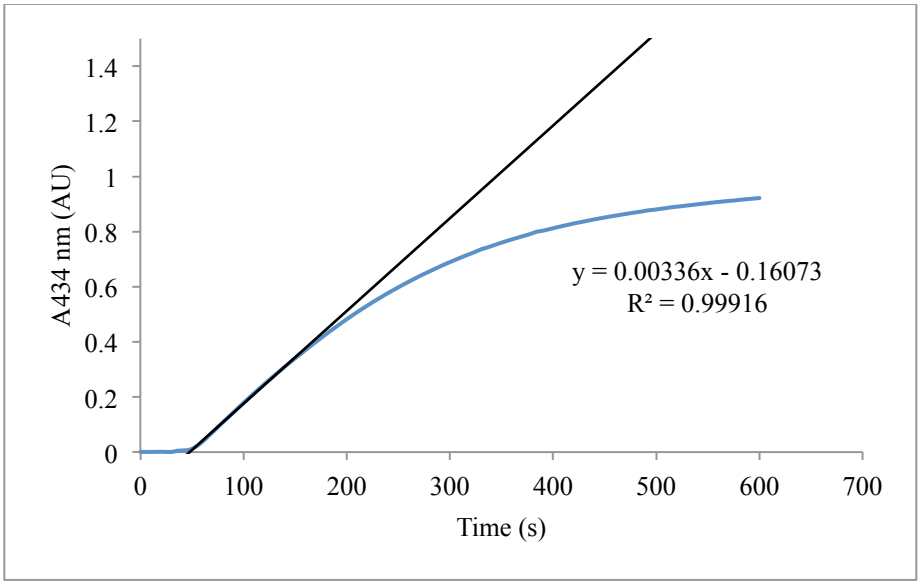

Figure 34. Typical linear fit for a single oAP assay for use in Michaelis Menten kinetics with tBHP. The example shown is 1µM NiR3His, 0.1 mM oAP, and 10 mM tBHP.

2.1d Phenoxazinone Synthase (PHS) Assay Optimization

A buffer and oxidant study was conducted to optimize the PHS assay conditions. To identify an optimal buffer system for the variants, 8 buffers were investigated at 4 different pHs. We first tested tris(hydroxymethyl) aminomethane (Tris) pH 8.5,

potassium phosphate pH 8.5, Tris pH 7.5, potassium phosphate pH 7.5, sodium acetate pH 5.1, ammonium acetate pH 5.1, 2-(*N*-morpholino)ethanesulfonic acid (MES) pH 5.1, and sodium acetate pH 4.1. All buffers were tested without a peroxide shunt (relying on O_2 from the air as the oxidant) with 25 μM NiR3His and 25 μM $CuSO_4$. Based on the results (see section 3), potassium phosphate buffer was chosen, with a further investigation required into the optimal pH. Using 50 mM potassium phosphate, rates for NiR3His and $CuSO_4$ with and without a H_2O_2 shunt were gathered at pHs 6.0, 6.35, 6.5, 6.75, 7.0, 7.5, and 8.0. See section x for results and discussion, but 50 mM potassium phosphate pH 7.5 was chosen as the assay pH.

In addition to a buffer optimization, various oxidants were investigated. The other oxidants were oxygen, ammonium persulfate (APS), ceric ammonium nitrate (CAN), meta-chloroperoxybenzoic acid (mCPBA), ferricyanide, cumyl hydroperoxide, and tert-butyl hydroperoxide (tBHP). We chose tert-butyl hydrogen peroxide as the oxidant for our peroxide shunted reactions, and oxygen as a "natural" oxidant, consistent with the native system.

2.1e Ortho-Aminophenol (oAP) Oxygen Consumption

The use of oxygen as an oxidant in the azurin variants' catalyzed oAP oxidation was investigated. To monitor oxygen consumption, a Clark style polarographic electrode with an YSI 5300a biological oxygen monitor was used with an Instech sealed cell apparatus. The cell was maintained at 23 °C by a Fisher Scientific Isotemp 3016D and stirred by a magnetic stir bar. The Clark electrode had a new plastic membrane with a solution of ½ saturated KCl placed under the membrane for each use. Oxygen consumption was monitored for the duration of the reaction with 250 μM protein, in 50

mM ammonium acetate buffer at pH 5.1, and varying amounts of oAP. A reaction was initiated by adding oAP to the cell with protein and buffer, and then immediately sealed by pressing the cover onto the cell. It was important to maintain no gaseous headspace in the sealed cell, as this provided a source of oxygen. The percent oxygen in solution was monitored with time, typically until it reached 0 % oxygen, over ~2-12 h.

2.2 WT Azurin Crystal Growth and Dehydration

Part of this project was the growth, dehydration, data collection, and solving of the wild type azurin crystal structure. The structure was needed as a control for our other crystal structures and on going projects. The current variants' structures have been crystallized under different conditions than the ones found in the literature[21] and this has been a necessary experiment to determine if some of the differences in the crystal structures were due to that mutations we made or the conditions the crystal was grown in. The results for this chapter will be discussed in chapter 3.

For crystallography experiments, wild type azurin was further purified beyond the established protocol described above.[1-3] Exactly 1.25 equivalents of $CuSO_4$ was added to an aliquot of protein and allowed to bind for 25 m. The protein was then injected into a low pressure chromatography system (Biorad, Econo Pump and Biorad Model 2110 Fraction Collector) fitted with a 1 meter long size exclusion gel column filled with Sephacryl 100-HR resin. This resin has a matrix with holes in the 1000-10,000 Da MW range that separate globular proteins. The column was operated at a flow rate of 0.5 mL/min for a period of 24.5 h, and 9.5 mL fractions were collected. In that time, the azurin eluted in 2 bands, one near 9.5 h and the other near 14 h. In order to collect the purest azurin for use in crystallography, a ratio of protein absorbance at 280 nm and the

T1 center in azurin at 625 nm was determined for each fraction. The molar absorptivities are 8440 and 5000 $cm^{-1}M^{-1}$, respectively, which produce a theoretical A_{280}/A_{625} ratio of 1.68 for pure azurin. The fractions in Table 1 demonstrate a typical result for a gel column injection of WT azurin. The azurin that eluted earlier (fractions 40 and 41) had a higher ratio A_{280}/A_{625}, and therefore slight impurities. However, the later azurin fractions 44 and 45 had the lowest ratio and were therefore the purest azurin. In the example shown, (Table 1) fractions 44 and 45 were selected as the purest azurin due to their average ratio of A_{280}/A_{625} = 1.97. In addition, the data in table xx correspond to an injection of 6 mL of 683 μM protein totaling 57 mg of azurin. We typically aim to inject 100 mg or less at a time, in a volume of 9 mL or less. The total azurin recovered in Table 1 was 42 mg, however only 17 mg of azurin was pure. This recovery of 73.7 % percent pure protein was typical.

Table 1. Example of a typical WT azurin gel column injection fraction work up.

Fraction #	A_{280} (AU)	A_{625} (AU)	Ratio	Mg Az
47	0.05	0.01	3.68	0.38
46	0.19	0.09	2.17	2.41
45	0.78	0.41	1.91	10.92
44	0.48	0.24	2.03	6.37
43	0.11	0.05	2.19	1.34
42	0.06	0.03	2.08	0.74
41	0.13	0.01	10.56	0.34
40	0.25	0.02	10.15	0.66
39	0.22	0.06	3.85	1.51
38	0.28	0.09	3.21	2.37
37	0.33	0.12	2.65	3.31
36	0.20	0.04	4.94	1.09
35	0.36	0.08	4.52	2.15
34	0.28	0.07	4.20	1.81
33	0.17	0.06	2.64	1.74
32	0.14	0.04	3.70	1.00
31	0.13	0.05	2.45	1.44
30	0.11	0.04	2.50	1.15
29	0.06	0.03	1.81	0.94
28	0.03	0.01	2.40	0.29

The pure azurin fractions were pooled and exchanged into 50 mM Tris HCl buffer at pH 7.0 using a PD-10 exchange column. After this, the concentration of the protein was determined using the T1 Cu absorbance at 625 nm. The final volume required to reach 30 mg/mL was determined. To concentrate the protein, a 10000 nominal molecular weight limit Ultracell® YM membrane Centricon centrifugal filter devices were used to achieve the desired volume. The samples were then aliquoted into 100 μL samples, flash frozen in liquid nitrogen, and stored in a -80 °C freezer for future use.

Wild type azurin crystals were grown using the hanging drop method and the gel column purified azurin aliquots. To grow a crystal for data collection, 61 WT azurin crystal boxes were made that varied: PEG polymeric chain length from 1000, 2000, 4000, and 8000; PEG concentration from 7-40 %; salt type from $CaCl_2$ or $LiNO_3$; salt concentration from 0 – 200 mM; droplet size water dilution from 0-3x dilution; and growth time from 2-7 days. A wild type azurin crystal that was suitable for data collection, named 61 D4, was grown from box #61 where the reservoir conditions varied from 30 to 120 mM $CaCl_2$, and 19 % to 24 % PEG-2000. The diffracted azurin crystal was selected from well D4 in the following reservoir conditions: 100 mM Tris HCl pH 7.0, 120 mM $CaCl_2$, 21% PEG-2000, and 5 mM $CuCl_2$. The droplet was prepared by combining 2 μL of the well solution with 2 μL of 30 mg/mL protein (Table 2). Thus making the conditions in the well D4 droplet for crystal growth; 15 mg/mL WTAz, 75 mM Tris HCl, 60 mM $CaCl_2$, 10.5% PEG-2000, and 2.5 mM $CuCl_2$. The crystal was grown in an isolated environment at room temperature for 5 days.

Once obtained, crystals were dehydrated to remove excess solvent, as this has been shown to improve crystal order and diffraction resolution. Based on fine-tuning of

techniques found in the literature[6-9], the optimal dehydration conditions for the wild type crystal were developed. To determine the correct conditions for dehydration that would not crack or deform the crystal, a protocol was developed that took into account the conditions the crystal was grown in. The chosen optimal conditions were the same conditions as the reservoir in which the crystal was grown over, except for the PEG concentration. The PEG concentration was made to be +15% PEG from the original droplet the crystal was grown in. For example, crystal 61 D4 was grown in droplet conditions that were 10.5% PEG. To dehydrate the crystal , 25.5% PEG was used (Table 3). Furthermore, to dehydrate the crystal, both the crystal box and the dehydration box were placed in the cold room at 4 °C and allowed to equilibrate for 2 h. Once chilled, the crystal was transferred to a 5 μL droplet of the dehydration solution and placed over the dehydrating well for 15 h. No glycerol was added to the dehydration solution. After dehydrating, the crystal was flash frozen in liquid nitrogen on a 0.2-0.3 mm crystal loop and stored in liquid nitrogen until it was screened.

Table 2. Box conditions used to grow crystal 61 D4 used in gathering dataset for WTAz crystal structure.

Box 61	2.0M Tris HCl pH 7.0 (µL)	M	3.0M $CaCl_2$ (µL)	%	50% PEG-2000 (µL)	0.1 M $CuCl_2$ (µL)	Millipore H_2O (µL)
A1	50	0.03	10	24	480	50	410
A2	50	0.03	10	23	460	50	430
A3	50	0.03	10	22	440	50	450
A4	50	0.03	10	21	420	50	470
A5	50	0.03	10	20	400	50	490
A6	50	0.03	10	19	380	50	510

	2.0M Tris HCl pH 7.0 (µL)	M	3.0M $CaCl_2$ (µL)	%	50% PEG-2000 (µL)	0.1 M $CuCl_2$ (µL)	Millipore H_2O (µL)
B1	50	0.06	20	24	480	50	400
B2	50	0.06	20	23	460	50	420
B3	50	0.06	20	22	440	50	440
B4	50	0.06	20	21	420	50	460
B5	50	0.06	20	20	400	50	480
B6	50	0.06	20	19	380	50	500

	2.0M Tris HCl pH 7.0 (µL)	M	3.0M $CaCl_2$ (µL)	%	50% PEG-2000 (µL)	0.1 M $CuCl_2$ (µL)	Millipore H_2O (µL)
C1	50	0.09	30	24	480	50	390
C2	50	0.09	30	23	460	50	410
C3	50	0.09	30	22	440	50	430
C4	50	0.09	30	21	420	50	450
C5	50	0.09	30	20	400	50	470
C6	50	0.09	30	19	380	50	490

	2.0M Tris HCl pH 7.0 (µL)	M	3.0M $CaCl_2$ (µL)	%	50% PEG-2000 (µL)	0.1 M $CuCl_2$ (µL)	Millipore H_2O (µL)
D1	50	0.12	40	24	480	50	380
D2	50	0.12	40	23	460	50	400
D3	50	0.12	40	22	440	50	420
D4	50	0.12	40	21	420	50	440
D5	50	0.12	40	20	400	50	460
D6	50	0.12	40	19	380	50	480

Table 3. Dehydration conditions for crystal 61 D4 used to collect a dataset for WTAz.

Well	2.0M Tris HCl pH 7.0 (µL)	M	3.0 M $CaCl_2$ (µL)	Original PEG Concentration (%)	15%+	50% PEG-2000 (µL)	0.1 M $CuCl_2$ (µL)	Millipore H_2O (µL)
D4	50	0.12	40	10.5	25.5	510	50	350

Good azurin crystals were screened for low mosaicities (<0.6 °) and high resolutions (<2.0 Å). We screened 132 crystals before finding a good one, where a full data set could then be collected. A crystal was identified with a mosaicity of 0.4335 ° and resolution of 2.0 Å by the initial screening frames. A dataset was collected for crystal 61 D4 over the span of 2 weeks. The crystal was bathed in a constant X-ray beam generated from a Cu Kα 1.5419 Å X-ray sealed tube lamp in a Rigaku Rapid-II diffractometer with an image plate detector. Each image was obtained with 20 min exposures while oscillating the crystal 0.5°. To amass a complete dataset, 782 images were taken over 2 weeks. The programs CrystalClear 2.0, CCP4, and Coot were used to solve the dataset and produce a crystal structure for WT azurin.[10-12]

2.3 Peptidylglycine α-Hydroxylating Monooxygenase (PHM) Assay Methods

To assess our proteins' activity, we assayed them using hydroxylation assays. Discussed herein is the peptidylglycine α-hydroxylating monooxygenase (PHM) oxidation assay. Hippuric acid was used as the substrate due to its resemblance to glycine, the native substrate of PHM.[13] The goal was to mimic the oxidoreductase protein PHM, and to assess this; we monitored the hydroxylation of hippuric acid and monitored the oxygen consumption during the assay. The results will be discussed in Chapter 3.

Protein was prepared in the same manner as preparation for the PHS assay described above in section 2.1.a. PHM activity was assayed according to literature[13-15]

procedures, where oxygen concentration was monitored and hydroxylated products were quantified by HPLC. The decrease in oxygen concentration was monitored using a Clark style polarographic electrode with an YSI 5300a biological oxygen monitor. Hippuric acid (HA) and α-hydroxyhippuric (AHHA) concentration were determined using HPLC with a Thermo Separation Products P200 and UV 100 detector set to 220 nm. To separate the reaction components, a Macherey-Nagel ET 250/8/4 Nucleosil 10 C^{18} column was used in combination with a Waters 4.6 x 50 mm C_8 3.5 μm guard column. The assay was performed at a protein concentration of 250 μM, 30 mM ascorbic acid, in 50 mM ammonium acetate buffer pH 5.1, in a total volume of 2.5 mL, and 1 mM hippuric acid. The reaction cuvette was stirred using a Variomag Telemodul magnetic stir device, and the Clark oxygen electrode was inserted into the top of the cuvette. Additionally, the UV-Visible absorption spectrum was monitored for the disappearance and reappearance of oxidized azurin (blue color, at 625 nm). Aliquots of the reaction mixture were taken at time intervals to monitor substrate and product concentration. The 10 μL aliquots were combined with 50 μL of 6% TFA to quench the reaction and stored in the -4 °C freezer. The aliquots of the reaction were analyzed using HPLC analysis the next day.

The HPLC separation protocol consisted of a two buffer system of 100:0 and 15:85 acetonitrile:Millipore water mixture, both containing 0.1% TFA. To initiate a separation, 10 μL of the aliquot was injected using a Hamilton syringe and the separation method was started. Based on work done by a previous student, it was determined that HA eluted at 550 s and AHHA acid eluted at 500 s (Figure 35). To monitor

concentrations of both product and reactant, standard curves were developed as shown in Figures 36 and 37.

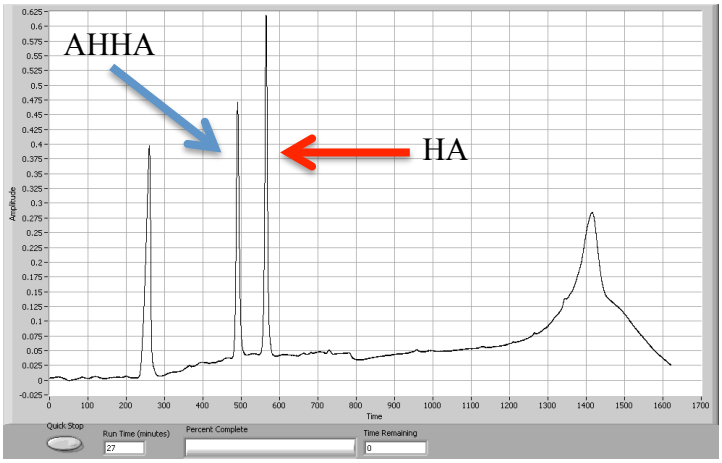

Figure 35. Control HPLC experiment to test separation ability of system. Hippuric acid elutes at 550 s, and α-hydroxyhippuric acid elutes at 500 s. Both peaks correspond to a concentration of 5 mM as determined using the area of the peak and standard curves.

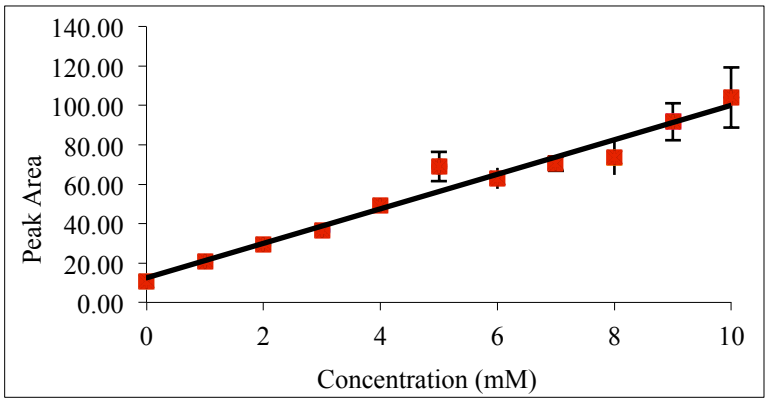

Figure 36. Standard curve developed previously for hippuric acid, eluting at 500 s, giving R^2 of 0.968, and a linear regression of y = 8.7642x + 12.476.

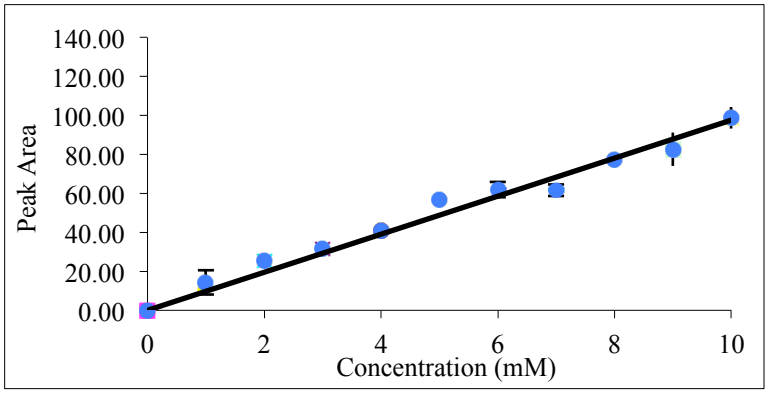

Figure 37. Standard curve developed previously for α-hydroxyhippuric, eluting at 550 s, giving R^2 of 0.9775, and a linear regression of y = 9.7646x.

Chapter 3: Results and Discussion

3.1 PHS Assay Initial Investigations

Based on previous work, all initial PHS assay experiments were performed with the NiR3His azurin variant. We observed our NiR3His variant to react with oAP and produce the chromophore APX product indicated by the increase in the characteristic 434 nm absorbance peak (Figure 38). This was a promising start to our investigation, as our parent mutants demonstrated the ability to efficiently catalyze the oxidation of PHS.

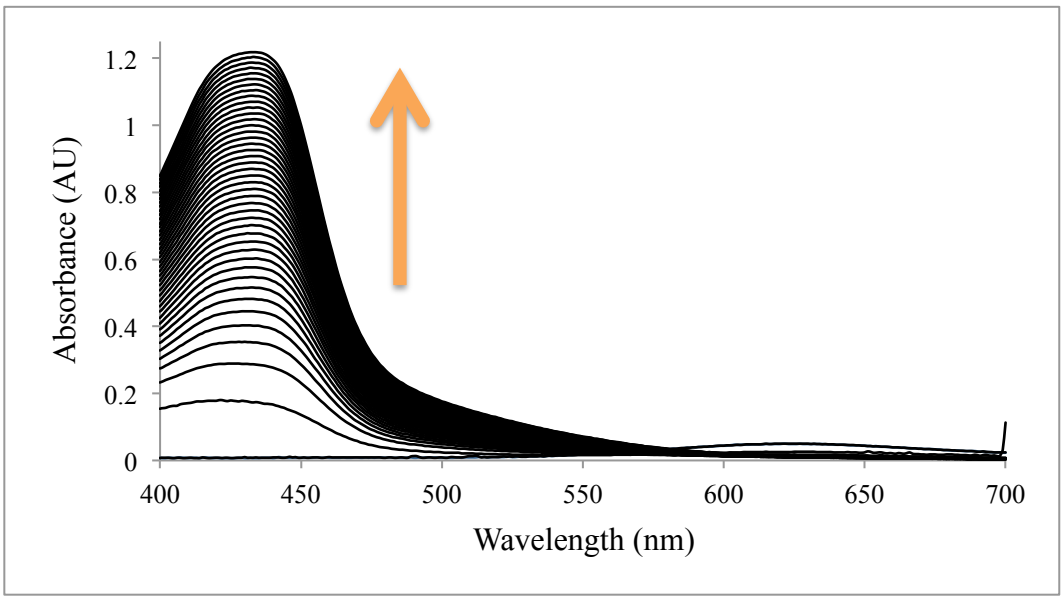

Figure 38. Example spectra of an assay with NiR3His azurin, oAP, and H_2O_2. A spectrum was taken every 30 seconds, and the intensity of the 434 nm peak grows in with each scan.

Although the majority of the PHS assay was investigated with a peroxide shunt, we also explored the oxygen consumption of the PHS system. This was important as oxygen gas is the natural substrate of the native enzyme. These assays were run with only protein and oAP with the oxygen sensor to measure oxygen consumption over time. The protein concentration used was higher than that for the peroxide shunt assays (increased from 10 μM to 250 μM). This increase in protein concentration was used because the rate of oAP oxidation was slower with oxygen as the oxidant than with

peroxides. We used ambient oxygen from air to saturate the reaction with oxidant. Therefore the maximum dissolved oxygen concentration we could achieve was ~256 µM, which was not in large excess of the enzyme concentration. Oxygen consumption was monitored in a sealed cell until all the dissolved oxygen in the reaction was depleted. Figure 39 shows the results of an oxygen assay in which 250 µM $CuSO_4$ or 250 µM NiR3His were used as catalysts along with 10 mM oAP. The NiR3His azurin catalyzed the consumption of all the dissolved oxygen in ~75 min, whereas the $CuSO_4$ control experiment consumed only a small quantity of oxygen.

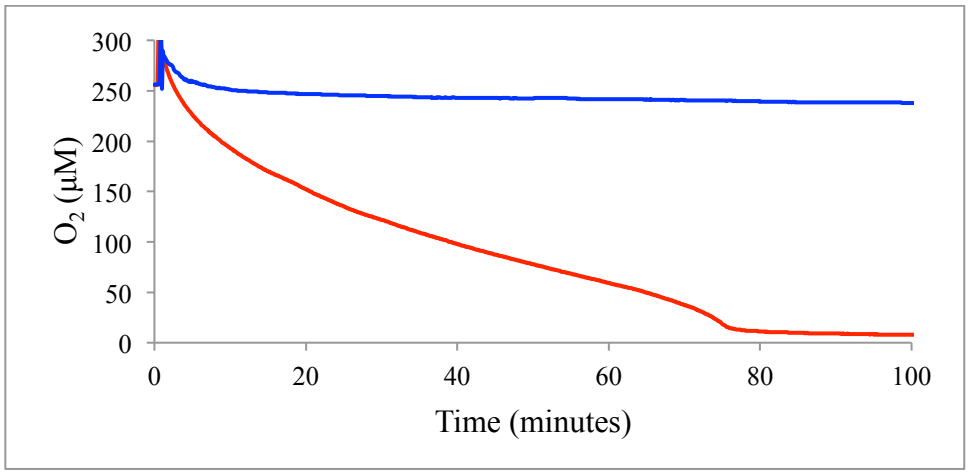

Figure 39. Results from an oxygen sensor assay, shown in blue is 250 µM $CuSO_4$ and red is 250 µM NiR3His, both with 10 mM oAP.

Figure 40 shows examples of oxygen consumption with NiR3His azurin. As the concentration of oAP increases, so does the rate at which the oxygen is consumed. The rate of oxygen consumption (slopes of the curves in Figure 40) increases linearly, from 0.5 – 25 mM oAP. In addition, oxygen consumption increased by 10 times when the oAP concentration was increased from 1 to 10 mM, and again goes up by about 2.5 times when oAP concentration is increased again from 10 to 25 mM.

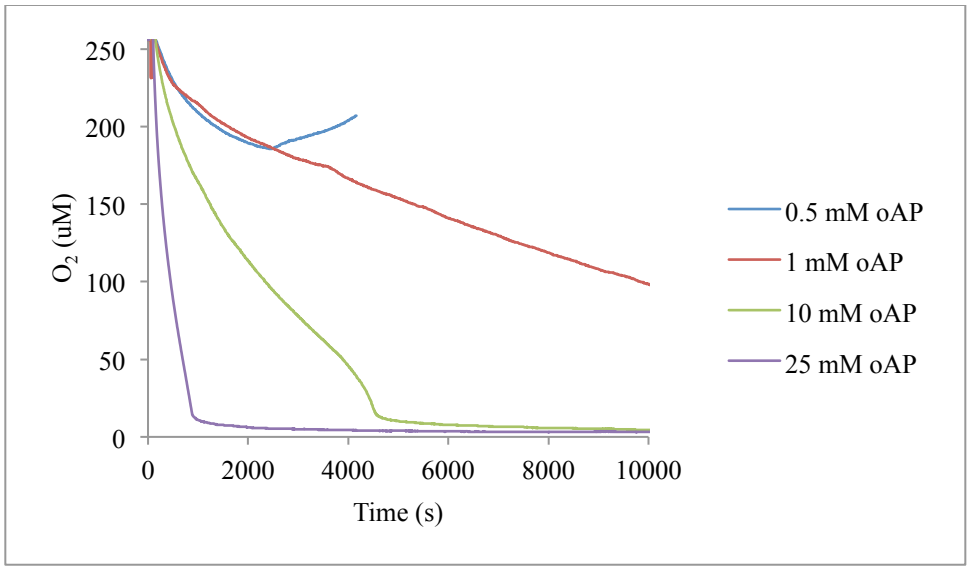

Figure 40. Oxygen sensor assays using NiR3His and varied amounts of oAP. As the oAP concentration increases, the rate at which the oxygen is consumed is also increased. The 0.5 mM oAP curves up slightly due to a slight leak allowing oxygen back into the cell slowly.

The significant result of these experiments is the fact that our system is capable of using oxygen as an oxidant. This is interesting since our models lack the T2/T3 trinuclear copper cluster believed to be necessary for oxygen reactivity in the native PHS system. The oxygen consumption reactivity of our model systems was not the focus of my research project, but it is an area for future exploration. We started our study of this system with a peroxide shunt because the oAP oxidation activity using oxygen was slower than that with peroxide. Also, to show appreciable oxygen consumption the enzyme concentration had to be increased 25 times from 10 μM to 250 μM. We were therefore able to more quickly assay our variants and complete preliminary activity comparisons. My work focused on the oxidation of oAP by our PHS mimics using the peroxide shunt.

Another example of how much faster our system is with H_2O_2 than with O_2 is shown in Figure 41. This figure shows more product accumulation with the peroxide

shunt by directly monitoring the intensity of the APX product's 434 nm peak. Without the peroxide shunt, the system takes approximately 6 times longer.

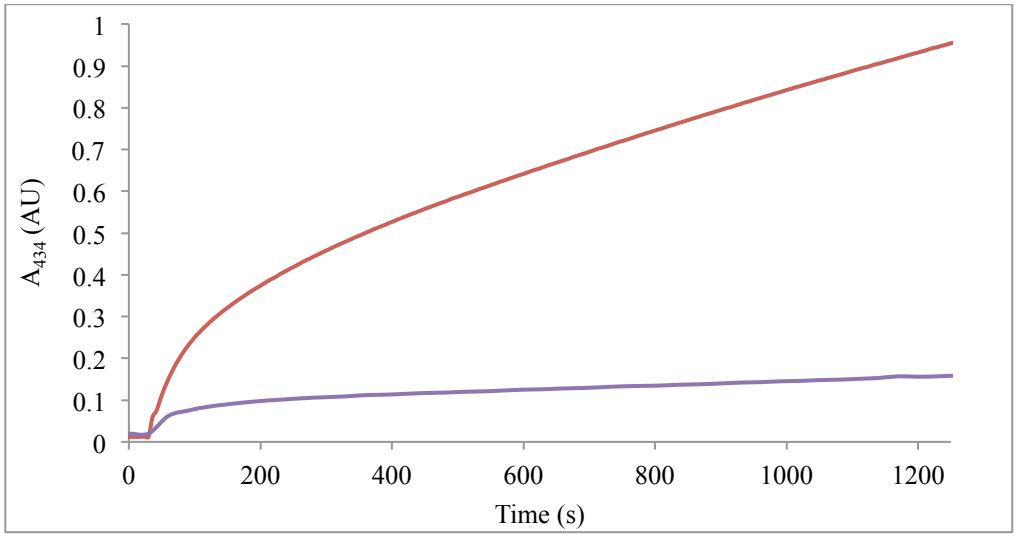

Figure 41. Plot of the A_{434} of two assays indicating the rate of oAP oxidation. The red curve has a H_2O_2 shunt and the purple curve uses O_2 as the oxidant.

At high enzyme concentrations (25 μM instead of 10 μM) we investigated an interesting reproducible observation of the assay. We observed a "biphasic" behavior to the reaction (Figure 41 and Figure 42). There was an initial "fast" phase, and then a transition to a "slow" phase. This phenomenon was observed when running the assays at enzyme concentrations higher than 10 μM. A concentration of 25 μM enzyme was used in order to observe a more intense azurin T1 625 nm peak. When azurin is in the oxidized Cu^{2+} state, it has an absorbance at 625 nm. However, when it is reduced to the Cu^{1+} state, the absorbance disappears. When we observed the entire visible spectrum, the fast phase of APX product formation was over when the entire azurin 625 nm peak was gone. Then, when all the azurin T1 copper centers were reduced, the reaction demonstrated a slow phase (Figure 42). This investigation revealed to us that the oAP reacts directly with our T1 copper center in our model. In addition, the fast phase transitions into the slower phase when APX product peak reached ~0.21 AU, which

corresponds to an APX concentration of ~9.2 µM. Since 25 µM NiR3His azurin is present with 2 Cu^{2+} ions, there is a total of 50 µM Cu^{2+} ions able to accept 1 electron. Therefore, the expected APX absorbance at 434 nm if all copper ions are reduced is 0.19 for a concentration of 8.33 µM APX, based on the conversion of oAP to APX requiring a 6 electron oxidation. In our experiment, we saw a slightly higher absorbance than expected (~0.21 vs 0.19), likely due to a hypothesized slower turnover of the system with the H_2O_2 oxidant that oxidizes some Cu^{1+} back to Cu^{2+} during the fast phase. We hypothesize the azurin is accepting all the electrons from oAP to undergo an initial fast phase reaction to reduce all coppers in azurin and once all coppers have been reduced, the slow phase is then dependent on the reoxidation of the reduced azurin with an oxidant enabling it to accept more electrons from oAP. This reoxidation of azurin occurs at a slower rate than the reaction of oAP with the oxidized enzyme. We therefore hypothesized that oxidation of the enzyme was the rate limiting step.

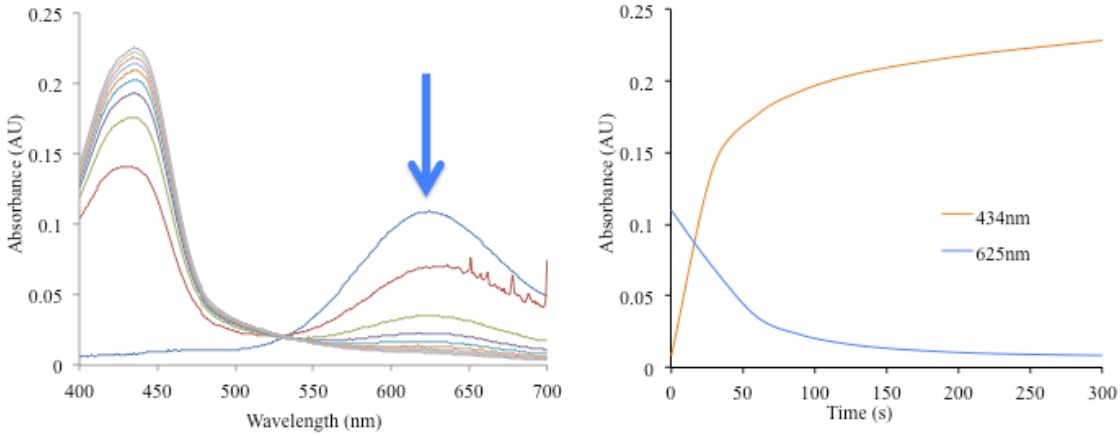

Figure 42. PHS assay with an increased enzyme concentration to investigate the biphasic behavior of the system with a hydrogen peroxide shunt. The fast phase is over when the azurin T1 site is fully reduced and then switched to a slower phase.

3.2 Preliminary H_2O_2 Shunt PHS Assay

A Michaelis Menten investigation with a H_2O_2 shunt was performed in 50 mM NH_4OAc, using 10 μM catalyst, and a 10 mM H_2O_2 shunt. The assay followed Michaelis Menten kinetics and produced a V_{max} of 2.63 x 10^{-2} mM/min, and K_m of 4.56 mM, with a turnover number of 2.63 mmol oAP min^{-1} $mmol^{-1}$ Az (Figure 43). When compared with the native PHS turnover number of 1,180 mmol oAP min^{-1} $mmol^{-1}$ PHS,[16] the assay under these conditions is about 450 times slower than the native system. This assay was performed in 50 mM ammonium acetate buffer at pH 5.1, to be consistent with the literature conditions in which PHS' activity was measured. Our next logical step was to explore the reactions behavior under varied conditions and find optimal conditions. The first way we chose to optimize our reaction was to explore different buffers and pHs.

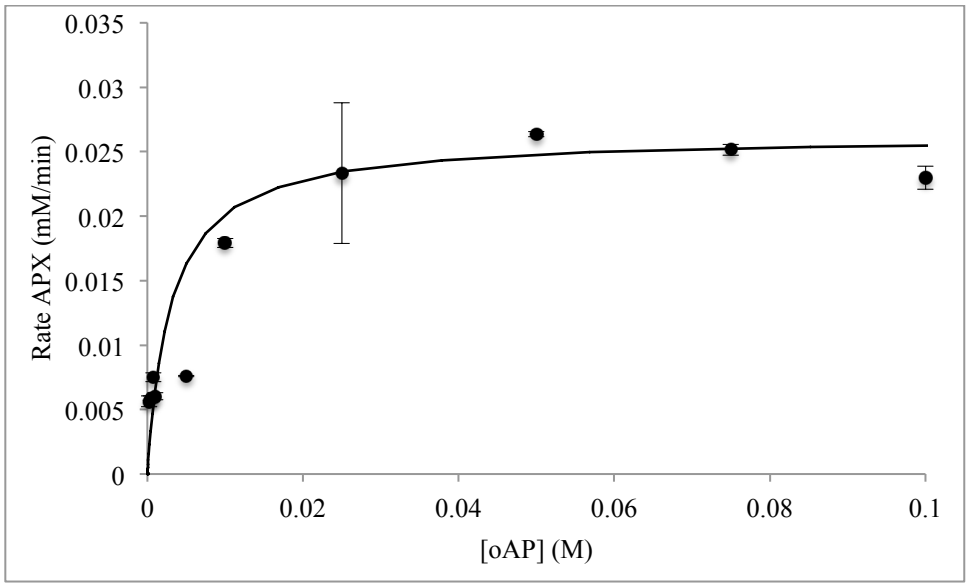

Figure 43. Preliminary Michaelis Menten kinetic fit for NiR3His model azurin using a H_2O_2 shunt. Error bars shown are the standard deviation of the initial linear rate for assays done in triplicate.

3.3 PHS Assay Improvement: Buffer & Oxidant Study

A buffer study was undertaken where pHs above and below 5.1 were investigated with and without a peroxide shunt. We initially assayed 8 different buffer systems at 4

pHs as shown in Figure 44. We chose different buffer types at the same pH to test whether the buffer compound affected activity. We also used the same buffer but at different pHs to test the pH dependence of the reaction. In addition, we compared the reaction rates using our protein catalyst to those rates with free $CuSO_4$ as catalyst. Overall wee saw the activity increase for the higher pHs. Both pH 7.5 and 8.5 demonstrated the highest activity. Furthermore, when we examined the activity of free $CuSO_4$, we saw a high rate in Tris buffer systems at pHs 7.5 and 8.5 compared to the protein catalyst (Figure 44). The phosphate buffer at pHs 7.5 and 8.5 did not show this trend. The phosphate buffer had an increased protein activity rate with a very slow background free copper rate. Because of this, phosphate buffer was chosen as the buffer, and another buffer study was performed to determine the optimum pH for the phosphate buffer.

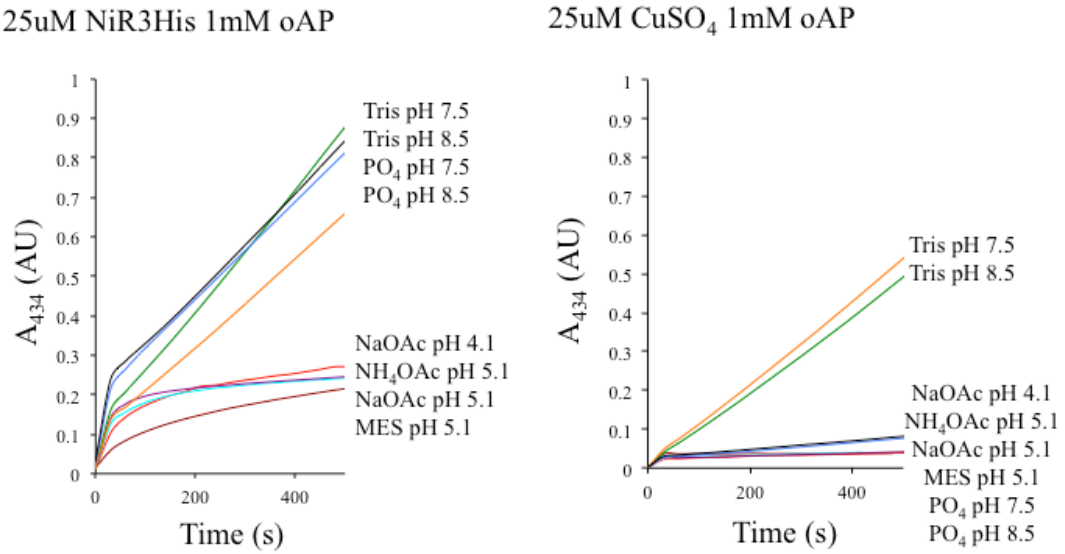

Figure 44. Initial buffer study showing the activity of NiR3His and $CuSO_4$ with varied buffers and pHs. The protein activity increased with higher pHs in both potassium PO_4 and Tris buffers while the background activity only increased with Tris. All buffers were 50 mM in concentration.

The phosphate buffer system was investigated from pH 6.0-8.0. At higher pH's the rate we observed with protein and a peroxide shunt was fast (Figure 45a). This

indicated that all pHs were fast for the phosphate buffer above pH 6.0. We removed the peroxide shunt to slow the reaction down to keep it below an absorbance of 1.0 on our spectrophotometer over a longer time period (Figure 45c). Without the shunt we observed that the more basic the buffer system became, the faster the assay became. pH 8.0 was the fastest (Figure 45c). We speculate that the higher pH is faster for our system due to the pKa the amine group of oAP. The amine group is more in the NH_2 form and more likely to interact with Cu^{2+} than the $-NH_3^+$ form. When free copper activity was examined, the trend was the opposite (Figure 45d). Without a peroxide shunt, all copper rates were very slow, and no trend in reaction rates could be deciphered confidently. However, with the peroxide shunt, we observed the control free $CuSO_4$ reaction rates to get slower as pH increased, with pHs 7.5 and 8.0 being the slowest (Figure 45b).

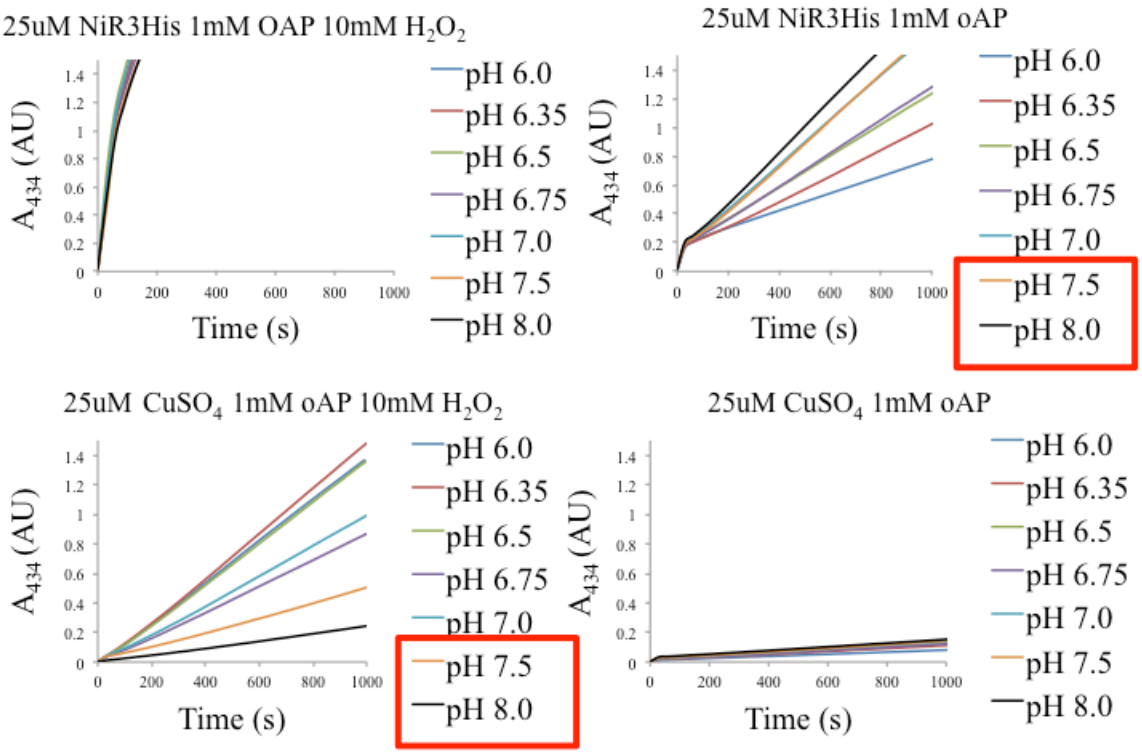

Figure 45. Results of the potassium phosphate buffer study from pH 6.0-8.0. All assays were run with the same concentration of catalyst both with and without a peroxide shunt. The red boxes showcase the results in which the enzyme activity was maximized with a minimized free copper sulfate activity. A) Top left

graph with NiR3His and a H_2O_2 shunt B) Top right NiR3His without a H_2O_2 shunt C) Bottom left $CuSO_4$ with a H_2O_2 shunt D) $CuSO_4$ without a H_2O_2 shunt. All buffers were 20 mM in concentration.

Based on the above studies, we chose a buffer system of 20 mM potassium phosphate pH 7.5. This was because phosphate was a good buffer system with high enzyme activity and low free copper activity. In addition to this, we chose a pH of 7.5 because azurin is more stable at pHs near 7 because of phosphate's ability to buffer better at pH 7.5 than 8.0, and because 7.5 is more physiologically relevant. Figure 46 shows our enzyme activity, free copper, and oAP background oxidation of oAP with a peroxide shunt in the final buffer choice. The enzyme is fastest, followed by free copper, and background oAP oxidation.

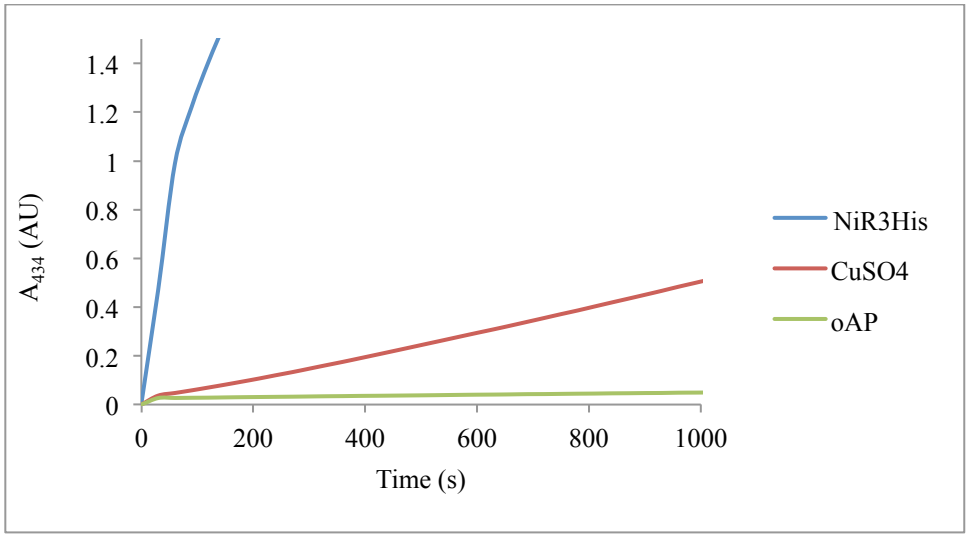

Figure 46. Plot of the 434 nm peak of assays with NiR3His, $CuSO_4$, and background oAP activity assays with a H_2O_2 shunt.

Once the pH and buffer system was chosen, the next logical place to improve the activity assay was to find a practical oxidant. As shown above, the use of a hydrogen peroxide species was faster than using O_2 as an oxidant. In addition, we investigated other oxidants listed in section 2.1d. It was discovered that the oxidants; ammonium persulfate (APS), ceric ammonium nitrate (CAN), meta-chloroperoxybenzoic acid

(mCPBA), ferricyanide, cumyl hydroperoxide had high direct uncatalyzed background oxidation rate with oAP. The best oxidant for our system was determined to be tBHP as it was faster than H_2O_2 and O_2, with a small background rate. Furthermore, tBHP is has a lower reduction potential than H_2O_2, and could therefore be less likely to participate in unwanted side reactions. Hydrogen peroxide has a reduction potential of 1.763 V[1] and tBHP's potential is 1.05 V[2]. The lower reduction potential makes it a milder oxidizing agent. To demonstrate this, we monitored the T1 center absorbance using 25 μM NIR3His in the presence of 1 mM tBHP or 1 mM H_2O_2 upon additions of 25 μM oAP (Figure 47). As can be observed in Figure 47, the addition of oAP to the tBHP reaction resulted in reduction of the T1 copper center (Absorbance at 625 nm) with its concomitant full reoxidation by tBHP. On the other hand, when H_2O_2 was used, the oxidized T1 Cu center never recovered its T1 copper center absorbance after just one addition of oAP, indicating loss of the catalyst by H_2O_2. Furthermore, with tBHP, the copper center recovers completely to 100% after multiple additions of oAP, demonstrating its resiliency. This experiment indicated that H_2O_2 destroys our T1 copper center, presumably decreasing the enzyme activity over time. tBHP did not significantly hurt the T1 copper center, and was able to withstand more than 1 addition of oAP.

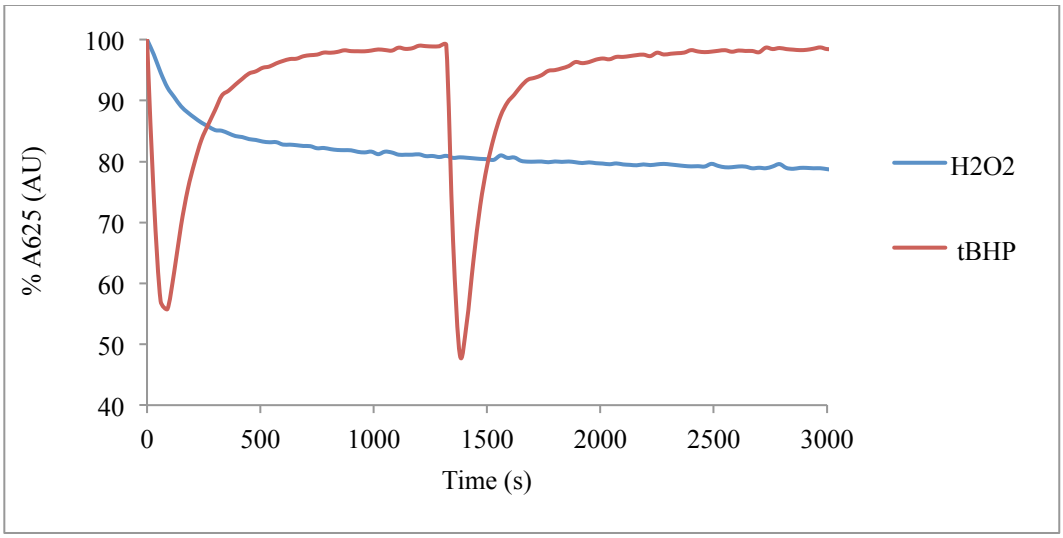

Figure 47. Percent absorbance of the T1 Cu center absorbance in 25 µM NiR3His in the presence of 1 mM tBHP or H_2O_2 indicating recovery of the T1 center from its bleached form. Each drop in absorbance represents the addition of one 25 µM oAP to the reaction.

When control assays rates were compared using tBHP as the oxidant, we also observed a significant increase in activity. Figure 47 shows the increased rate of tBHP when compared to H_2O_2, free copper as a catalyst, and background oAP oxidation.

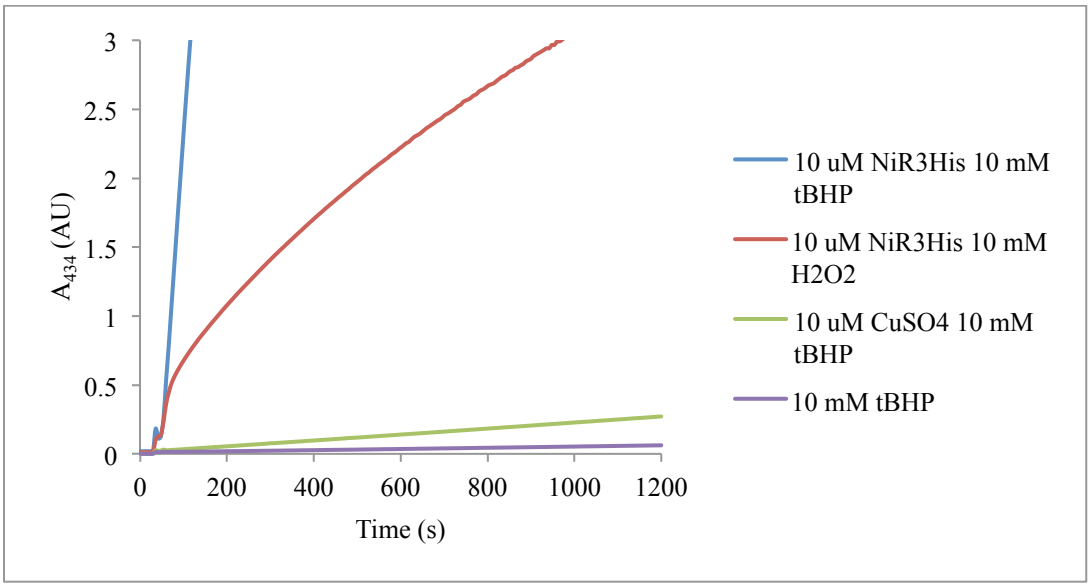

Figure 48. Reactions and controls using the final 20 mM phosphate buffer at pH 7.5 and tBHP shunt conditions.

In conclusion, we optimized the buffer to 20 mM potassium phosphate pH 7.5 and found the milder tBHP peroxide shunt species (Figure 48). In addition to optimizing the conditions for increased activity, the PHS assays no longer displayed the "biphasic" behavior described in Section 3.1. This is due to a decrease in enzyme concentration from 25 μM to 1 μM to compensate for the increased optimized enzymatic activity (see below). This decrease reduced the impact of the "fast" phase by decreasing the amount of electrons that can be transferred to azurin initially. Now that the conditions were optimized, we revisited the Michaelis Menten kinetics for NiR3His and all the parent variants.

3.4 NiR3His-Azurin tBHP Shunt Assay

The first assay to be revisited was the NiR3His assay, now with the 20 mM potassium phosphate buffer at pH 7.5 and the 10 mM tBHP shunt. However, when the assay was attempted under the similar conditions to the H_2O_2 shunt assay, the reaction was too fast to record accurately. To compensate for this, we decreased the enzyme concentration from 10 μM to 1 μM. Once this change was made the assay was performed and the Michaelis Menten plot of NIR3His with a tBHP shunt is shown in Figure 49.

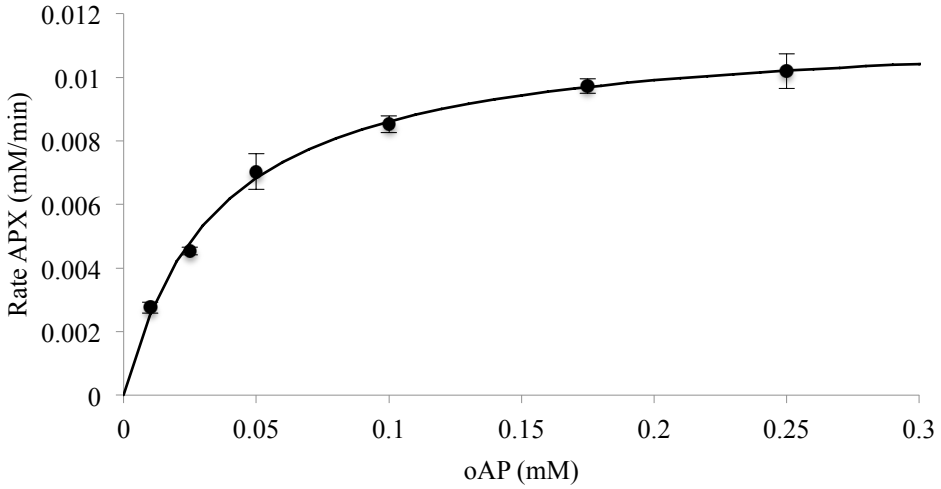

Figure 49. Michaelis Menten plot for the PHS tBHP assay using NiR3His. The new optimized tBHP conditions are a 20 mM potassium phosphate buffer, a 10 mM tBHP shunt, and a decreased enzyme concentration of 1 μM. Error bars shown are the standard deviation of the initial linear rate for assays done in triplicate.

The new NiR3His PHS assay showed improvements over the old conditions. First, the K_m dropped from 4.56 mM to 35.4 μM. This is a decrease in the K_m by a factor of ~130, indicating a stronger oAP binding to our protein under these buffer and assay conditions. The second improvement was the increase in turnover number. The same NiR3His variant with the H_2O_2 shunt had a turnover number of 2.63 mmol oAP min^{-1} $mmol^{-1}$ Az, but, with the tBHP shunt NiR3His produced a turnover number of 11.8 mmol oAP min^{-1} $mmol^{-1}$ Az. This was an improvement of about 4 times over the H_2O_2 shunt. The assay for these conditions is about 100 times slower than the native PHS,[16] assayed in sodium acetate buffer at pH 5.0 using molecular oxygen as an oxidant. The third improvement was the error bars and shape of the curve. There was much less error in these optimized conditions and a much better fit producing the Michaelis Menten curve.

3.5 Control Experiments to Investigate the Assay Mechanism

A series of controls were run to investigate our PHS model system. We ran control assays on wild type azurin, NiR3His-azurin with T1 copper center loading only, NiR3His-azurin with T1 Hg T2 Cu, wild type azurin + 1 equivalent of free $CuSO_4$, and $CuSO_4$ alone, all at 1 μM catalyst concentration.

The first interesting result came from examining the rate of wild type azurin. Wild type azurin only contains one T1 copper center, and does not have an additional copper-binding site. Figure 50 shows the rate of wild type azurin as ~60 times slower (Table 4) than the NiR3His variant loaded with 2 copper atoms per protein. This was our first indication of the significance of our T2 copper center in our model to mimic PHS' reactivity.

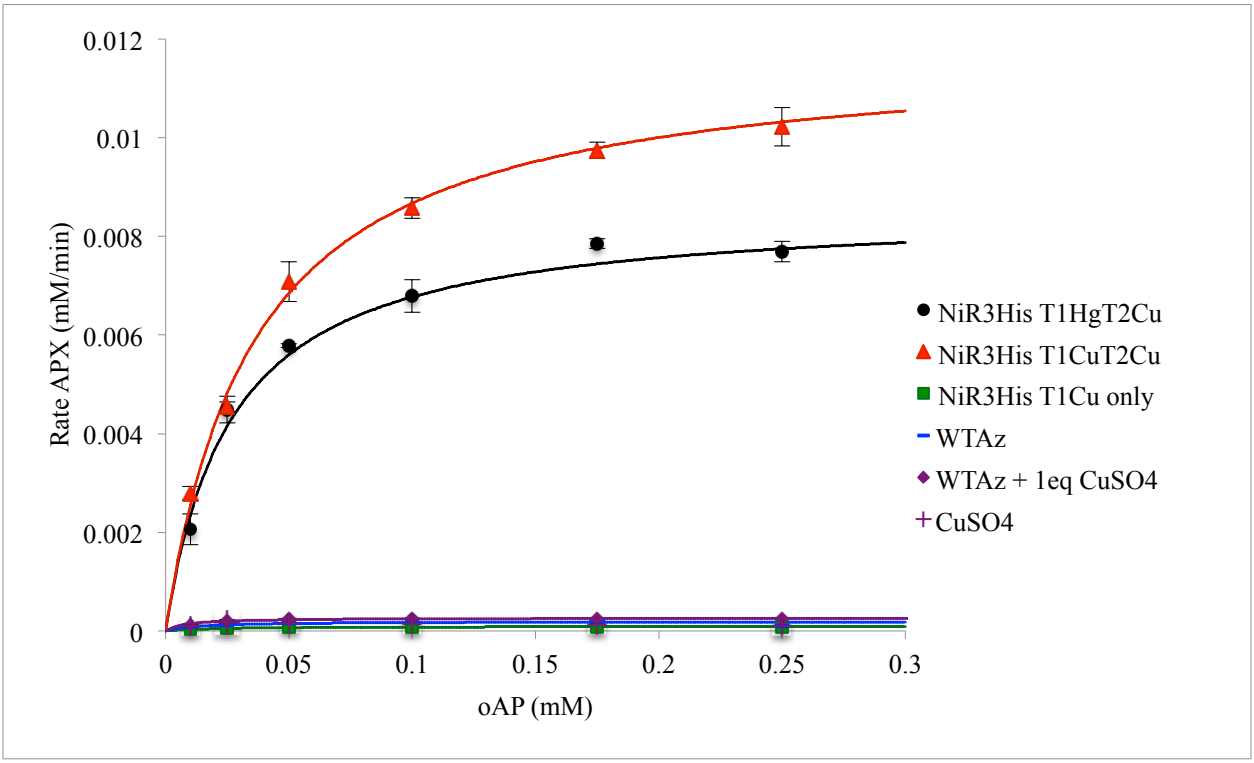

Figure 50. Michaelis Menten plots for control assays using NiR3His-azurin with varied metal loading into the copper centers, wild type, and free $CuSO_4$, Error bars shown are the standard deviation of the initial linear rate for assays done in triplicate.

Table 4. Michaelis Menten kinetic values for control assays using NiR3His-azurin with varied metal loading into the copper centers, wild type, and free $CuSO_4$. Errors were determined in Sigmaplot using a least squares analysis at the 95% confidence interval.

Protein	Vmax (mM/min)	Error (mM/min)	Km (mM)	Error (mM)	Turnover # (mmol oAP/min mmol protein)
NiR3His T1Hg T2 Cu	0.0088	0.00022	0.027	0.0026	8.8
NiR3His T1 Cu T2 Cu	0.0118	0.00028	0.035	0.0030	11.8
NiR3His T1 Cu only	0.0001	0.000002	0.021	0.0017	0.1
WTAz	0.0002	0.00001	0.014	0.0035	0.2
WTAz + 1 eq. $CuSO_4$	0.0003	0.00001	0.008	0.0015	0.3
$CuSO_4$	0.0002	0.00001	N/A		0.2

When we loaded NiR3His with a T1 copper center only, instead of 2 coppers like that of a regular assay for our models, we observed an activity that was, within error, the same as wild type azurin (Figure 50, Table 4). This is a significant observation, as when our models are loaded with just a T1 Cu center, they should behave similarly to wild type due to the lack of second copper atom at our surface T2 site. Even with the mutations to bind a second copper atom, there is not a second copper bound, like that of wild type azurin, to participate in the enzymatic cycle. The activity of the T1 only sample shows this by being ~ 60 times slower (Table 4) than the T1 and T2 copper bound NiR3His-azurin sample.

In addition to this, wild type azurin with an extra equivalent of free $CuSO_4$ has an activity only slightly higher than just wild type azurin and can be attributed to free copper activity. This is another important observation as without a surface copper-binding site, the only PHS activity will be from wild type azurin and free $CuSO_4$. Without the surface copper bound of our variants, the activity ~ 30 times less (Table 4) and supports an interaction between both copper sites during a catalytic cycle in addition to the T2 copper site's importance.

When NiR3His loaded with T1 Hg and T2 Cu was assayed, the activity was ~ 75 % (Figure 50, Table 4) of a T1 T2 copper experiment. This experiment was to probe the activity of just the T2 copper site, by blocking the T1 center with a non redox-active metal. The Hg^{2+} binds to the T1 center with a higher affinity than Cu^{2+} and is not redox active and therefore can't participate in electron transfer reaction. This variant had only the T2 copper center and therefore all activity was a result of this copper center. This result demonstrates that the T2 copper center is the key to the model's activity. Our hypothesis is that the T2 site is where the oxidant could be reacting and we hypothesized above that this could be the slower rate determining step if the reaction with oAP is very fast. This would make the copper re-oxidation the most important step so the enzyme can continue accepting electrons from oAP. This underscores the importance of our T2 surface copper center in our systems ability to mimic the reactivity of PHS.

Lastly, free $CuSO_4$ was assayed to ensure the observed activity wasn't from copper that had come out of the copper binding sites. Free copper was found to be as slow as our NiR3His-azurin T1 copper center only, wild type, and wild type + 1 eq $CuSO_4$ assays (Figure 50). When compared to the NiR3His T1 and T2 copper bound assay, it was ~ 60 times slower (Table 4) and the free $CuSO_4$ assay did not follow Michaelis Menten kinetics. Because of this, K_m was not able to be gathered (Table 4). This indicated that the activity seen in our assays is not a result of free copper in solution.

The results of the metal loading and wild type assay experiments indicate (Figure 50) the T2 copper center is very important for PHS activity. In addition, the presence of both T1 and T2 copper centers are required for optimal activity as indicated by its largest V_{max} and turnover numbers (Table 4). The control assays also shed some

mechanistic light on our system and further support the importance of a T2 copper center in our system.

Because of the metal loading controls and the importance of the T2 copper center in the T1 Hg T2 Cu sample we decided to further investigate the mechanism of our system using an EPR experiment. We attempted activity related EPR experiments to investigate the copper centers during the PHS reaction. When we combined our 1 mM NiR3His variant with 50 molar equivalents to protein of oAP, and flash froze the sample in liquid nitrogen after approximately 2 minutes of reaction, we observed 2 effects (Figure 51).

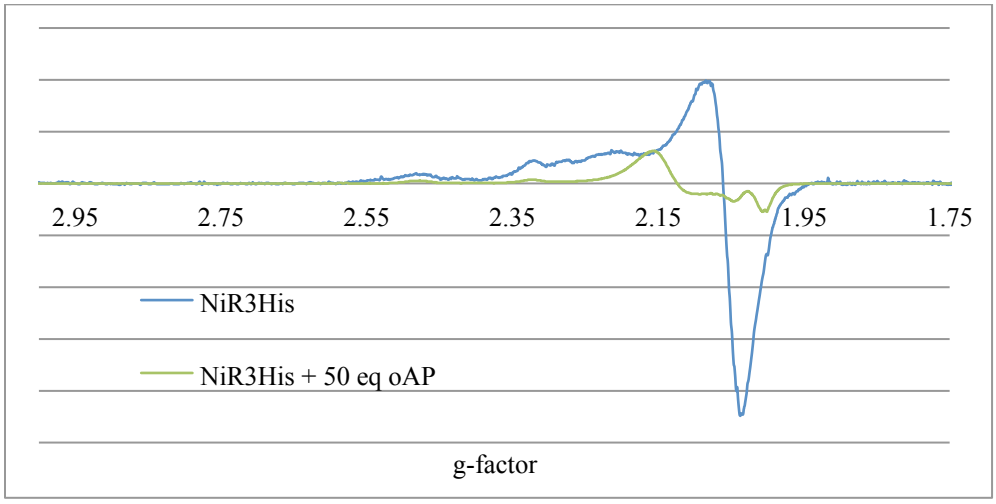

Figure 51. EPR spectra of NiR3His in 20 mM phosphate buffer at pH 7.5. Shown in blue is the EPR spectrum of just NiR3His and green is NIR3His + 50 equivalents of oAP flash frozen 2 min after addition of oAP. The green line is the shape of a T2 copper signal and there is an additional peak at a g-value of 2.03 that suggests the presence of an organic radical species and not a.

Our protein samples when loaded with both T1 and T2 copper display a signal that is a mixture of T1 and T2 copper shapes. Both of these signals overlap causing a blurring of both the spectra for our proteins, but one can make both the T1 and T2 EPR spectra with all 8 hyperfine peaks, 4 coming from each copper center (Figure 51).

The first observation from the EPR experiment with oAP added was the disappearance of the T1 copper signal and the retention of the T2 copper center (Figure 51). The green line in Figure 51 is indicative of the T2 copper center only as there are now 4 clearly defined hyperfine peaks with A-value hyperfine splitting distances of a T2 copper center. The disappearance of the T1 copper center's EPR signal is not surprising as during all PHS mimic reactions we observed the disappearance of the blue color from the T1 center, which means the Cu in the T1 was reduced from Cu^{2+} to Cu^{1+}. (The $3d^{10}$ electron configuration of Cu^{1+} is not EPR active like the $3d^9$ Cu^{2+} species is.) The disappearance of the T1 copper center EPR signal before the T2 copper center indicates the electron transfer to the T1 center is thermodynamically and/or possibly kinetically favorable and presumably first in the order of reactions in the system. This is consistent with the reduction potentials of the T1 and T2 centers. The T1 copper center has a reduction potential of about 350 mV and the T2 center is about 200-250 mV. Because of this, it is more thermodynamically favorable for the T1 site to be in the reduced Cu^{1+} state than the T2 site with the lower reduction potential.

The second observation was the presence of an additional peak in the EPR spectrum at a g-factor of about 2.03 (Figure 51). The location of this peak is characteristic of an organic radical species.[3] It could be either an oAP radical species, or a tryptophan radical.[4,5] To discern which radical species it is, we attempted to count the number of hyperfine coupling peaks on the peak. We weren't able to confidently identify any hyperfine peaks, which would allow us to indicate which radical species it was. Therefore, this peak can only be identified as an organic radical species. Alternatively,

one could interpret the EPR spectrum as that of a rhombically distorted Cu^{2+} center. We don't favor this explanation as the overall line shape

In conclusion, our working hypothesis is that once an electron has been transferred to the T1 center from oAP, it is transferred to the T2 center, where it reduces tBHP to t-butanol and H_2O (Figure 51). The T1 center is then able to accept more electrons from oAP until 2 molecules of oAP have donated 6 electrons total and reacted with one another to form the APX product. This is consistent with hypotheses on the native system in which the electrons enter the active site at the T1 center and are transferred to the T2/T3 trinuclear cluster. Once at the trinuclear cluster, the electrons reduce 3/2 molecules of O_2 to water. A depiction of this flow of electrons is shown in Figure 52 along with the native PHS' electron flow.

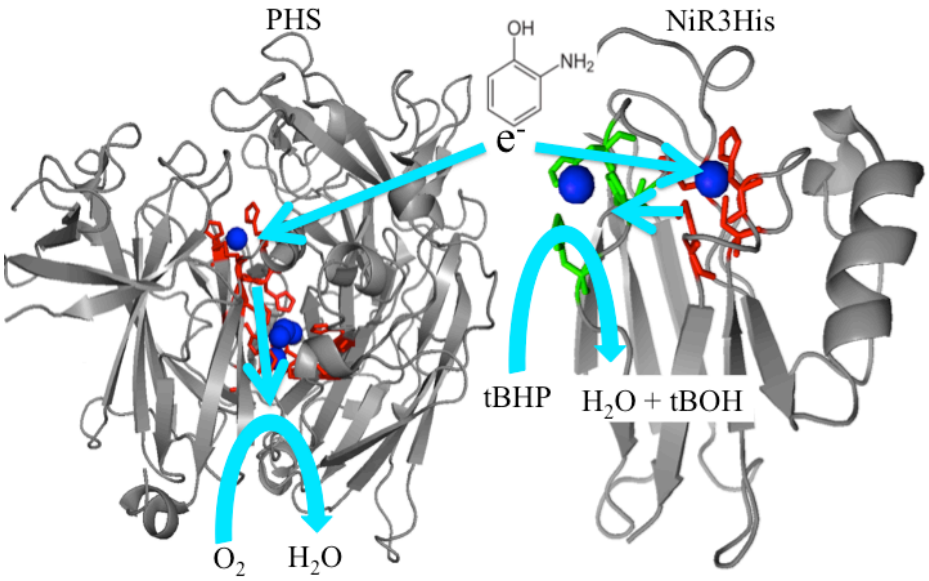

Figure 52. Hypothetical model of our NiR3His model and the native PHS' electron pathways. The blue arrows illustrate the flow of electrons through both the native PHS and our NiR3His azurin systems.

3.6 Parent Mutant tBHP Assays

After optimizing conditions and studying Nir3His azurin's PHS activity, we assayed the other parent mutants for their activity. The fastest parent variant was

NiR3His, followed by PHM, PHM3His, and NiR (Figure 53, Table 5). Like that of NiR3His, all the assays follow Michaelis-Menten kinetics. Table 5 has V_{max}, $K_{m,}$ and turnover number listed for all the variants. The V_{max} and turnover number of NiR3His are ~ 2.5 times higher than that of both PHM and PHM3His, and ~6 times higher than that of NiR (Figure 53, Table 5). PHM3His has the same rate as PHM, indicating the copper site ligands did not affect the rate much with their similar T2 center geometry. But both of the 3His models are faster than the NiR model. This isn't surprising as histidine is known to bind copper with higher affinity than aspartate and suggests a tighter T2 copper center binding with the 3His variants. Because NiR is the slowest, and that is the only T2 variant to contain a negatively charged acidic amino acid, we believe negative charge near the T2 copper center slows down the reaction due to possible electron repulsion forces between aspartate and the oxidant. This could also suggest that aspartate for NiR is weakly bound to the surface copper.

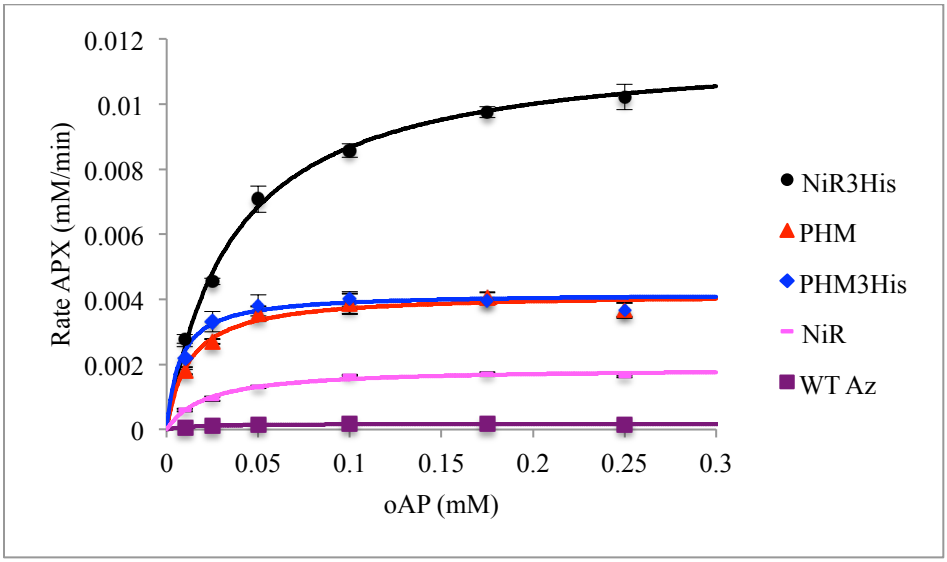

Figure 53. Michaelis Menten kinetic plots of NiR3His, PHM, PHM3His, NiR, and WT Az for the PHS assay using a tBHP shunt. Error bars shown are the standard deviation of the initial linear rate for assays done in triplicate.

Table 5. Michaelis Menten kinetic values for the parent T2 copper center variants. Errors were determined in Sigmaplot using a least squares analysis at the 95% confidence interval.

Protein	V_{max} (mM/min)	Error (mM/min)	K_m (mM)	Error (mM)	Turnover # (mmol oAP/min mmol protein)
NiR3His	0.01180	0.00028	0.03535	0.00297	11.8
PHM	0.00418	0.00012	0.01227	0.00173	4.18
PHM3His	0.00419	0.00011	0.00726	0.00127	4.19
NiR	0.00189	0.00004	0.02196	0.00210	1.89
WT	0.00018	0.00001	0.01352	0.00352	0.16
PHS[16]					1181

In addition to V_{max} and turnover number, the K_m was different for all 4 variants. The lowest K_m was PHM3His, followed by PHM, NiR, and NiR3His. Based on our working hypothesis (Figure 52), where we believe the first step of this reaction is the electron transfer from oAP to the T1 copper center in our variants, and the fact our T1 copper center is maintained all throughout the parent variations, the K_m should stay relatively the same. However, because there is variability between all the parent mutants in the design of their T2 centers, then the variations in their K_m values and the ability of the T2 to react with oxidant could be affected. There could also be a change in the electron transfer from the T1 to the T2 copper center and change how the oAP behaves at the T1 copper center.

3.7 2nd Generation Mutant PHS Assays With tBHP Shunt

The second-generation variants were assayed for all parent T2 copper center variants. The proteins assayed were all the combinations of Phe114Pro, Phe15Trp, and Met121Gln as described in Section 1.5. The Michaelis-Menten plots are show in Figures 54-57 and the V_{max}, K_m, and turnover numbers are listed in Tables 6-9.

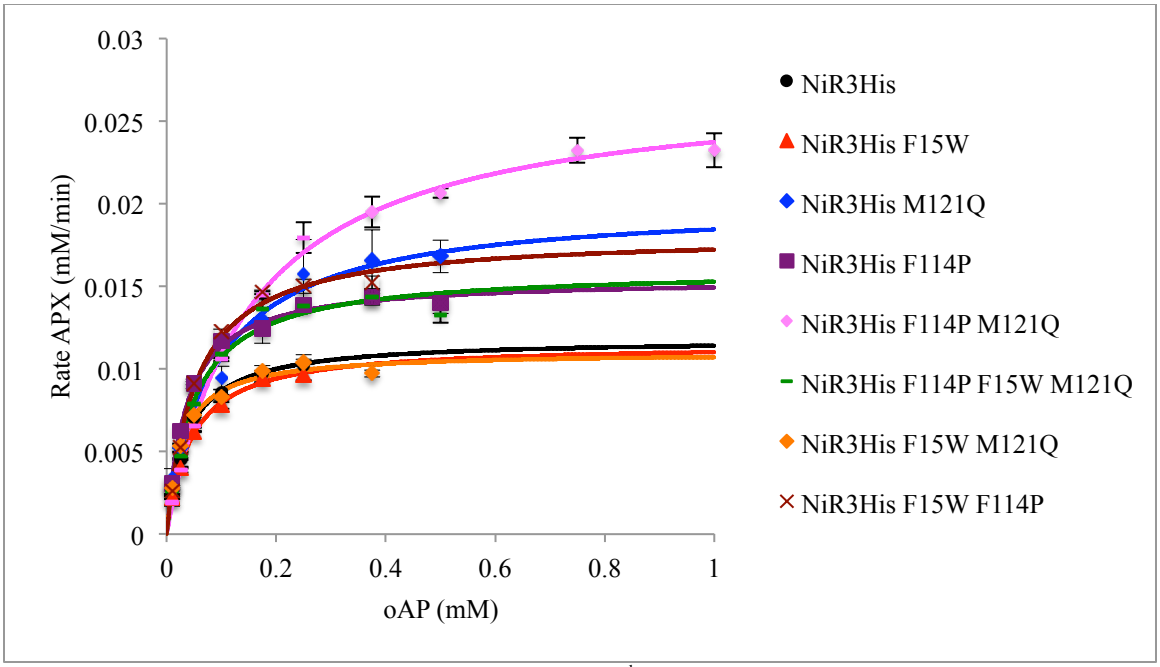

Figure 54. Michaelis-Menten plots for all NiR3His 2nd generation variants. Error bars shown are the standard deviation of the initial linear rate for assays done in triplicate. Error bars shown are the standard deviation of the initial linear rate for assays done in triplicate.

Table 6. Michaelis-Menten kinetics for all NiR3His 2nd generation variants. Errors were determined in Sigmaplot using a least squares analysis at the 95% confidence interval.

Protein	V_{max} (mM/min)	Error (mM/min)	K_m (mM)	Error (mM)	Turnover # (mmol oAP / min mmol protein)
NIR3His	0.0118	0.0003	0.0354	0.0030	11.8
NiR3His F114P	0.0155	0.0002	0.0361	0.0018	15.5
NiR3His M121Q	0.0201	0.0010	0.0870	0.0132	20.1
NiR3His F15W	0.0115	0.0002	0.0445	0.0023	11.5
NiR3His F114P M121Q	0.0273	0.0004	0.1501	0.0075	27.3
NiR3His F114P F15W	0.0181	0.0004	0.0519	0.0036	18.1
NiR3His M121Q F15W	0.0110	0.0002	0.0274	0.0021	11.0
NiR3His F114P M121Q F15W	0.0160	0.0004	0.0494	0.0049	16.0

Within the NiR3His series, the most active mutant based on the turnover number was the Phe114Pro/Met121Gln NiR3His azurin double variant. This variant has the most decreased reduction potential of about 150 mV (Figure 54, Table 6). The order of activity based on turnover number and V_{max} within the NiR3His azurin series is listed in Table 10 and is as follows: Phe114Pro/Met121Gln NiR3His azurin, Met121Gln NiR3His azurin, Phe114Pro/Phe15Trp NiR3His azurin, Phe114Pro/Met121Gln/Phe15Trp NiR3His

azurin, Phe114Pro NiR3His azurin, NiR3His azurin, Phe15Trp NiR3His azurin, and Met121Gln/Phe15Trp NiR3His azurin (Figure 54, Table 10). All of the turnover numbers have increased from the parent mutation except for the Phe15Trp NiR3His azurin and the Met121Gln/Phe15Trp NiR3His azurin, however both of those variants are within error from each other and the parent NiR3His protein. The turnover number of the variants that contained Phe15Trp and Met121Gln for the NiR3His azurin protein were all less than their corresponding single mutation. For example, Met121Gln NiR3His azurin is about two times faster than when the mutation Phe15Trp is added to make Met121Gln/Phe15Trp NiR3His azurin. The turnover number of the fastest variant, Phe114Pro/Met121Gln NiR3His azurin, has an increased value of 27.3 mmol oAP/ min mmol protein, and is now about 40 times slower than the native PHS enzyme.[16]

Within the NiR3His azurin series, there were a few interesting trends that emerged with regards to the second-generation variations. The first trend was the decrease in the reduction potential of the T1 center caused an increase in turnover number and V_{max} by as much as three times. For every 100 mV the reduction potential was decreased, the turnover number increased linearly by 8 mmol oAP min^{-1} $mmol^{-1}$ azurin, from 11.8 (NiR3His azurin) to 20.1 (Met121Gln NiR3His azurin) to 27.3 mmol oAP min^{-1} $mmol^{-1}$ azurin (Phe114Pro/Met121Gln NiR3His azurin). The highest turnover number within the NiR3His azurin (Phe114Pro/Met121Gln NiR3His azurin) series had a decreased the T1 copper center reduction potential by about 200 mV to 150 mV. Since the reduction potential of the T2 center is still about 250 mV, the T1 site has a lower reduction potential than the T2 center in these variants. It is possible that this system with the NiR3His azurin series, has a faster electron transfer step potentially due to

Marcus theory affecting the energy required for electron transfer from the T1 to the T2 site and is able to accept more electrons from oAP and thus turnover more oAP molecules.

The second trend of the second-generation variants was when Phe15Trp was combined with Met121Gln in the NiR3His azurin series; the V_{max} and turnover numbers decrease. This was shown with Phe15Trp NiR3His azurin and Phe15Trp/Met121Gln NiR3His azurin being slightly slower than NiR3His azurin. This was again shown with the Met121Gln NiR3His azurin single mutant being two times faster than the Met121Gln/Phe15Trp NiR3His azurin. And, lastly, this was shown with the Phe114Pro/Met121Gln NiR3His azurin variant being two times faster than the Phe114Pro/Met121Gln/Phe15Trp NiR3His azurin. This suggests that the Phe15Trp and Met121Gln mutations together in NiR3His azurin are detrimental. This is counter to the Phe15Trp mutation combined with the Phe114Pro mutation where the Phe15Trp increases the turnover number by about 1.3 times. This latter trend was the hypothesized one, as the Phe15Trp is designed to act as the electron transfer wire. The difference in effect for the Phe114Pro and Met121Gln's interactions with Phe15Trp could come from the relative proximity of the mutations. The Phe15Trp is closer to the theoretical location of the Met121Gln site, which could cause an interaction to slow the rate of electron transfer with the NiR3His parent variation.

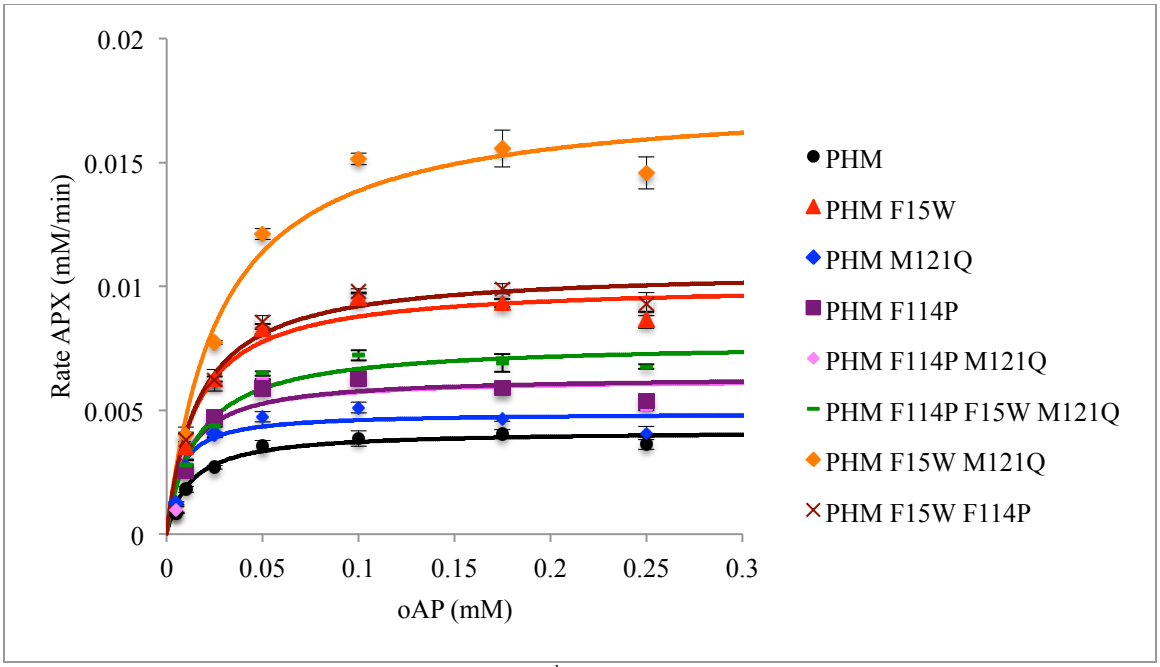

Figure 55. Michaelis Menten plots for all PHM 2nd generation variants. Error bars shown are the standard deviation of the initial linear rate for assays done in triplicate.

Table 7. Michaelis Menten kinetics for all PHM 2nd generation variants. Errors were determined in Sigmaplot using a least squares analysis at the 95% confidence interval.

Protein	V_{max} (mM/min)	Error (mM/min)	K_m (mM)	Error (mM)	Turnover # (mmol oAP / min mmol protein)
PHM	0.0042	0.0001	0.0123	0.0017	4.18
PHM F114P	0.0064	0.0002	0.0105	0.0021	6.37
PHM M121Q	0.0049	0.0002	0.0063	0.0016	4.89
PHM F15W	0.0101	0.0003	0.0151	0.0021	10.1
PHM F114P M121Q	0.0063	0.0002	0.0098	0.0026	6.30
PHM F114P F15W	0.0107	0.0003	0.0163	0.0019	10.7
PHM M121Q F15W	0.0177	0.0006	0.0277	0.0037	17.7
PHM F114P M121Q F15W	0.0077	0.0003	0.0159	0.0024	7.73

The PHM azurin 2nd generation variants produced some similar and some different trends than the NiR3His azurin series. The fastest variant in the PHM azurin series was the Phe15Trp/Met121Gln PHM azurin variant with the electron transfer wire and one mutation to decrease the reduction potential of the T1 copper center to about 250 mV (Figure 55, Table 7). This is different than the NiR3His series having Phe114Pro/Met121Gln NiR3His azurin as the fastest variant with a reduction potential of

about 150 mV. The order of decreasing rates for the PHM azurin series is listed in Table 10 and is as follows: Met121Gln/Phe15Trp PHM azurin, Phe114Pro/Phe15Trp PHM azurin, Phe15Trp PHM azurin, Phe114Pro/Met121Gln/Phe15Trp PHM azurin, Phe114Pro PHM azurin, Phe114Pro/Met121Gln PHM azurin, Met121Gln PHM azurin, and PHM azurin. The turnover numbers and V_{max} of all the 2nd generation variants for the PHM azurin series have increased from the parent PHM azurin variant by as much as 4.3 times and as little as 1.5 times (Table 7).

The first trend in the PHM azurin series is an increase in activity with the decreasing reduction potential, like that of the NiR3His azurin series. Although a similar trend emerged with decreasing the reduction potential caused an increased turnover number, the PHM azurin series increased turnover number by about 2.5 mmol oAP min^{-1} mmol^{-1} azurin per 100 mV decrease in reduction potential of the T1 copper center. Therefore, both of the singly decreased reduction potential Phe114Pro and Met121Gln single PHM azurin variants, and the doubly reduced Phe114Pro/Met121Gln PHM azurin variant increased the turnover number from the parent PHM variant by about 1 and 1.5 times over the parent PHM azurin variant. When these variants are combined with the Phe15Trp mutation, these turnover numbers increase again by an additional two times (Figure 55, Table 4).

The second trend in reactivity in the PHM azurin series as alluded to above, was the Phe15Trp interaction within the PHM azurin series, increased activity. This is shown with the fastest variant in the PHM series being the Phe15Trp/Met121Gln PHM azurin variant and the fastest 2nd generation variants all containing the Phe15Trp variation in some form. The increased rates of all Phe15Trp variants suggest the methionine of the

PHM azurin surface T2 copper center and the Phe15Trp mutations do not interact in a negative way like in NiR3His azurin. This trend is consistent with our hypothesized function of Phe15Trp acting like an electron transfer wire in the PHM azurin series.

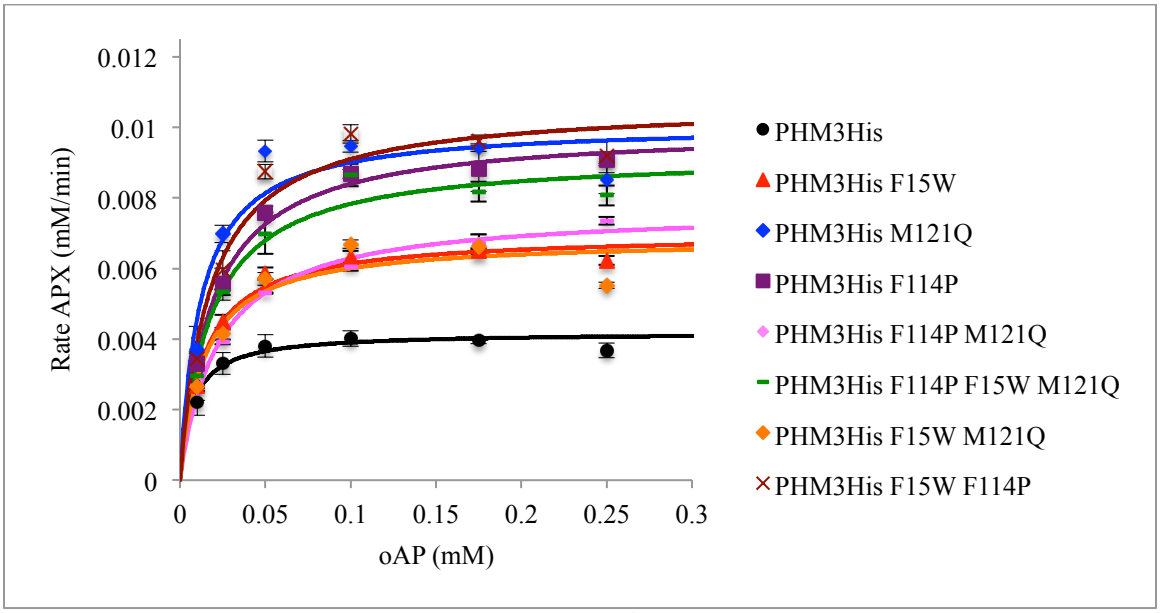

Figure 56. Michaelis Menten plots for all PHM3His 2nd generation variants. Error bars shown are the standard deviation of the initial linear rate for assays done in triplicate.

Table 8. Michaelis Menten kinetics for all PHM3His 2nd generation variants. Errors were determined in Sigmaplot using a least squares analysis at the 95% confidence interval.

Protein	V_{max} (mM/min)	Error (mM/min)	K_m (mM)	Error (mM)	Turnover # (mmol oAP / min mmol protein)
PHM3His	0.0042	0.0001	0.0073	0.0013	4.19
PHM3His F114P	0.0100	0.0002	0.0187	0.0016	9.97
PHM3His M121Q	0.0101	0.0004	0.0120	0.0024	10.1
PHM3His F15W	0.0070	0.0001	0.0138	0.0014	6.98
PHM3His F114P M121Q	0.0077	0.0001	0.0223	0.0016	7.69
PHM3His F114P F15W	0.0107	0.0004	0.0174	0.0025	10.7
PHM3His M121Q F15W	0.0068	0.0003	0.0139	0.0027	6.84
PHM3His F114P M121Q F15W	0.0092	0.0003	0.0179	0.0023	9.23

The PHM3His variants' 2nd generation mutants also produced some similar and some different trends. The Phe114Pro/Phe15Trp PHM3His azurin having the highest turnover number (Figure 56, Table 8). The order of activity from highest to lowest for

the PHM3His series is listed in Table 10 and is as follows: Phe114Pro/Phe15Trp PHM3His azurin, Met121Gln PHM3His azurin, Phe114Pro PHM3His azurin, Phe114Pro/Met121Gln/Phe15Trp PHM3His azurin, Phe114Pro/Met121Gln PHM3His azurin, Phe15Trp PHM3His azurin, M121Gln/Phe15W PHM3His azurin, and PHM3His azurin (Table 10). All of the 2nd generation variants increased the turnover number by at least 1.6 times, however only increased by a maximum of 2.5 times to 10.7 mmol oAP min^{-1} $mmol^{-1}$ azurin (Figure 56, Table 8). The trend of decreasing the reduction potential to increase turnover number existed similar to that of the PHM azurin series.

The decrease in reduction potential of the T1 copper center increased the turnover number for all PHM3His azurin variants. The single mutants with one mutation to decrease the reduction potential were all about 2.2-2.5 times faster than PHM3His azurin (Figure 56, Table 8). And all of the top three fastest variants all contained one mutation to decrease the reduction potential by 100 mV. The next fastest variant was the Phe114Pro/Met121Gln/Phe15Trp PHM3His azurin at about two times faster than the parent PHM3His azurin variant (Figure 55, Table 8). After that, the three variants that were all about 1.6 times faster than PHM3His azurin were the doubly reduced Phe114Pro/Met121Gln PHM3His azurin, Phe15Trp PHM3His azurin, and Met121Gln/Phe15Trp PHM3His azurin. Therefore the optimal reduction potential for the PHM3His azurin 2nd generation variants is 250 mV followed by 150 mV.

Like that of the NiR3His azurin variant series, the Phe15Trp mutation with theMet121Gln PHM3His azurin produced a deleterious effect to the turnover number (Table 10). The Phe15Trp PHM3His azurin variant and Met121Gln/Phe15Trp PHM3His azurin variants are both about 1.6 times faster than the parent variant, but are about half

as fast as the Met121Gln variant without the Phe15Trp mutation (Figure 56, Table 8). Like that of NiR3His, there may be an interaction between Met121Gln and Phe15Trp mutation that slows the reaction with the third histidine present in the surface T2 copper binding site.

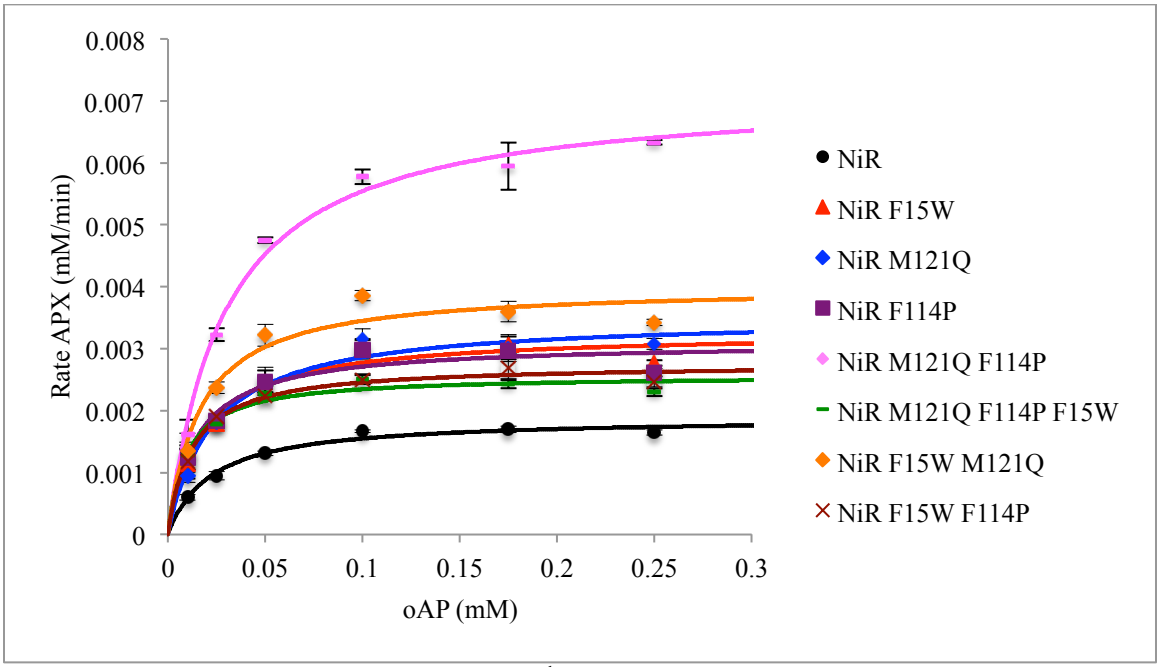

Figure 57. Michaelis Menten plots for all NiR 2nd generation variants. Error bars shown are the standard deviation of the initial linear rate for assays done in triplicate.

Table 9. Michaelis Menten kinetics for all NiR 2nd generation variants. Errors were determined in Sigmaplot using a least squares analysis at the 95% confidence interval.

Protein	V_{max} (mM/min)	Error (mM/min)	K_m (mM)	Error (mM)	Turnover # (mmol oAP / min mmol protein)
NiR	0.0019	0.0001	0.0220	0.0021	1.89
NiR F114P	0.0031	0.0001	0.0146	0.0025	3.11
NiR M121Q	0.0035	0.0001	0.0227	0.0030	3.51
NiR F15W	0.0033	0.0001	0.0179	0.0026	3.27
NiR F114P M121Q	0.0072	0.0002	0.0290	0.0024	7.15
NiR F114P F15W	0.0028	0.0001	0.0121	0.0012	2.75
NiR M121Q F15W	0.0040	0.0001	0.0162	0.0027	4.01
NiR F114P M121Q F15W	0.0026	0.0001	0.0096	0.0026	2.57

Table 10. Relative rankings of the turnover numbers for all 2nd generation variants.

Order	NiR3His	PHM	PHM3His	NiR
1	F114P M121Q	M121Q F15W	F114P F15W	F114P M121Q
2	M121Q	F114P F15W	M121Q	M121Q F15W
3	F114P F15W	F15W	F114P	M121Q
4	Triple	Triple	Triple	F15W
5	F114P	F114P	F114P M121Q	F114P
6	Parent	F114P M121Q	F15W	F114P F15W
7	F15W	M121Q	M121Q F15W	Triple
8	M121Q F15W	Parent	Parent	Parent

The NiR azurin series was the slowest of all four of the parent variants and had the slowest 2nd generation variants. The fastest 2nd generation NiR azurin variant was the Phe114Pro/Met121Gln variant with the lowest T1 copper reduction potential, which was about 4 times faster than NiR azurin (Figure 57, Table 9). This is the same 2nd generation variant that was the fastest in the NiR3His azurin series. The order of activity from highest to lowest for the NiR azurin series is listed in Table 10 and is as follows: Phe114Pro/Met121Gln NiR azurin, Met121Gln/Phe15Trp NiR azurin, Met121Gln NiR azurin, Phe15Trp NiR azurin, Phe114Pro NiR azurin, Phe114Pro/Phe15Trp NiR azurin, Phe114Pro/Met121Gln/Phe15Trp NiR azurin, and NiR azurin. The range of improvement over NiR azurin was as little as 1.3 times faster and as much as four times faster (Figure 57, Table 9).

Again, the trend of decreased reduction potential increasing turnover number held true for the NiR azurin series also. By far the greatest improvement in the turnover number in this series came from the Phe114Pro/Met121Gln NiR azurin variant at about four times faster than NiR azurin. Even without the third histidine, the decreased reduction potential by about 200 mV to about 150 mV for the T1 center, increased turnover number, like that of the NiR3His variation. However, the next closest variant was the Met121Gln/Phe15Trp variant that was only about two times as fast as NiR

azurin. This is a different trend than all other parent variants were no more than 50% apart from one another in reactivity rate increase (Figure 57, Table 9).

Like that of the PHM azurin series, the Met121Gln and Phe15Trp mutation had a positive effect on the turnover number. The Met121Gln NiR azurin variant was about two times faster than the Phe15Trp NiR azurin variant. This indicated an advantageous interaction between the surface copper site of NiR and the Phe15Trp/Met121Gln mutations.

In summary, after all of the 2nd generation variants were assayed, some overall trends appeared. The first trend was the interaction of the Met121Gln and Phe15Trp in both the 3His parent variations. Both variants produced results with decreased turnover numbers from their increased single mutations from Met121Gln when combined with Phe15Trp. However, without the third histidine present, the trend was reversed. Any mutation with Phe15Trp increased the activity of the PHM and NiR parent mutations. This suggests an interaction with the third histidine with both 3His variants' that somehow slowed down the reaction rate and oAP oxidation with the Phe15Trp/Met121Gln azurin series', that doesn't occur when there are only two histidines to bind to at the surface copper-binding site.

The second trend that emerged from all 2nd generation variants was the decrease in reduction potentials increased all the turnover numbers. With the exception of two variants in the NiR3His, all mutations improved activity, and the two variants that decreased activity are within error of the parent variant. A possible explanation for this is that through tuning the reduction potential of the T1 center, we are affecting the electron transfer rates to increase turnover numbers due to Marcus theory. To be more specific,

we are altering the thermodynamic energy required for electron transfer, and according to Marcus theory, are therefore affecting the kinetics of the electron transfer reaction. Further tests are required to support this theory or disprove this theory. To test this, we are currently performing mutations to increase the reduction potential of the T1 copper center that should decrease the turnover number and slow the reaction.

3.8 PHM Assay Investigations

In addition to the PHS oxidation assay, the peptidylglycine α-hydroxylating monooxygenase (PHM) assay was investigated using our variants, hippuric acid (HA), and the electron donor compound ascorbic acid (AA). The goal of this project was to mimic PHM and produce a hydroxylated peptide.

The typical results of an assay are shown in Figure 58, where 250 μM NiR3His was combined with 1 mM HA, and 10 mM AA in 50 mM NH_4OAc buffer at 23 ° C. The chromatograms on the left show three different time points where aliquots were taken; a zero point, 150 min, and 900 min. In all time points of the reaction, the peak associated with hippuric acid (indicated by the red star) doesn't change in retention time or area (Figure 58). Table 11 shows the peak areas and corresponding concentration of both HA and potential α-hydroxylated hippuric acid (AHHA) for all time points from Figure 58. As the reaction proceeds, the retention time stays at 550 seconds, the peak areas remain around 22, and the HA concentration stays at 1 mM.

If the reaction were to have been successful, the hydroxylated hippuric acid would have given a peak with a shifted retention time of about 50 seconds and as the HA peak decreased, the hydroxylated peak would have increased in intensity over time. However, neither the HA peak area changed nor did an AHHA peak appear, indicating no reaction occurred to the substrate HA under these conditions.

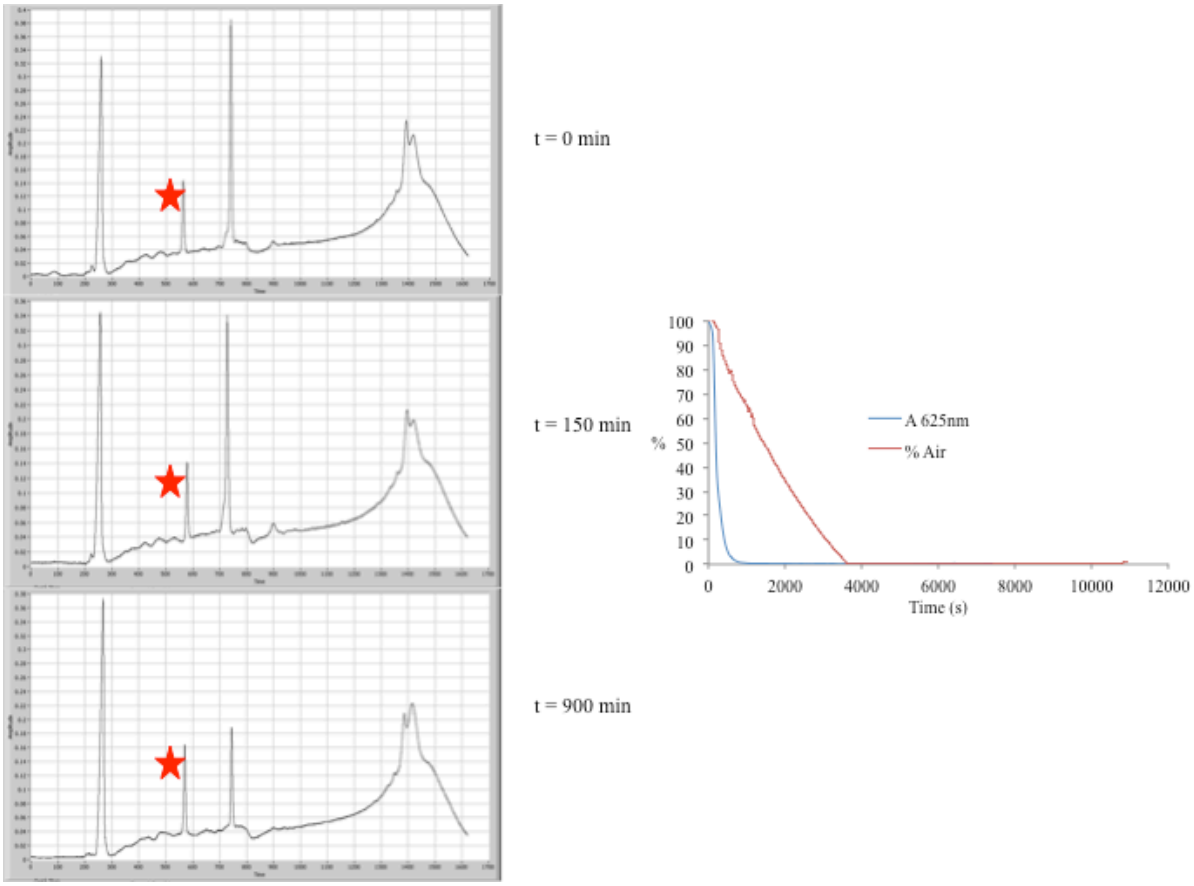

Figure 58. Typical results of a PHM assay with HPLC chromatograms shown on the left, the red stars indicate the hippuric acid peak in each time point, and % air and % 625 nm absorbance shown on the right.

Table 11. Hippuric acid and hydroxylated hippuric acid concentrations at different time points for an assay with NiR3His, hippuric acid, and ascorbic acid.

Time (min)	Peak Area	Concentration HA (mM)	Concentration AHHA (mM)
0	22.27	1.11	0
150	21.68	1.05	0
900	22.07	1.09	0

Although no hydroxylation of HA occurred in the reaction shown in Figure 58, there was a reaction that did occur. This is shown by the disappearance of the 625 nm peak and the decrease in oxygen concentration over time (Figure 58). This indicates that the Cu^{2+} reacted with the electron donor AA, to become the reduced Cu^{1+} species, thus bleaching the 625 nm T1 center azurin absorbance. Cu^{1+} reacting with oxygen followed by hydroxylation of HA was the hypothesized reaction. And, based on Figure 58, the

AA reduced the copper in azurin which then likely reacted in a known reaction with oxygen to produce reactive reduced species of oxygen.[13] The oxygen content slowly decreased to 0 % over ~3500 s. Since there was no hydroxylation activity, the reduced species of oxygen reacted with the protein or other species in solution to consume the O_2. Due to the lack of evidence in the chromatograms, the reaction was never able to utilize the reduced copper azurin to form a copper-oxygen species active or specific enough to hydroxylate HA.

In further attempts to find HA hydroxylation activity, we attempted this reaction with all 4 parent variants, varied ascorbic acid concentrations, varied buffers and pHs, and added hydroxylating shunt agents (see below). Based on previous work, the main variant utilized for this study was NiR3His azurin. But, PHM azurin, PHM3His azurin, and NiR azurin were all used in an attempt to facilitate hydroxylation. The parent azurin variants did not produce hydroxylation.

The initial assay contained 1 mM AA as the electron donor for the system and this was our first area to change in an attempt to facilitate hydroxylation. The AA was increased from 1 mM to 10 mM, and then finally to 30 mM. The increase in AA to the system did not facilitate hydroxylation. We then decided to perform all subsequent assays using 10 mM and 30 mM AA, to ensure all coppers were always reduced and able to react with oxygen to hydroxylate HA.

The next logical variable to manipulate was the buffer and pH. All of our assays were originally performed in 50 mM NH_4OAc buffer at pH 5.1. To optimize this, we consulted with the literature to find an optimal pH and buffer system, and it was found that a pH of 5.8 in 50 mM MES was optimal for the native PHM system.[14] We tried 50

mM MES pH 5.8 for our system, and after that failed to produce hydroxylation, we tried; 50 mM NH_4OAc at pH 6.35, 50 mM potassium phosphate at pH 6.35, 50 mM Tris at pH 7.0, and 50 mM NH_4OAc at pH 4.1. Again, none of these buffers demonstrated evidence of hydroxylation with either 10 mM or 30 mM AA.

Our final variable to manipulate was to try a stronger hydroxylating agent or use a peroxide shunt. Based on the literature,[15] we tried reactions with the known hydroxylating agents; H_2O_2, tetrabutylammonium iodate, mCPBA, $Ca(ClO)_2$, and $KMnO_4$. Again, none of these reactions produced evidence of a singly hydroxylated AHHA product. The only reagent that facilitated a reaction with HA was $KMnO_4$. However, the products formed did not have HPLC retention times of AHHA, but rather formed unidentified breakdown products of HA.

We were not able to accomplish the goal of creating a functional mimic for the oxidoreductase PHM. Rather we pursued the more successful PHS assays.

3.9 Wild Type Azurin X-Ray Crystal Structure Solving Process

As described in Section 2.2, a crystal sufficient for a dataset was grown, known as 61 D4. After the full X-ray diffraction dataset was gathered, the initial structure solution began in CrystalClear 2.0r7 with the determination of the crystal's unit cell. In order to obtain a more accurate unit cell than the one determined from the crystal screenings, we used 8 frames at least 25 ^{o} frames apart from each other in the dataset to determine the unit cell. This was an important step to ensure the accurate and complete harvesting of all reflections in the dataset. Before the reflections were harvested, a mask file was created over the beam stop and beam stop arm, and applied to all images preventing erroneous harvesting of spots near the beam stop.

All 782 images were then integrated using the d*TREK program embedded into CrystalClear 2.0r7, to harvest all reflections. Only reflections with an intensity/σI (<I/σI>) ratio of 3.0 were harvested. The I/σI is the relative intensity of the reflection related to the standard deviation of the baseline of the image. If the reflection had a ratio less than 3.0, it was considered too weak and was not harvested. During the harvesting, CrystalClear 2.0r7 continually updated the unit cell and mosaicity of the crystal. This allowed the complete harvest of all reflections with slight deviation from the determined unit cell due to the crystal's inherent disorder.

The next operation in CrystalClear 2.0r7 was to determine the Laue symmetry and space group. The reflection list generated from integration above was used to determine the crystal's Laue symmetry in CrystalClear 2.0r7's Laue check operation. For 61 D4, the highest Laue symmetry was 2/m. Next, the crystal's space group was determined by checking the dataset for systematic absences based on the Laue symmetry previously

determined. The <I/σI> tolerance is used to determine this and for crystal 61 D4, C2 was the crystal space group as this was the highest symmetry space group that lacked systematic absences.

The final operation in CrystalClear 2.0r7 was the scaling and averaging of all reflections harvested by integration. Due to factors like exposure time, possible radiation damage, fluctuating source X-Ray intensity, and most importantly varied path length through the crystal due to varied orientations, all frames need to be scaled and averaged to each other to have the correct representation of reflection intensity. This process was repeated until a scaled and averaged file had the statistics listed in Table 12. These values indicate the point at which the data should be cut off and therefore the resolution of the structure. It is important to have an I/Sig un-averaged of 2.0 or greater, and the corresponding resolution shell should have an R_{merge} shell of less than 0.4. Using the statistics output from scale and average in CrystalClear 2.0r7, the optimum resolution of the dataset for crystal 61 D4 was 1.68 Å.

Table 12. Outermost shell statistics from scale and averaging in CrystalClear 2.0r7 to determine the resolution of the dataset for WT Az 61 D4.

Resolution Range (Å)	I/Sig un-averaged	Reduced χ^2	R_{merge} Shell
1.74-1.68	2.0	1.26	0.328

The final statistics for the scaling and averaging for crystal 61 D4 are shown in Table 13. The unit cell lattice symmetry was determined to be monoclinic and had a C2 spacegroup. This is different from many of the previously solved crystal structures in our lab and in the literature as azurin more commonly packs in orthorhombic lattice symmetry with higher symmetry point groups. This meant the crystal 61 D4 was less symmetrical in its azurin packing, and therefore required more unique reflections to collect an entire dataset. Even with the lower symmetry packing of azurin, the crystal

still had a good mosaicity of 0.53°. The entire dataset had 903,540 reflections and 118,674 unique reflections. We took an approach that allowed us to collect approximately 7.5 times more data than one dataset would have encompassed as indicated by our average redundancy of 7.61. This contributed to our % completeness being 100%, and provided us with an excellent dataset for solving. Using this information, the next step was to transfer the scaled and averaged reflections to another program and continue solving the structure.

Table 13. Scaling and Averaging statistics for WT Az crystal 61 D4 for all resolution shells and the last resolution shell.

	All Resolution Shells	Last Resolution Shell
Space Group	C2	
Unit Cell Dimensions (Å, °)	a=109.20 b=97.16 c=100.33 α=90 β= 94.75 γ= 90	
Lattice System	Monoclinic	
Laue Symmetry	2/m	
Mosaicity (°)	0.53	
Total # Reflections	903,540	
Unique # Reflections	118,674	
Resolution Range (Å)	35.38-1.68	1.74-1.68
Average Redundancy	7.61	6.58
Completeness (%)	100	100
R_{merge}	0.070	0.328
R_{meas}	0.075	0.355
Output <I/σI>	11.6	4.0

Once the dataset had been scaled and averaged for all coordinates and intensities in CrystalClear 2.0r7, the reflection list was then loaded in to CCP4, another software that enables us to perform the phase solution of the structure by the molecular replacement method. Because CrystalClear 2.0r7 uses d*TREK, the reflection list was

formatted to be a .ref file, however CCP4 uses a .mtz file. Therefore the next operation for solving the structure was the conversion of the .ref file to a .mtz file for use in CCP4.

Once converted, the solvent content was calculated using the Mathews coefficient. The Mathews coefficient is based on the molecular weight of the protein and the unit cell volume, and is used to calculate the approximate solvent content.[6] The solvent content analysis provided an estimate of the amount of monomers per unit cell by taking into account the number of monomers per asymmetric unit. Typically solvent content is around 43%, but can vary from as little as 27 % to as high as 65 %.[6] For the 61 D4 crystal, the solvent content for 8 monomeric units came out to be 48.09 % solvent. By investigating all possible solvent content options, these parameters were found to be the best for solving the structure.

Once the number of monomers per unit cell was estimated, the next step was the calculation of the B-Factor. B-factors represent the thermal disorder and amount of electron density displacement due to thermal motion and crystal disorder.[8] To find this factor, CCP4 uses an already existing structure to estimate the B-Addition (BADD) value, or the value to add to the already solved B-factor we use as an input. We used the already solved azurin structure by Nar et al. in the protein data bank as 4AZU.[7] The B-factor for 4AZU is 16.656. The 61 D4 dataset was calculated by CCP4 to have a B-factor of 21.141, thus the BADD value was 4.485.

Next, a molecular replacement was performed with the 4AZU pdb, using rotation and translation functions, an 8 monomer search, and using the determined BADD value. Molecular replacement was able to find 8 monomers per asymmetric unit.

The final step for the WT structure solution was to perform an initial refinement with Refmac5 to match the experimental electron density with the generated structure. The initial refinement was done using restrained refinement without TLS parameters, babinet scaling, and local auto non-crystallographic symmetry (NCS) restraints. Because of the large amount of monomers per asymmetric unit, local NCS restraints were used to find an initial structure to begin refining from.[8] Auto NCS restraints are commonly used for structures with large numbers of monomers and provide a starting point for future refinement.[8] The NCS restraints functions by first aligning all chains using the Needleman-Wunsh[9] method and then finding a correspondence between atoms. When using local restraints as opposed to global restraints, the program makes lists of corresponding interatomic distances within 5 residue windows, and designs weights to use for each chain during refinement.[8] In addition to the NCS restraints, the initial refinement was run for 100 cycles, as opposed to the traditional 10 cycles, due to the large amount of experimental data. This was found to greatly improve the R_{factor}[10] and the R_{free}[11] values and produce a better structure to start refinement from. The starting point for refinement was an R_{factor} of 32.87 % and R_{free} of 35.28 %. R_{factor} is used to gauge how well the refined structure fits to the electron density map as it is defined as a ratio of the sum of the differences between experimental observations and the ideal calculated values.[10] R_{free} is similar to the R_{factor}, however it uses 5% of the total reflection data that is excluded from the structure refinement.[11] Both provide information on how accurate the fit is to matching the experimental electron density.

After the initial refinement, our WT azurin R factors obtained above were an indication of a good structure. However, there was much room for improvement. The

structure was therefore further refined using a program called Coot. The first step of the continued refinement was to add 8 Cu^{2+} ions at the T1 copper centers using Coot's "get monomer" tool and the difference map peak generator.[18] Then, the structure was refined using translation libration screw-motion (TLS) and restrained refinement without NCS restraints (Figure 59). TLS refinement gives an estimate of the anisotropic displacement of atoms during refinement and is useful for solving protein structures.

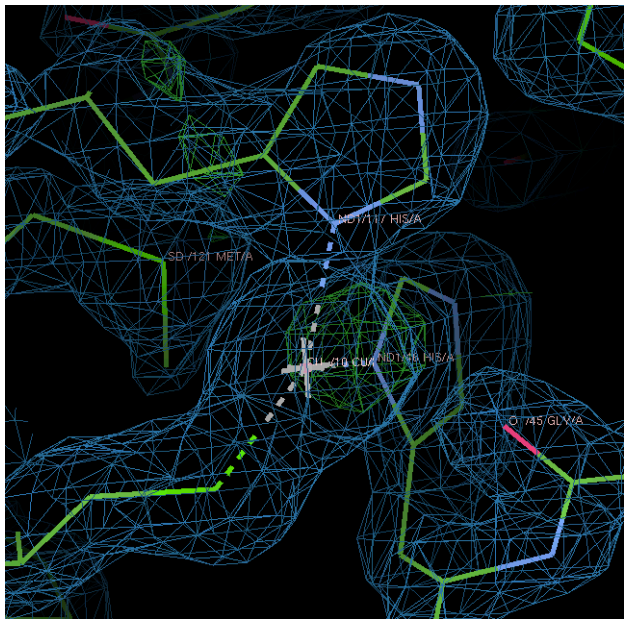

Figure 59. Type 1 copper center on chain A in the 61 D4 wild type azurin with the copper ion added using Coot's "get monomer" and difference map peak generator. This image was made in Coot.[18]

The second refinement round in Coot was to fix was the N-terminus of each protein chain. In the initial refinement, the N-terminus of each chain was flipped and incorrectly matched to electron density that was actually belonging to a Cu^{2+} ion and a Tris (Figure 60). To correct this, Cu^{2+} ions had to be placed according to the difference map peak generator in Coot. Once the Cu^{2+} ions were placed using Coot's "get monomer" feature a Tris molecule was placed at seven of the eight chains. Only seven of the eight Tris' were assigned, as the 8th Tris had a negative impact on the R_{factor} and R_{free}

due to the lack of ordered electron density at one chain. Then, the N-terminus was rotated manually in Coot and positioned in an approximate position for binding to the Cu^{2+}. After this, the structure was refined in CCP4's Refmac5 using TLS and restrained refinement, and the positioning of all chelating ligands was resolved sufficiently (Figure 60).

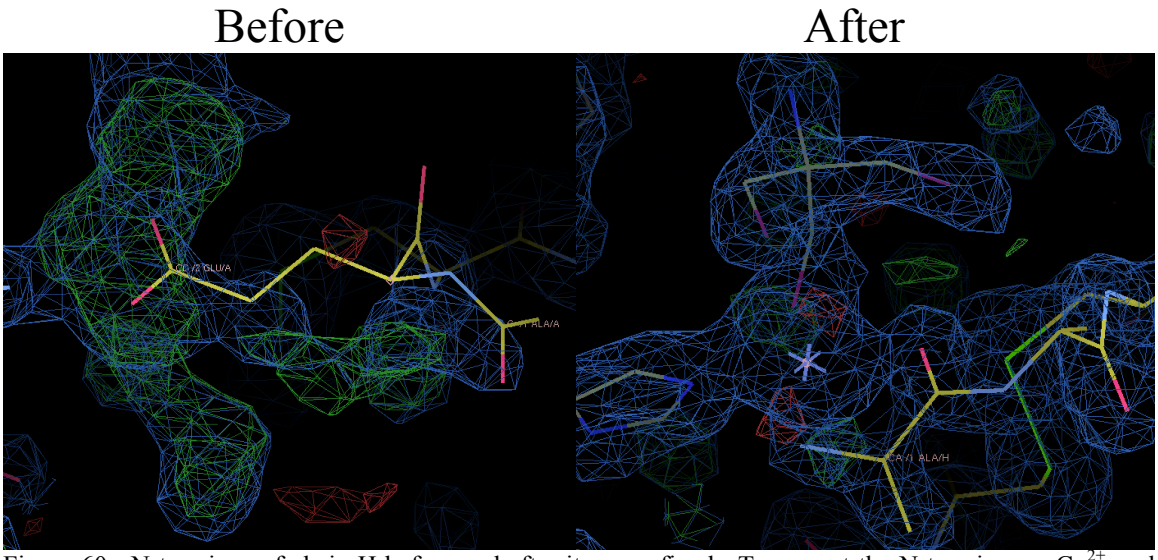

Figure 60. N-terminus of chain H before and after it was refined. To correct the N-terminus, a Cu^{2+} and Tris, had to be added, and then the N-terminus was able to be rotated and auto fit to the electron density. This was then run through refinement in Refmac5. This image was made in Coot.[18]

Once these initial operations for refining were completed, each amino acid was examined to ensure a good fit to electron density. To do this, Coot's real space refine was used to match the model to electron density both on the protein backbone and side chains. After a thorough investigation of all chains, an additional eight Cu^{2+} ions were added for sixteen total Cu^{2+} ions and seven Tris's. The R_{factor} and R_{free}, were improved to 26.69 % and 30.65 % respectively. However, many peaks in the difference map still existed indicating the existence of unassigned electron density.

The next refinement step involved the addition of water molecules to the model, using Coot. To do this, the most intense peaks in the difference map were assigned as

waters that were within hydrogen bonding distance (up to 4 Å) of the protein structure (Figure 61). Figure 61 shows the positioning of a water molecule 2.8 Å from the nitrogen of the protein backbone. This water was placed and refined to the final location shown in Figure 23. Water molecules were added 20 at a time and then sent through 10 cycles of TLS and restrained refinement in Refmac5. After each refinement, all waters were examined in order to ensure the placement was correct, and that the R_{factor} and R_{free} had decreased. In total, 293 water molecules were added to the structure and the R_{factor} and R_{free} were decreased to 24.73 % and 29.23 % respectively. At this point, adding waters no longer decreased the R_{factor} and R_{free}, and therefore no more waters could be reasonably added.

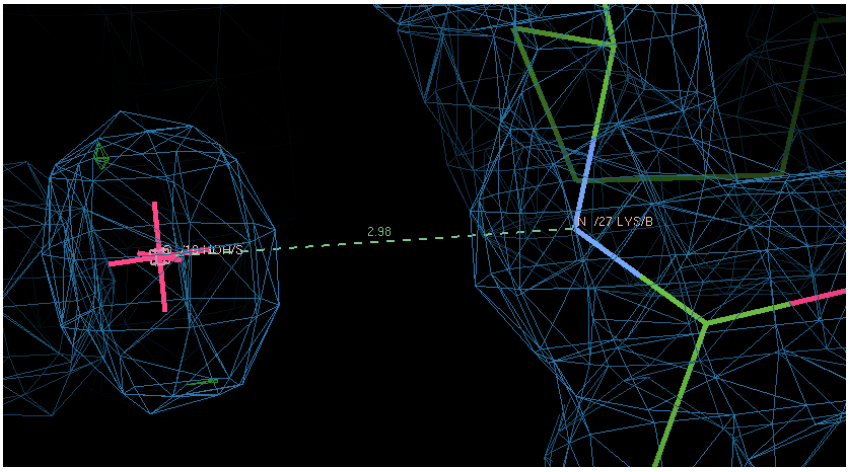

Figure 61. Placement of a water within hydrogen bonding distance of the NH_2 backbone of lysine 27 on chain B. This image was made in Coot.[18]

The final improvement of the R_{factor} and R_{free} values came after observing a significant amount of unassigned and incorrectly assigned electron density near the Cu^{2+} ions at each N-terminus (Figure 62). After many attempts to improve the model at these sites, it was discovered that the Tris molecule chelating the Cu^{2+} ion needed to be split into two different orientations each with 50 % occupancy across all atoms. After

refinement, the electron density was correctly assigned and the Tris was both N and O bound to copper (Figure 62). The Tris' had settled into their correct orientation based on the visual inspection and there was a significant decrease in the R_{factor}. There was no preference for how the Tris would bind to the copper, and thus, there was an even distribution of N and O bound copper Tris chelation at all Tris'. The final R_{factor} and R_{free} were 21.93% and 27.01 % respectively.

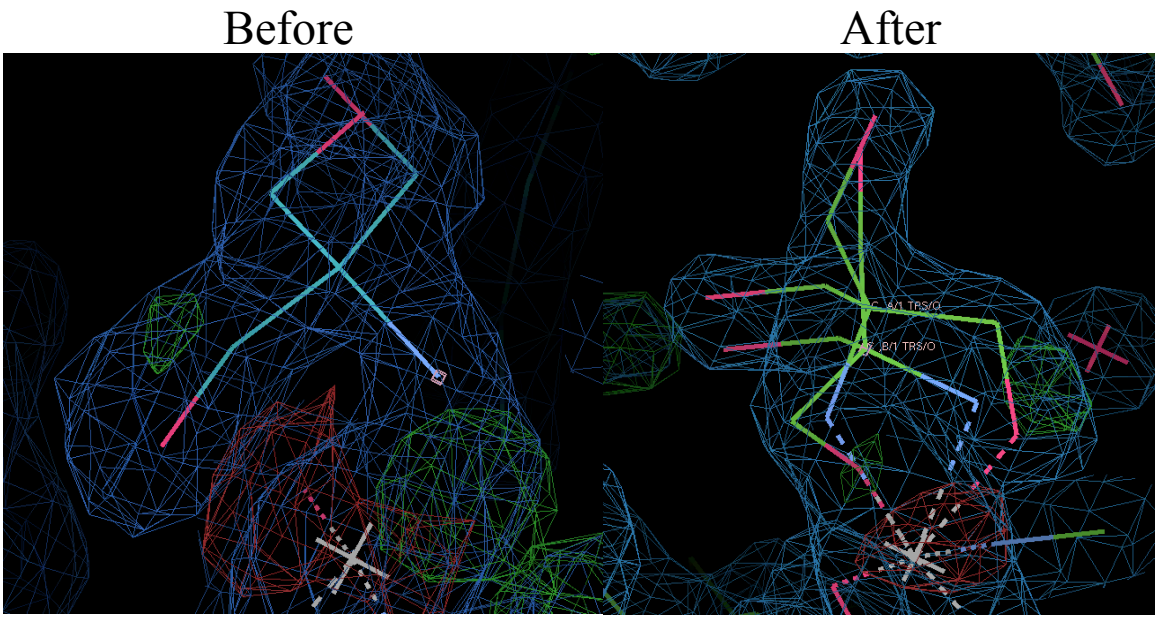

Figure 62. View of Tris at the N-terminus of 7 chains in the octomeric structure of WT Az 61 D4. The left image is before the Tris was split and mismatched electron density exists, while the right has a split Tris to account for both binding motifs to the copper from the Tris, both N-bound and O-bound. This image was made in Coot.[18]

At this point in the solving of the WT structure, no more refinement was beneficial to the R_{factor} and R_{free}, and therefore the structure was finished being refined. Waters could still be added to the structure based on the difference map generated by Coot, and more refinement could have been performed, but this wasn't beneficial to the solving statistics and would have resulted in an over-fitting of the data.

Figures 63, 64, and 65 are all interactive menus generated by Coot that were used to gauge the quality of the structure. The first density fit bar graph has a score from 0-1, with a better fit having a lower number, displayed as a short green bar. Figure 63, indicates a good fit on all amino residues by the height and color of their density fit bar graphs. There are a few bars with an orange or yellow color that indicate a less than ideal fit to electron density that arise from a lack of electron density to match the model with.

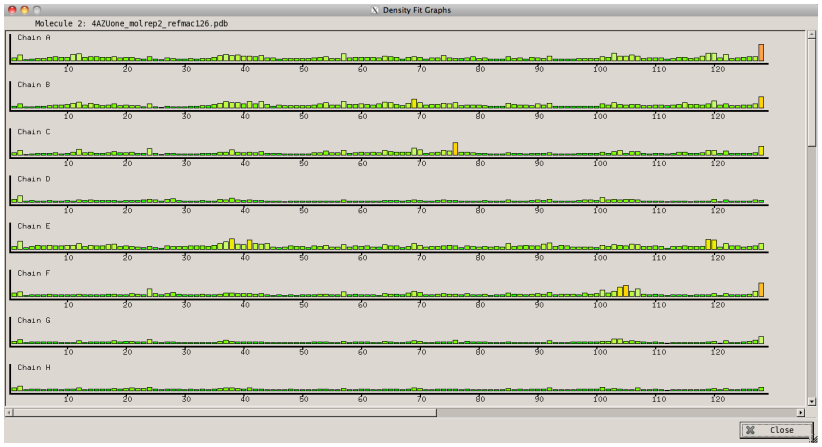

Figure 63. Density fit graph for WT Az crystal 61 D4 generated by Coot for all amino acid residues.

In addition to fitting electron density, another parameter checked was the geometry of the amino acids. Each amino acid should match the electron density and have the acceptable geometry commonly known for that amino acid. Like the electron density graph, the geometry analysis is displayed as a score from 0-1 and visualized as bar graph with a low green bar being a good score. Figure 64 shows the final geometry analysis for crystal 61 D4, with low green bars except for three, indicative of a good geometry analysis. The red and yellow bars come from residues that have a strained geometry due to disorder and lack of electron density in the dataset.

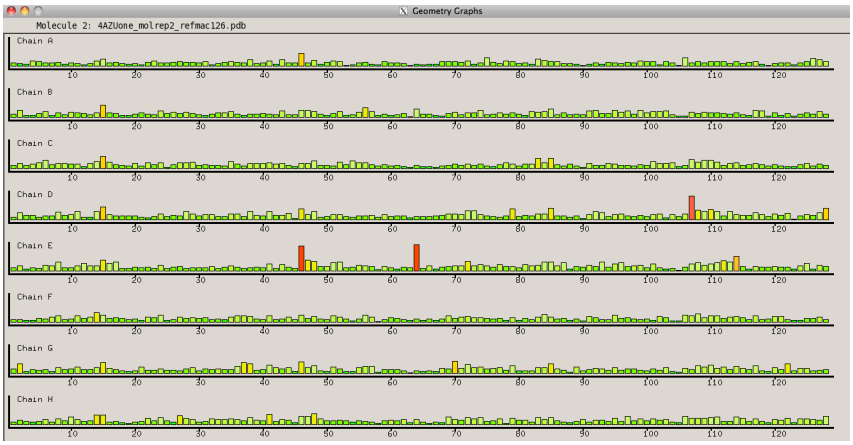

Figure 64. Geometry analysis of WT Az crystal 61 D4 generated by Coot for all amino acid residues.

Another analysis tool we used in Coot for assessing the structure was the Ramachandran plot. This tool plots each amino acids' torsion angles on the amino acid back bone between the N-Cα, called phi torsion angle and the Cα-C, called psi torsion angle.[12] Due to steric clashing, these angles should only fall within a small region of the plot, and therefore any outliers would need to be questioned.[12] Figure 65 shows all amino acids are well within the yellow and pink areas that correspond to accepted phi and psi angles. This shows all values for the Ramachandran plot are within the accepted torsion angles for a peptide backbone and support the final refined structure.

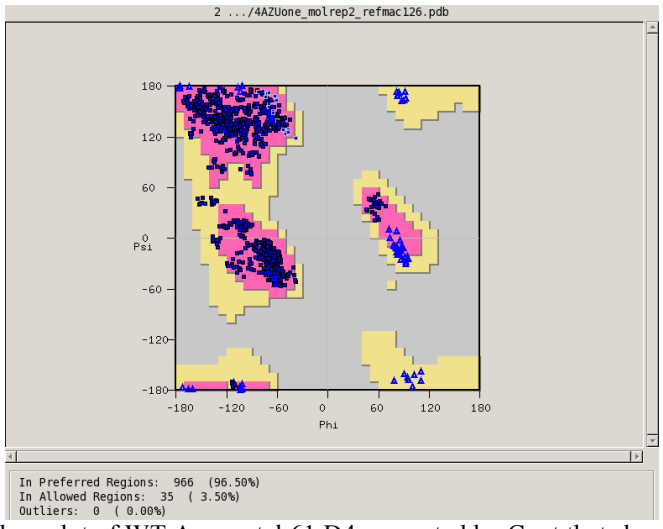

Figure 65. Ramachandran plot of WT Az crystal 61 D4 generated by Coot that shows the plot of phi vs psi for all amino acid residues.

3.10 Analysis of WT Az Crystal Structure

After all the validations were taken into account, one can begin to analyze the structure. Figure 66 shows an example of the fit from the theoretical solved structure to the experimental electron density. The experimental blue electron density is fit well by the green model. This is consistent throughout the entire structure and is indicative of a good dataset and solution.

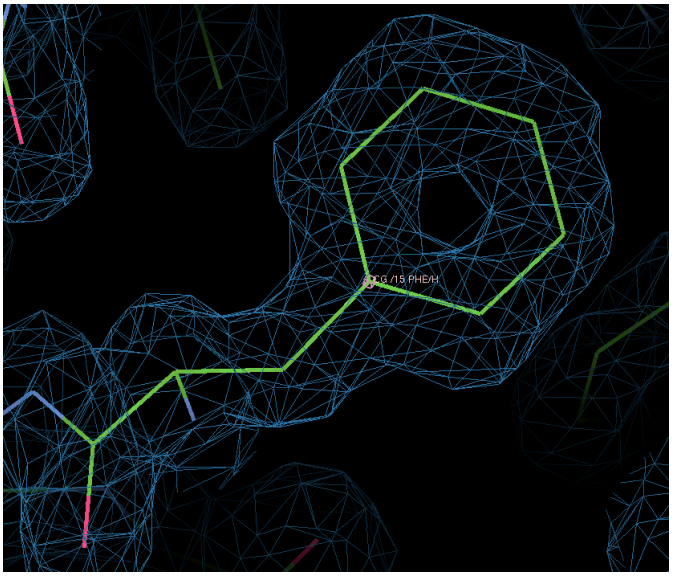

Figure 66. Phenylalanine residue 15 on chain H of WT Az crystal 61 D4. The model green line structure fits the electron density indicated by blue colored electron density indicating a good match of theory to experiment. This image was made in Coot.[18]

The crystal 61 D4 for wild type azurin packed into a monoclinic unit cell with eight monomeric units (Figure 67). Figure 67 shows all 8 monomeric chains oriented within the unit cell. Seven of the eight chains are in a row with one by itself to the side. The separate chain by itself, is also dimerized with a chain in the bottom row, but in symmetry related equivalent position and is shown in a separate area within the unit cell. This is different from other azurin crystal structures in the literature, for example the 4AZU structure packed into an orthorhombic symmetry with four chains in a tetrameric cluster of azurin.[7] This makes the 61 D4 wild type azurin crystal structure interesting in

that eight monomeric chains were formed in the unit cell as no other azurin structure in the protein data bank has eight monomeric chains. In fact, there is only one structure with more than four monomeric units that contains twelve monomeric chains,[17] but this is a highly mutated variant with direct mutations to the T1 site. Therefore, 61 D4 is the first octameric wild type azurin crystal structure.

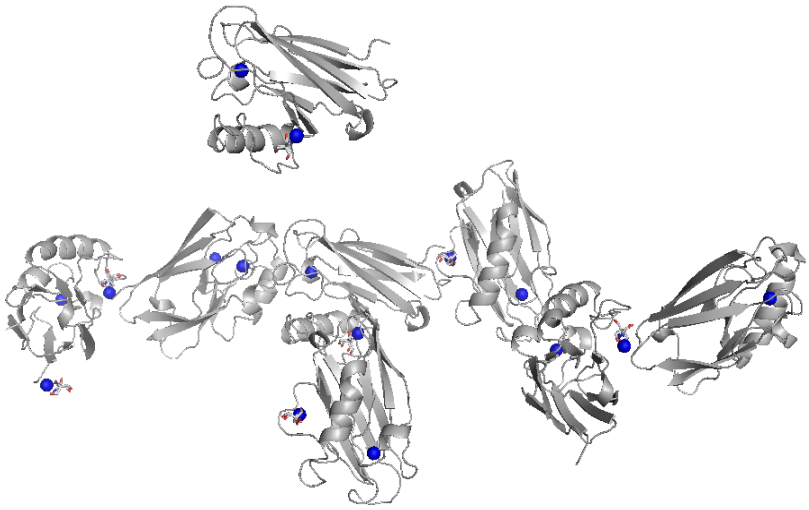

Figure 67. Final crystal structure of the WT Az 61 D4 showing all 8 monomers and the Cu^{2+} ions. This image was generated in Pymol.[19]

Within the crystal packing, the wild type crystal structure was found to dimerize at the N-terminus and the His83 residue of the neighboring monomer through an additional Cu^{2+} ion (Figures 68-70). The second Cu^{2+} ion was coordinated by the carbonyl on the backbone of the N-terminus, and the amine group of the N-terminus glycine residue, both N and O bound from a Tris, N-bound from the histidine 83 residue of another monomer, and a water (Figure 69). The Tris molecule was split into two conformations as described above in order to improve the R_{factor} and R_{free} to more correctly solve the structure (Figure 68).

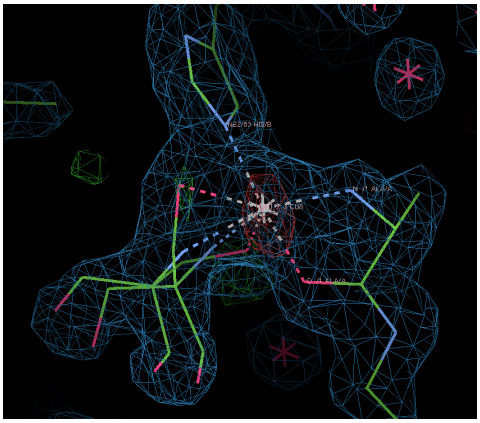

Figure 68. Dimerization site of the WT Az crystal at the N-terminus of chain A and H83 residue of chain B shown with a split Tris conformation. This image was made in Coot.[18]

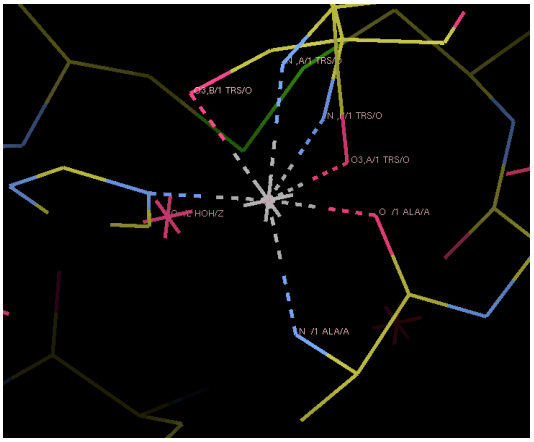

Figure 69. N-terminus of the 61 D4 wild type azurin crystal structure showing the coordination of the surface copper with the carbonyl on the backbone of the n-terminus, and the amine group of the n-terminus glycine residue, N and O bound from the Tris, the N-bound from the histidine 83 residue of another monomer, and a water. This image was made in Coot.[18]

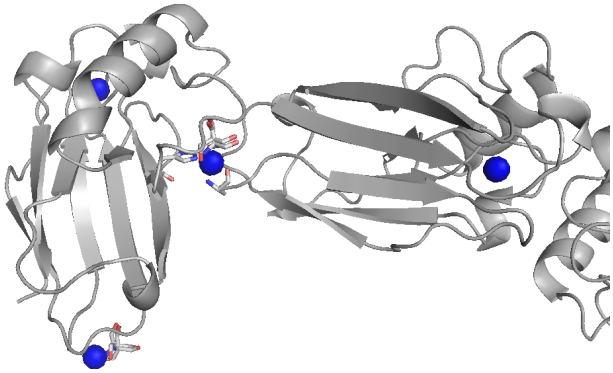

Figure 70. Dimerization of the WTAz structure through the N-terminus H83 on another monomer. This image was generated in Pymol.[19]

The copper ion was coordinated in an elongated octahedral geometry. This is shown by the N-terminus glycine backbone carbonyl, N-terminus backbone amine group, and both Tris coordination N and O bound coordinations in the equatorial plane shown by all these residues having a bond distance of about 2.0 Å (Table 14) and the axial water and His83 nitrogen binding at about 2.46 Å and 2.1 Å, respectively. The axial ligands are slightly elongated, indicative of some Jahn-Teller distortion with an octahedral coordinated Cu^{2+} ion (Table 15).

Table 14. Bond distances of the coordinating ligands around the dimerized surface Cu^{2+} ion on the 61 D4 WT Az crystal structure.

Coordinating Ligands	Bond Distance (Å)
Carbonyl	2
N-term N	2.02
N-Bond Tris	2.03
O-Bound Tris	2.07
His83 N	2.1
Water	2.46

The secondary structure of the individual chains of the 61 D4 wild type azurin structure was defined by 2 β-sheets with one small α-helix arranged in a double wound Greek key topology (Figure 71). The protein contained one T1 copper center and a surface bound copper at the N-terminus of each chain. The secondary structure was the same as that of other solved crystal structures of the wild type azurin that have been published.

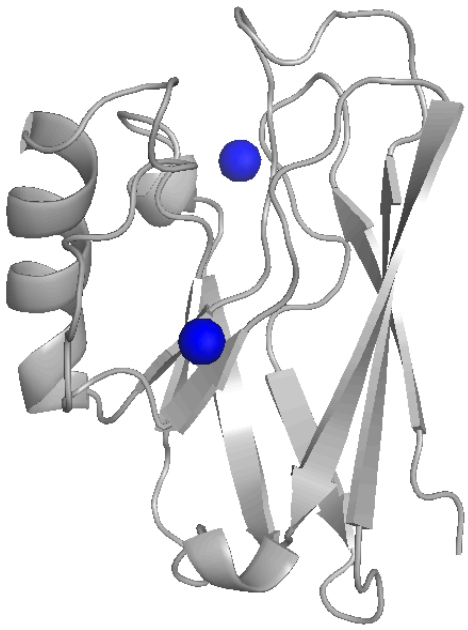

Figure 71. Monomeric structure of the final solved 61 D4 wild type azurin crystal structure showing 2 Cu^{2+} ions, a β-sheet motif with a small α-helix. This image was generated in Pymol.[19]

The active site of the 61 D4 wild type structure is that of a typical copper center in azurin. It is coordinated by two histidines, one cysteine, one methionine, and an H-bonded glycine carbonyl backbone (Figure 72). The coordination is similar to the wild type azurin crystal structure published as 4AZU. When the bond distances are compared (Table 15), both the histidine bonds are about 1.1-1.2 times longer than the 4AZU structure, and the cysteine bond is about 1.2 times shorter than 4AZU. This indicated the copper at the T1 center is shifted slightly towards the cysteine when compared to the 4AZU structure. However, this deviation is within the resolution of both structures and could therefore be the same distances within error. The 4AZU structure has a resolution to 1.9 Å, where as the 61 D4 structure is out to 1.68 Å. The higher resolution structure of the 61 D4 could be a more accurate representation, however they both share the same geometry and coordination sphere of a T1 copper center.

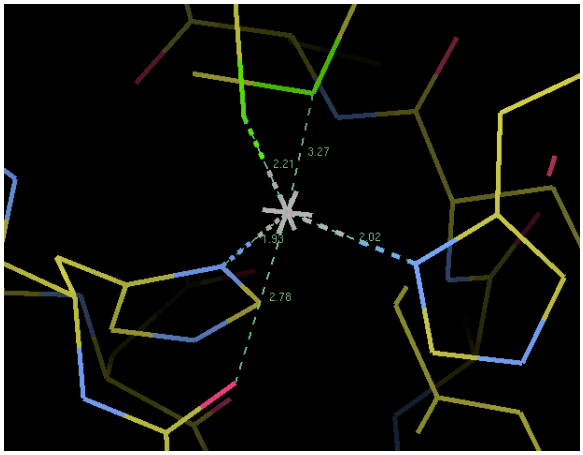

Figure 72. T1 copper center of the 61 D4 wild type crystal structure showing the coordination by 2 histidines, 1 cysteine, 1 methionine, and a h-bond from a glycine carbonyl backbone. This image was made in Coot.[18]

Table 15. Type 1 copper center bond distances of crystal 61 D4 wild type azurin and protein data bank 4AZU wild type azurin crystal structure.

Coordinating Residues	61 D4 bond distances (Å)	4AZU bond distances (Å)
His117	2.02	2.42
His46	1.93	2.15
Cys112	2.21	1.79
Met121	3.27	3.21
Gly45	2.78	2.47

This was a useful experiment for our lab as we have solved the structures of other azurin variants under these same conditions. This structure was a useful control for our crystallography investigations as we can now determine if any observations from current and future crystal structures are artifacts of crystallization, a result of our mutations, or are significant structural discoveries. The N-terminus dimerization with the His83 site observed in the WT structure can be attributed as an artifact of crystallization due to the conditions we use and not a result of our mutations. This is significant for our studies so more direct future comparisons can be made between our many PHM azurin structure and both our phenylalanine variant structures.

Conclusions and Future Directions

We successfully designed a functional protein mimic for PHS that is comparable to the native system. In doing so, we created an adapted PHS activity assay for azurin variants using a two electron reduced tBHP shunt at a pH of 7.5 in 20 mM potassium phosphate buffer. Using these conditions we gathered Michaelis-Menten kinetic parameters for all of our parent variants and found our NiR3His azurin variant to be the fastest. In addition to this, we assayed all of our parent variants with a series of 2nd generation mutations that decreased the reduction potential of the T1 center in azurin. We found the most active variant to be the NiR3His Phe114Pro/Met121Gln variant, which was approximately 40 times slower than the native PHS system with a turnover number of 27.3 mmol oAP min^{-1} mmol^{-1} azurin. A future direction of this project would be an investigation using O_2 as the oxidant instead of the tBHP shunt.

All 2nd generation variants showed increased turnover number with a decreased reduction T1 copper center reduction potential. This is an area for further study currently as we test the hypothesis that a decrease in reduction potential may effect the electron transfer rates and accelerate the reaction due to Marcus theory. If this hypothesis stands, increasing the reduction potential should decrease the turnover number with each parent variant. Studies are currently underway with azurin variants that have an increased reduction potential at their T1 copper center to test this hypothesis.

The mechanism of these PHS models is believed to be electron transfer to the native T1 copper center in azurin and then to the mutated surface T2 copper center, which then reacts with tBHP. Thus far, our experiments support this hypothesis, however more experiments to test this are required. Because the T1 Hg T2 Cu NiR3His azurin variant is

about 75 % as fast as our T1 Cu T2 Cu variant, it seems that two copper ions are not required for activity. However, this could be indicative of a different mechanism occurring when the protein is loaded this way, with electrons going directly to our T2 copper center and being reoxidized immediately by tBHP. Therefore, at this point, we can state that we have created a functional mimic for PHS and can not state that we have a mechanistic mimic for PHS. An area of future exploration for this is to test the fast and slow phases of the models with varied metal loaded proteins and examine the reduction and reoxidation of the T1 copper center during the tBHP assay.

Lastly, I was able to gather the crystal structure for wild type azurin under the conditions we use to crystallize other azurin variants. The structure had an octameric unit cell with a monoclinic unit cell and each protein was similar to other wild type azurin crystal structures in the literature. The T1 center was coordinated by two histidines, one cysteine, one methionine, and a hydrogen bound carbonyl from a nearby glycine residue. The N-terminus was found to dimerize through a surface bound Cu^{2+} ion to the histidine 83 site of another monomeric azurin chain.

This was a useful control to our crystallographic studies for our azurin variants. An area of future study is to crystallize our PHM His83Asn variant. This variant has an asparagine at the His83 site that will prevent the protein from dimerizing through the His 83 site and could prevent the N-terminus dimerization as well. There are currently studies underway to crystallize this variant under apo conditions to get the non-dimerized structure PHM azurin structure.

Chapter 1 References

1. Freeman J.; Nayar P.; Begley T.; Villafranca J. Stoichiometry and Spectroscopic Identity of Copper Centers in Phenoxazinone Synthase: A New Addition to the Blue Copper Oxidase Family. *Bioch,* **1993**, 32, 4826-4830.
2. Smith W.; Camara-Artigas A.; Wang M.; Allen J.; Fransisco W. Structure of Phenoxazinone Synthase from *Streptomyces antibioticus* Reveals a New Type 2 Copper Center. *Bioch.* **2006,** 45, 4378-4387
3. Roses-Hill, M.; Goodwin, C.; Burton, S. Phenoxazinone Synthase: what's in a name? *Tren. in Bioch.*, **2009**, 27.
4. *The Clinical Use of Actinomycin: Cancer Chemotherapy Reports;* Frei E. Vol. 58 Jan 1974
5. Barry, C.; Nayar P.; Begley T. Phenoxazinone Synthase: Mechanism for the Formation of the Phenoxazinone Chromophore of Actinomycin *Bioc.* **1989**, 28, 6323-6333
6. Eggert et al. Laccase-mediated formation of the Phenoxazinone derivative, cinnabarinic acid. *FEBS Lett*. **1995**, 376, 202-206.
7. Solomon E.; Sundaram U.; Machonkin T.; Multicopper Oxidases and Oxygenases. *Chem. Rev.* **1996**, 2563-2605
8. Suzuki, H.; Furusho, Y.; Higashi, T.; Ohnishi, Y.; Horinouchi, S. A novel o-aminophenol oxidase responsible for formation of the phenoxazinone chromophore of grixazone. *J. Biol. Chem.* **2006**, 281, 824-33.
9. Nair, P.; Vaidyanathan C. Isophenoxazine synthase. *Biochim. Biophys. Acta.* **1964**, 81, 507-516.
10. McIntyre, N.; Lowe, E.; Merkler, D. Imino-oxy Acetic Acid Dealkylation as Evidence for an Inner-Sphere Alcohol Intermediate in the Reaction Catalyzed by Peptidylglycine α-Hydroxylating Monooxygenase. *J. Amer. Chem. Soc.* **2009**, 131, 10308-10319
11. Toussaint, O.; Lerch, K. Catalytic Oxidation of 2-Aminopehnols and Ortho Hydroxylation of Aromatic Amines by Tyrosinase. *Bioch.* **1987**, 26, 8567-8571.
12. Osborne, R.; Zhu, H.; Iavarone, A.; Blackburn, N. Interdomain Long-Range Electron Transfer Becomes Rate-Limiting in the Y216A Variant of Tyramine β-Monooxygenase. *Bioch.*, **2013** 52, 1179-1191.
13. Katz, E.; Weissbach, H. Biosynthesis of the Actinomycin Chromophore; Enzymatic Conversion of 4-methyl-hydroxyanthranilic Acid to Actinocin. *J. Biol. Chem.* **1962**, 237, 882-886.
14. Nishimura, J.; Golub, E. On the effects of cyanide on phenoxazinone synthetase. *Biochim. Biophys. Acta*, **1969**, 191 724-726.
15. Pinho, D.; Besson, S.; Brondino, C.; De Castro, B.; Moura, I. *Eur. J. Biochem.* **2004**, 271, 2361-9.
16. LaCroix, L.; Shadle, S.; Wang, Y.; Averill, B.; Hedman, B.; Hodgson, K.; Solomon, E. *J. Am. Chem. Soc.* **1996**, 118, 7755-68.
17. Altschul, S.; Wooton, J.; Gertz, E.; Agarawala R.; Morgulis, A.; Schaffer, A.; Yu, Y. Protein database searches using compositionally adjusted substitution matrices. *FEBS J.* **2005**, 20, 5101-9.

18. Hakulinen N.; Andberg, M.; Kallio, J.; Koivula, A.; Kruus, K.; Rouvinen, J. A near atomic resolution structure of a Melanocarpus albomyces laccase. *J. Struct. Biol.* 1, 29-39.
19. Song, He.; Weitz, A; Hendrich, M.; Lewis, E.; Emerson, J. Building reactive copper centers in human carbonic anhydrase II. *J. Biol. Inorg. Chem.* **2013**, 18, 595-598.
20. Southan, C.; Kruse, Li. Sequence similarity between dopamine beta-hydroxylase and peptide alpha-amidating enzyme: evidence for a conserved catalytic domain. *FEBS Lett.* **1989**, 255, 116-20.
21. Xiaonan, X.; Mains, R.; Eipper, B. Monooxygenase X, a Member of the Copper-Dependent Monooxygenase Family Localized to the Endoplasmic Reticulum. *J. Biol. Chem.* **2004**, 48159-48167.
22. Katarzyna, R.; Chufan, E.; Eipper, B.; Mains, R.; Amzel, M. Peptidylglycine α-Hydroxylating Monooxygenase (PHM). *Handbook of Metalloproteins*, **2011**, 5, 563-568.
23. Cuttitta, F. Peptide amidation: Signature of Bioactivity. *The Anatomical Record*, **1993**, 87-95.
24. Vale, W.; Spiess, J.; Rivier, C.; Rivier, J. Characterization of a 41-resiude ovine hypothalamic peptide that stimulates secretion of corticotropin and beta-endorphin. *Science*, **1981**, 213, 1394-7.
25. Czyzyk, TA.; Ning, Y.; Hsu, MS.; Peng, B.; Mains, RE.; Eipper, B.; Pintar, J. Deletion of peptide amidation enzymatic activity leads to edema and embryonic lethality in the mouse. *Dev. Biol.* **2005**, 287, 301-13.
26. Satani, M.; Takahashi, K.; Sakamoto, H.; Harada, S.; Kaida, Y.; Noguchi, M. Expression and characterization of human bifunctional peptidylglycine α-amidating monooxygenase. *Prot. Expr. And Puri.* **2003**, 28, 293-302.
27. Rudzka, K.; Chufan, E.; Eipper, B.; Mains, R.; Amzel, M. Peptidylglycine α-hydroxylating monooxygenase (PHM). *Handbook of Metalloproteins*. **2011**, 5, 563-568.
28. Chufan, E.; Prigge, S.; Siebert, X.; Eipper, B.; Mains, R.; Amzel, M. Differential Reactivity between Two Copper Sites in Peptidylglycine α-Hydroxylating Monooxygenase. *J. Am. Chem. Soc.*, **2010**, 132, 15565-15572.
29. De la Lande, A.; Marti, S.; Parisel, O.; Moliner, V. Long Distance Electron-Transfer Mechanism in Peptidylglycine α-Hydroxylating Monooxygenase: A Perfect fitting for a Water Bridge. *J. Am. Chem. Soc.* **2007**, 129, 11700-11707.
30. Chen, P.; Solomon, E.; Oxygen Activation by the Noncoupled Binuclear Copper Site in Peptidylglycine α-Hydroxylating Monooxygenase. Reaction Mechanism and Role of the Noncoupled Nature of the Active Site. *J. Am. Chem. Soc.* **2004**, 4991-5000.
31. Prigge, S.; Eipper, B.; Mains, R.; Amzel, L. Dioxygen binds end-on to mononuclear copper in a precatalytic enzyme complex. *Science*, **2004**, 304, 864-867.
32. Evans, J.; Blackburn, N.; Klinman, J. The Catalytic Role of the Copper Ligand H172 of Peptidylglycine α-Hydroxylating Monooxygenase: A Kinetic Study of the H172A Mutant. *Biochemistry*, **2006**, 15419-15429.

33. Pozdnyakova I.; Guidry, J.; Wittung-Stafshede, P.; Studies of Pseudomonas aeruginosa azurin mutants: cavities in beta-barrel do not affect refolding speed. *Biophys. J.* **2002**, 2645-51.
34. Rizzuti, B.; Daggett, V.; Guzzi, R.; Sportelli, L. The early steps in the unfolding of azurin. *Bioch.* **2004**, 49, 15604-9.
35. Berry, S.; Baker, M.; Reardon, N. Reduction potential variations in azurin through secondary coordination sphere phenylalanine incorporations. *J. Inorg. Bioch.* **2010**, 104, 1071-1078.
36. Yu, F.; Penner-Hahn, J.; Pecoraro, L. De Novo-Designed Metallopeptides with Type 2 Copper Centers: Modulation of Reduction Potentials and Nitrite Reductase Activities. *J. Am. Chem. Soc.* **2013**, 135, 18096-18107.
37. Abraham, Z.; Smith, B.; Howes, B.; Lowe, D.; Eady, R. pH dependence for binding a single nitrite ion to each type-2 copper centre in the copper-containing nitrite reductase of Alcaligenes xylosoxidans. *Bioch.* **1997**, 511-6.
38. Adman, E.; Watenpaugh, K.; Jensen, L. NH---S hydrogen bonds in Peptococcus aerogenes ferredoxin, Clostridium pasteurianum rebredoxin, and Chromatin high potential iron protein. *Proc. Natl. Acad. Sci. USA.* **1975**, 4854-8.
39. Strange, R.; Murphy, L.; Dodd, F.; Abraham, Z.; Eady, R.; Smith, B.; Hasnain, S. Structural and kinetic evidence for an ordered mechanism of copper nitrite reductase. *J. Mol. Biol.* **1999**, 287, 1001-9.
40. Sailasuta, N.; Anson, F.; Gray, H. Studies of the thermodynamics of electron transfer reaction of blue copper proteins. *J. Am. Chem. Soc.* **1979**, 101, 455-458.
41. Sykes, A. Active-Site Properties Of The Blue Copper Proteins. *Adv. Inorg. Chem.* **1991**, 377-408.
42. Machonkin, T.; Zhang, H.; Hedman, B.; Hodgson, K.; Solomon, E. Spectroscopic and Magnetic Studies of Human Ceruloplasmin: Identification of a Redox-Inactive Reduced Type 1 Copper Site. *Bioch.* **1998**, 37, 9570-9578.
43. Marshall, N.; Garner, D.; Wilson, T.; Gao, Y.; Robinson, H.; Nilges, M.; Lu, Y. Rationally tuning the reduction potential of a single cupredoxin beyond the natural range. *Nature*, **2009**, 462, 113-116.
44. Yanagisawa, S.; Banfield, M.; Dennison, C. The Role of Hydrogen Bonding at the Active Site of a Cupredoxin: the Phe114Pro Azurin Variant. *Bioch.* **2006**, 45, 8812-8822.
45. Remero, A.; Hoitink, C.; Nar, H.; Huber, R.; Messerschmidt, A.; Canters, G.; X-ray Analysis and Spectroscopic Characterization of M121Q Azurin. *J. Mol. Biol.*, **1993**, 229, 1007-1021.
46. Shis, C.; Museth, A.; Abrahamsson, M.; Blanco-Rodriguez, A.; Di Bilio, A.; Sudhamsu, J.; Crane, B.' Ronayne, K.; Towrie, M.; Vlcek, A.; Richards, J.; Winkler, J.; Gray, H. Tryptophan-accelerated electron flow through proteins. *Science*, **2008**, 320, 1760-2.
47. Allewell, N. M.; Trikha, J. Diffraction Methods in J.A. Glasel & M.P. Deutscher, *Introduction to Biophysical Methods for Protein and Nucleic Acid Research*. **1995**, (pp. 381-390), San Diego, CA.
48. Drenth, J.; Mesters, J. Chapter 1: Crystallizing a Protein. In Principles of Protein X-Ray Crystallography (PP. 1-20). New York, NY: Springer.

49. Krauss, I.; Sica, F.; Mattia, C.; Merlino, A. Increasing the X-ray Diffraction Power of Protein Crystals by Dehydration: The Case of Bovine Serum Albumin and a Survey of the Literature Data. *Int. J. Mol. Sci* **2012**, 13, 3782-3800.
50. Heras, B.; Edeling, M.; Byriel, K.; Jones, A.; Raina, S.; Martin, J. Dehydration Converts DsbG Crystal Diffraction from Low to High Resolution. *Struc. Elsev.* **2003**, 11, 139-145.
51. Faham, S.; Day, M.; Connick, W.; Crane, B.; Di Bilio, A.; Schaefer, W.; Rees, D.; Gray, H. *Acta. Cryst. Sect. D: Biol.* **1999**, *D55*, (2), 379-385.
52. Crane, B.; Di Bilio, A.; Winkler, J.; Gray, H. *J. Am. Chem. Soc.* **2001**, 123 (47), 11623-11631.
53. Gradinaru, C.; Crane, B. *J. Phys. Chem. B.* **2006**, 110, (41), 20073-20076.
54. The PyMOL Molecular Graphics System, Version 1.5.0.4 Schrödinger, LLC

Chapter 2 References

1. Hay, M.; Richards, JH.; Lu, Y. *Proc. Natl. Acad. Sci.* USA **1996,** 93: 461-464.
2. Hay, MT.; Ang, MC.; Gamelin, DR.; Solomon, EI.; Antholine, WE.; Ralle, M.; Blackburn, NJ.; Massey, PD.; Wang, X.; Kwon, AH.; Lu, Y. *Inorg. Chem.* **1998**, 37:191-198.
3. Berry, S.; Mayers, J.; Zehm, N. Models of noncoupled dinuclear copper centers in azurin. *J. Biol. Inorg. Chem.* **2009**, 14:143-149
4. Puiu, M.; Raducan, A.; Babaligea, I.; Oancea D. Oxidase-peroxidase reaction: kinetics of peroxidase-catalyzed oxidation of 2-aminophenol. *Biop. Bios. Eng.* **2008**, 31:579-586.
5. Freeman J.; Nayar P.; Begley T.; Villafranca J. Stoichiometry and Spectroscopic Identity of Copper Centers in Phenoxazinone Synthase: A New Addition to the Blue Copper Oxidase Family. *Bioch,* **1993**, 32, 4826-4830.
6. Krauss, I.; Sica, F.; Mattia, C.; Merlino, A. Increasing the X-ray Diffraction Power of Protein Crystals by Dehydration: The Case of Bovine Serum Albumin and a Survey of the Literature Data. *Int. J. Mol. Sci* **2012**, 13, 3782-3800.
7. Heras, B.; Edeling, M.; Byriel, K.; Jones, A.; Raina, S.; Martin, J. Dehydration Converts DsbG Crystal Diffraction from Low to High Resolution. *Struc. Elsev.* **2003**, 11, 139-145.
8. Deng, X.; Davidson, S.; Thompson, T. Improving the diffraction of apoA-IV crystals through extreme dehydration. *Acta Crys. Sect. F*, **2011**, F68, 105-110.
9. Newman, J. A review of techniques for maximizing diffraction from a protein crystal *in stilla*. *Acta Crys. Sect. D*, **2005**, D62, 27-31.
10. Winn, M.; Ballard, C.; Cowtan, K.; Dodson, E.; Emsley, P.; Evans, P.; Keegan, R.; Krissinel, E.; Leslie, A.; McCoy, A.; Mcnicholas, S.; Murshudov, G.; Pannu, N.; Potterton, E.; Powell, H.; Read, R.; Vagin, A.; Wilson, K. Overview of the CCP4 suite and current developments. *Acta. Crys. Sect. D*, **2010**, D67, 235-242.
11. Emsley, P.; Lohkamp, B.; Scott, W.; Cowtan, K. Features and development of Coot. *Acta. Crys. Sect. D*, **2010**, D66, 486-501.
12. Murshudov, G.; Vagin, A.; Dodson, E. Refinement of Macromolecular Structures by the Maximum-Likelihood method. *Acta. Crys. Sect. D*, **1997**, D53, 240-255.

13. Evans, J.; Blackburn, N.; Klinman, J. The Catalytic Role of the Copper Ligand H172 of Peptidylglycine α-Hydroxylating Monooxygenase: A Kinetic Study of the H172A Mutant. *Biochemistry*, **2006**, 15419-15429.
14. Bauman, A.; Jaron, S.; Yukl, E.; Burchfiel, J.; Blackburn, N. pH Dependence of Peptidylglycine Monooxygenase. Mechanistic Implications of Cu-Methionine Binding Dynamics. *Biochemistry*, **2006**, 45, 11140-11150.
15. Shimoi, H.; Kawahara, T.; Suzuki, K.; Iwasaki, Y.; Jeng, A.; Nishikawa, Y.; Characterization of a *Xenopus laevis* skin peptidylglycine α-hydroxylating monooxygenase expressed in insect-cell culture. *Eur. J. Biochem*, **1992**, 209, 189-194.

Chapter 3 References

1. Bockris, L.; Oldfield, L. The oxidation-reduction reactions of hydrogen peroxide at inert metal electrodes and mercury cathodes. *Trans. Faraday Soc.*, **1955**, 51, 249-259.
2. Das, T.; Dhanasekaran, T.; Alfassi, B.; Neta, P. Reduction Potential of the *tert*-Butylperoxy Radical in Aqueous Solutions. *J. Phys. Chem. A*. **1998**, 102, 280-284.
3. Szigyarto, I.; Simandi, T.; Simandi, L.; Korecz, L.; Nagy, N. A functional phenoxazinone synthase model based on dioximatomanganese(II) Kinetics and mechanism of the catalytic oxidation of 2-aminophenols by dioxygen. *J. Mol. Cat.*, **2006**, 270-276.
4. Miller, J.; Gradinaru, C.; Crane, B.; Di Bilio, A.; Wehbi, W.; Un, S.; Winkler, J.; Gray, H. Spectroscopy and Reactivity of a Photogenerated Tryptophan Radical in a Structurally Defined Protein Environment. *J. Am. Chem. Soc.* **2003**, 125, 14220-14221.
5. Shafaat, H.; Leigh, B.; Tauber, M.; Kim, J. Spectroscopic Comparison of Photogenerated Tryptophan Radicals in Azurin: Effects of local Environment and Structure. *J. Am. Chem. Soc.*, **2010**, 132, 9030-9039.
6. Matthews, B.W. Solvent content of protein crystals. *J. Mol. Biol.* **1968**, 33, 391-497.
7. Nar, H.; Messerschmidt, A.; Huber, Z.; van de Kamp, M.; Canters, G.W.; Crystal structure analysis of oxidized Pseudomonas aeruginosa at pH 5.5 and pH 9.0. A pH-induced conformational transition involves a peptide bond flip. *J. Mol. Biol.* **1991**, 221, 765-772.
8. Murshudov, G.; Skubak, P.; Lebedev, A.; Pannu, N.; Steiner, R.; Nicholls, R.; Winn, M.; Long, F.; Vagin, A. REFMAC5 for the refinement of macromolecular crystal structures. *Acta Cryst. Sec. D.* **2011**, D67, 355-367.
9. Needleman, S.; Wunsh, C. A General Method Applicable to the Search for Similarities in the Amino Acid Sequence of Two Proteins. *J. Mol. Biol.* **1969**, 48, 443-453.
10. Blow, D.; *Outline of Crystallography for Biologists*. New York, NY: Oxford University Press.
11. Bruger, A.T.; Free R Value: a novel statistical quantity for assessing the accuracy of crystal structures. *Nature*, **2004**, 355, 472-475.

12. Kleywegt, G.J.; Validation of protein crystal structures. *Acta Crystallographica,* **2000**, D56, 249-265.
13. Buettner, G.; Jurkiewicz, B.; Chemistry and Biochemistry of Ascorbic Acid. *Handbook of Antioxidants*. New York, NY, **1994**.
14. Bauman, A.; Jaron, S.; Yukl, E.; Burchfiel, J.; Blackburn, N. pH Dependence of Peptidylglycine Monooxygenase. Mechanistic Implications of Cu-Methionine Binding Dynamics. *Bioch.*, **2006**, 45, 11140-11150.
15. Hrycay, E.; Gustafsson, J.; Sundberg, M.; Ernster, L. Hydroxylating agents in steroid hydroxylation reactions catalyzed by partially purified cytochrome p-450. *Biochem. And Biophys. Res. Comm.* **1975**. 66, 209-216.
16. Freeman J.; Nayar P.; Begley T.; Villafranca J. Stoichiometry and Spectroscopic Identity of Copper Centers in Phenoxazinone Synthase: A New Addition to the Blue Copper Oxidase Family. *Bioch,* **1993**, 32, 4826-4830.
17. Alagaratnam, S.; Meeuwenoord, N.; Navarro, J.; Hervas, M.; De la Rosa, M.; Hoffmann, M.; Einsle, O.; Ubbink, M.; Canters, G. Probing the reactivity of different forms of azurin by flavin photoreduction. *FEBS*, **2011**, 278, 1506-1521.
18. Emsley, P.; Lohkamp, B.; Scott, W.; Cowtan, K. Features and development of Coot. *Acta. Crys. Sect. D*, **2010**, D66, 486-501.
19. The PyMOL Molecular Graphics System, Version 1.5.0.4 Schrödinger, LLC